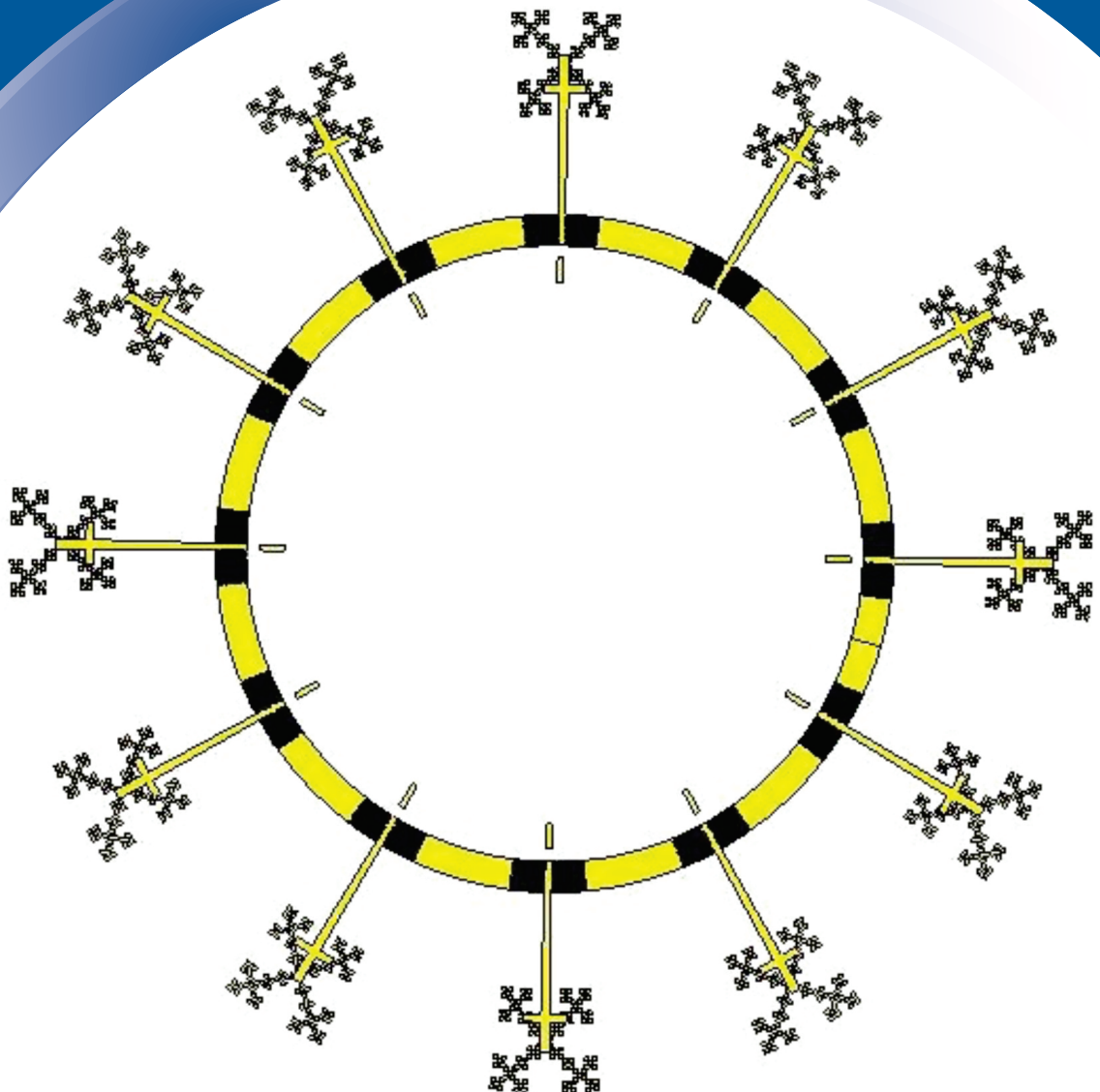


ISSN 0352-9045

Informacije MIDEM

*Journal of Microelectronics,
Electronic Components and Materials*
Vol. 54, No. 2(2024), June 2024

*Revija za mikroelektroniko,
elektronske sestavne dele in materiale*
letnik 54, številka 2(2024), Junij 2024



Informacije MIDEEM 2-2024

Journal of Microelectronics, Electronic Components and Materials

VOLUME 54, NO. 2(190), LJUBLJANA, JUNE 2024 | LETNIK 54, NO. 2(190), LJUBLJANA, JUNIJ 2024

Published quarterly (March, June, September, December) by Society for Microelectronics, Electronic Components and Materials - MIDEEM.
Copyright © 2024. All rights reserved. | Revija izhaja trimesečno (marec, junij, september, december). Izdaja Strokovno društvo za mikroelektroniko, elektronske sestavne dele in materiale – Društvo MIDEEM. Copyright © 2024. Vse pravice pridržane.

Editor in Chief | Glavni in odgovorni urednik

Marko Topič, University of Ljubljana (UL), Faculty of Electrical Engineering, Slovenia

Editor of Electronic Edition | Urednik elektronske izdaje

Kristijan Brecl, UL, Faculty of Electrical Engineering, Slovenia

Associate Editors | Odgovorni področni uredniki

Vanja Ambrožič, UL, Faculty of Electrical Engineering, Slovenia
Arpad Bürmen, UL, Faculty of Electrical Engineering, Slovenia
Danjela Kuščer Hrovatin, Jožef Stefan Institute, Slovenia
Matija Pirc, UL, Faculty of Electrical Engineering, Slovenia
Franc Smole, UL, Faculty of Electrical Engineering, Slovenia
Matjaž Vidmar, UL, Faculty of Electrical Engineering, Slovenia

Editorial Board | Uredniški odbor

Mohamed Akil, ESIEE PARIS, France
Giuseppe Buja, University of Padova, Italy
Gian-Franco Dalla Betta, University of Trento, Italy
Martyn Fice, University College London, United Kingdom
Ciprian Iliescu, Institute of Bioengineering and Nanotechnology, A*STAR, Singapore
Marc Lethiecq, University of Tours, France
Teresa Orłowska-Kowalska, Wrocław University of Technology, Poland
Luca Palmieri, University of Padova, Italy
Goran Stojanović, University of Novi Sad, Serbia

International Advisory Board | Časopisni svet

Janez Trontelj, UL, Faculty of Electrical Engineering, Slovenia - Chairman
Cor Claeys, IMEC, Leuven, Belgium
Denis Donlagić, University of Maribor, Faculty of Elec. Eng. and Computer Science, Slovenia
Zvonko Fazarinc, CIS, Stanford University, Stanford, USA
Leszek J. Golonka, Technical University Wrocław, Wrocław, Poland
Jean-Marie Haussonne, EIC-LUSAC, Octeville, France
Barbara Malič, Jožef Stefan Institute, Slovenia
Miran Mozetič, Jožef Stefan Institute, Slovenia
Stane Pejovnik, UL, Faculty of Chemistry and Chemical Technology, Slovenia
Giorgio Pignatelli, University of Perugia, Italy
Giovanni Soncini, University of Trento, Trento, Italy
Iztok Šorli, MIKROIKS d.o.o., Ljubljana, Slovenia
Hong Wang, Xi'an Jiaotong University, China

Headquarters | Naslov uredništva

Uredništvo Informacije MIDEEM
MIDEEM pri MIKROIKS
Stegne 11, 1521 Ljubljana, Slovenia
T. +386 (0)1 513 37 68
F. + 386 (0)1 513 37 71
E. info@midem-drustvo.si
www.midem-drustvo.si

Annual subscription rate is 160 EUR, separate issue is 40 EUR. MIDEEM members and Society sponsors receive current issues for free. Scientific Council for Technical Sciences of Slovenian Research Agency has recognized Informacije MIDEEM as scientific Journal for microelectronics, electronic components and materials. Publishing of the Journal is cofinanced by Slovenian Research Agency and by Society sponsors. Scientific and professional papers published in the journal are indexed and abstracted in COBISS and INSPEC databases. The Journal is indexed by ISI® for Sci Search®, Research Alert® and Material Science Citation Index™. |

Letna naročnina je 160 EUR, cena posamezne številke pa 40 EUR. Člani in sponzorji MIDEEM prejema posamezne številke brezplačno. Znanstveni svet za tehnične vede je podal pozitivno mnenje o reviji kot znanstveno-strokovni reviji za mikroelektroniko, elektronske sestavne dele in materiale. Izdajo revije sofinancirajo ARRS in sponzorji društva. Znanstveno-strokovne prispevke objavljene v Informacijah MIDEEM zajemamo v podatkovne baze COBISS in INSPEC. Prispevke iz revije zajema ISI® v naslednje svoje produkte: Sci Search®, Research Alert® in Materials Science Citation Index™.

Content | Vsebina

Original scientific papers

Izvirni znanstveni članki

M. M. Ismail, B. B. Q. Elias, T. A. Elwi, B. S. Bashar, A. I. Alanssari, Z. A. Rhazal, H. Misran: Multi-Beam Metasurface Control Based on Frequency Reconfigurable Antenna	77	M. M. Ismail, B. B. Q. Elias, T. A. Elwi, B. S. Bashar, A. I. Alanssari, Z. A. Rhazal, H. Misran: Večžarčni metapovršinski nadzor na podlagi frekvenčno nastavljive anten
H. Wu, S. Jiang, S. Seyedi, N. J. Navimipour: Quantum-based serial-parallel multiplier circuit using an efficient nano-scale serial adder	87	H. Wu, S. Jiang, S. Seyedi, N. J. Navimipour: Kvantno vezje zaporedno-paralelnega množilnika z uporabo učinkovitega zaporednega seštevalnika v nano merilu
V. R. Nedungadi, V. Ranganathan: A Multiband Meanderline Rectenna: Design and Simulation for Enhanced Performance	95	V. R. Nedungadi, V. Ranganathan: Večpasovna Meanderline rektena: načrtovanje in simulacija za večjo zmogljivost
J. R. Selvaraj, A. Ramasamy: Optimization of Mobile Ad-hoc Networks Communication Using Ad-hoc On-demand Multipath Distance Vector With Novel Aging Multi Population Strategy for Effectual Energy Utilization	107	J. R. Selvaraj, A. Ramasamy: Optimizacija komunikacije v mobilnih omrežjih Ad-hoc z uporabo vektorja razdalje na zahtevo z novo strategijo staranja večje populacije za učinkovito rabo energije
P. Ramesh, B. Mohan, L. Viswanath, B. J. Stephen: Software Defined Network Architecture Based Network Slicing in Fifth Generation Networks	123	P. Ramesh, B. Mohan, L. Viswanath, B. J. Stephen: Programsko definirana omrežna arhitektura, ki temelji na rezinjenju omrežja v omrežjih pete generacije
H. Pamu, P. K. Kumar, K. K. Gurralla: A Novel Dual-Mode Dual Type Hysteresis Schmitt Trigger and its Applications using Single Differential Voltage Current Conveyor Transconductance Amplifier	131	H. Pamu, P. K. Kumar, K. K. Gurralla: Nov dvonivojski histerezni Schmittov prožilec in njegova uporaba z uporabo enojnega diferencialnega napetostnega tokovnega transkonduktančnega ojačevalnika
M. Pirc: Empirical Light-soaking and Relaxation Model of Perovskite Solar Cells in an Indoor Environment	149	M. Pirc: Empirični model svetlobnega prežemanja in relaksacije perovskitnih sončnih celic v notranjem okolju
Announcement and Call for Papers: 59 th International Conference on Microelectronics, Devices and Materials With the Workshop on Electromagnetic Compatibility: From Theory To Practice	163	Napoved in vabilo k udeležbi: 59. mednarodna konferenca o mikroelektroniki, napravah in materialih z delavnico o elektromagnetski kompatibilnosti: Od teorije do prakse
Front page: The CRLH structure. (M. M. Ismail et al.)		Naslovnica: CRLH struktura (M. M. Ismail et al.)

Multi-Beam Metasurface Control Based on Frequency Reconfigurable Antenna

Marwa M. Ismail¹, Bashar Bahaa Qas Elias², Taha A. Elwi^{3,4}, Bashar S. Bashar⁵, Ali Ihsan Alanssari⁶, Z.A. Rhazal⁷, Halina Misran⁸

^{1,2}Department of Information and Communication Engineering, College of Information Engineering, Al-Nahrain University, Jadriya, Baghdad, Iraq

³International Applied and Theoretical Research Center (IATRC), Baghdad Quarter, Iraq;

⁴Islamic University Centre for Scientific Research, The Islamic University, Najaf, Iraq

^{5,7}Electrical & Electronic Engineering Department College of Engineering Universiti Tenaga Nasional Kajang, Malaysia

⁶Department of Systems Engineering, College of Information Engineering, Al-Nahrain University, Jadriya, Baghdad, Iraq

⁸Nanoarchitectonic Laboratory Department of Mechanical Engineering Universiti Tenaga Nasional Kajang, Malaysia

Abstract: This paper presents a new design and analysis of a reconfigurable antenna with a switchable slot held using PIN diodes for multifunction reconfiguration, including frequency multiplexing. The performance of the proposed antenna in terms of reflection coefficient spectra and radiation patterns is evaluated. From the results obtained, it is observed that the antenna can be operated for different frequencies: 1.8 GHz, 2.7 GHz, 3.1 GHz, 3.3 GHz, 4.1 GHz, 5.1 GHz, and 5.4 GHz. A maximum gain of 11.1 dBi is also significantly achieved at 5.1 GHz. Moreover, this antenna is designed to provide a high Q-factor and low-frequency ratio (FR) for using the spectrum efficiently. Upon the advantage of spatial diversity, multiple independent data streams can be transmitted over the same frequency simultaneously. All results obtained in this work were produced based on the simulation process using CST Microwave Studio simulator software at different switching scenarios.

Keywords: Reflection coefficient, gain, microstrip patch, modes, Metasurface

Večzarčni metapovršinski nadzor na podlagi frekvenčno nastavljive antene

Izveček: Prispevek predstavlja novo zasnovo in analizo nastavljive antene s preklopno režo z uporabo diod PIN za več funkcijsko nastavljivost, vključno s frekvenčnim multipleksiranjem. O vrednoteni je zmogljivost predlagane antene v smislu spektrov koeficienta odboja in sevalnih vzorcev. Iz dobljenih rezultatov je razvidno, da lahko antena deluje na različnih frekvencah: 1,8 GHz, 2,7 GHz, 3,1 GHz, 3,3 GHz, 4,1 GHz, 5,1 GHz in 5,4 GHz. Pri frekvenci 5,1 GHz je doseženo tudi največje ojačenje 11,1 dBi. Poleg tega je ta antena zasnovana tako, da zagotavlja visok faktor Q in nizko frekvenčno razmerje (FR) za učinkovito uporabo spektra. S prednostjo prostorske raznolikosti je mogoče hkrati prenašati več neodvisnih podatkovnih tokov na isti prosti frekvenci. Vsi rezultati, pridobljeni v tem delu, so bili pridobljeni na podlagi postopka simulacije z uporabo programske opreme CST Microwave Studio pri različnih scenarijih preklapljanja.

Ključne besede: Odbojni koeficient, ojačanje, mikrotrakasta krpica, meta površina

*Corresponding Author's e-mail: bashar.bahaa@nahrainuniv.edu.iq, PE21173@student.uniten.edu.my

How to cite:

M. M. Ismail et al., "Multi-Beam Metasurface Control Based on Frequency Reconfigurable Antenna", Inf. Midem-J. Microelectron. Electron. Compon. Mater., Vol. 54, No. 2(2024), pp. 77–85

1 Introduction

After years of building high-efficiency transceivers to compensate for signal loss at the ends of a radio channel, designers are now beginning to realize that they have reached the practical limits of transceiver efficiency as they prepare to introduce the 5th generation (5G) technology [1-3]. 5G communication systems must meet a wide range of needs, such as extremely high data rates, high mobility, and low latency unavailable in preexisting networks [4]. 5G technology has some outstanding qualities, which are boosting its adoption. One of the most notable advantages of 5G is its high data speeds, which surpass 20 Gbps - substantially faster than 4G LTE's 1 Gbps peak. Furthermore, 5G has tremendous mobility, allowing users to maintain lightning-fast speeds even when on the move. Moreover, another major feature of 5G is its incredibly low latency, which is expected to be as low as 1 millisecond, significantly lower than the 50-millisecond delay of 4G. This near-instant reaction time allows for real-time applications such as self-driving cars, which require quick communication. The combination of high data speeds and low latency makes 5G a major change in modern connection. Overall, 5G has greater performance in areas like data rates. Tele-education, virtual reality offices, social media, telemedicine, e-governance, e-commerce, and many other emerging high-data-rate applications will necessitate these standards [5]. A high-gain antenna array is highly desired for such a wide range of applications[6]. Multiple-input multiple-output (MIMO) antennas are utilized to meet the vast need for high-volume data transmission across the communication channel because of their exceptional characteristics, including immunity to multipath fading, low consumption of power compared to data rate, and fast data utilization [7, 8].

Resource allocation in 5G networks can be a complex optimization problem requiring efficient algorithms [9]. One of the most popular approaches is distributed optimization, which involves multiple nodes in the network collaborating to solve the optimization problem [10]. One such algorithm is the Alternating Direction Method of Multipliers (ADMM) [11]. ADMM is a distributed optimization algorithm well-suited for resource allocation problems in communication networks. It is advantageous when the optimization problem can be decomposed into smaller sub-problems [12].

In the context of resource allocation in 5G networks, ADMM can allocate radio resources such as bandwidth and power to different users in the network [13]. The problem can be formulated as a constrained optimization problem, where the objective is to maximize the network throughput subject to constraints on the available re-

sources [14]. The ADMM algorithm involves the following steps: Decompose the problem into smaller sub-problems, each of which can be solved by individual nodes in the network [15]. Each node solves its sub-problem independently and then communicates the solution to its neighbors [2]. The neighboring nodes exchange information and update their solutions accordingly [16, 17]. The process is repeated until convergence [18].

Contemporary portable wireless communication devices need multi-functional antennas adaptable to changing system requirements. The Reconfigurable antennas have received substantial consideration in recent years due to their capability to change electromagnetic wave frequency, polarization, or radiation pattern[19, 20]. In an advanced wireless communication system, multiple antennas are deployed for various application-specific tasks[21]. As a result, the system becomes complex and bulkier. The advanced portable device requires a single radiating structure to operate at multiple frequencies. This led to the development of multiband antennas. These antennas offer only fixed performance and cannot be tuned to the user's request. In such scenarios, the concept of frequency reconfiguration provides an excellent solution. This allows the radiating structure to switch at a frequency based on the antennas, which are significant in 5G and cognitive radio communications technologies[22].

Reconfigurable antennas can be reconfigured regarding operating frequency, polarization, or radiation pattern [7]. Due to the 5G technology demand in beam steering and beam shaping, radiation pattern reconfigurable antennas are vital and are being researched extensively. In 5G technology, the mid-band frequencies are defined from 1 to 6 GHz ,being widely used in many wireless technologies, particularly the Internet of Things applications[23]. Using the mid-band frequencies, low power consumption can be maintained when communicating within a short range of network devices [24]. However, the effectiveness of such systems depends on the level of multipath and interference [25]. Thus, reconfiguration of the radiation patterns of antennas will enable the enhancement of signal strength and transmission efficiency [6]. Pattern reconfiguration antennas are one of the critical technologies for modern telecommunication applications. Pattern reconfigurability is essential with the ability to change the current source distribution on the antenna structure by performing the radiated energy as the beam to the dedicated or specific directions that eventually helps improve the communication's data throughput [26, 27]. The reconfigurable pattern antenna could avoid noise sources by directing null toward interference and radiating the main beam to the desired direction for better coverage improvement. This antenna

has advantages with its compact size, small power consumption, and increasing functionality to resolve the burden on today’s transmission systems within a confined space[28]. This paper presents a simple, compact, low-cost, parasitic, composite right/left-handed (CRLH) resonator-based reconfigurable antenna exhibiting frequency and pattern diversity. The proposed antenna is suitable for steering omnidirectional radiation patterns into bi-directional and unidirectional end-fire radiation patterns for multiple frequencies.

2 Antenna configuration

In this work, a reconfigurable antenna is structured based on a truncated patch with slots to realize a primary patch antenna to couple the electromagnetic energy inductively to a second patch antenna based on a fractal geometry of a novel structure. As seen in Figure 1, four PIN diodes are proposed to the primary antenna patch to adapt and adjust (reconfigure) an individual radiator’s fundamental operating features to their environment by altering their operating frequencies, impedance, radiation pattern, and polarization separately. The second patch of the antenna is introduced to increase the antenna bandwidth through the effects of the inductive coupling. However, raising the proposed Meta surface (MTS) increases the antenna gain at the desired frequencies.

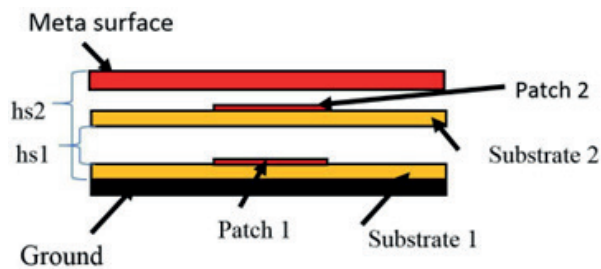


Figure 1: layout of the antenna structure.

The first antenna layer is a microstrip patch with four slots, as seen in Figure 2. These slots are proposed to reduce the effects of surface wave fringing and mitigate the phase retardations from the patch edges. The second layer is designed as a ring of interdigitated capacitors connected to eight fractal patches by T-shaped stubs. The fractal patch also has the advantage of controlling the input impedance matching at the desired resonant frequency through capacitive coupling by directing current to each unit cell. In addition, the proposed MTS is invoked to direct antenna radiation in a specific direction with minimal reflections by gently transferring electromagnetic energy into its free space. This combination realizes the advantages of increasing the antenna bandwidth and gain. In this way, antenna

gain is maximized while maintaining the original radiation pattern characteristics of the base station antenna but increasing radiation efficiency and gain. The antenna is printed on a Taconic RF-30 (lossy) substrate with $280 \times 280 \text{ mm}^2$ of $\epsilon_r=4.4$ and 1.6 mm thickness. The entire antenna system height is fixed to 70 mm for maximum gain. The rest of the proposed antenna dimensions are listed in Table 1.

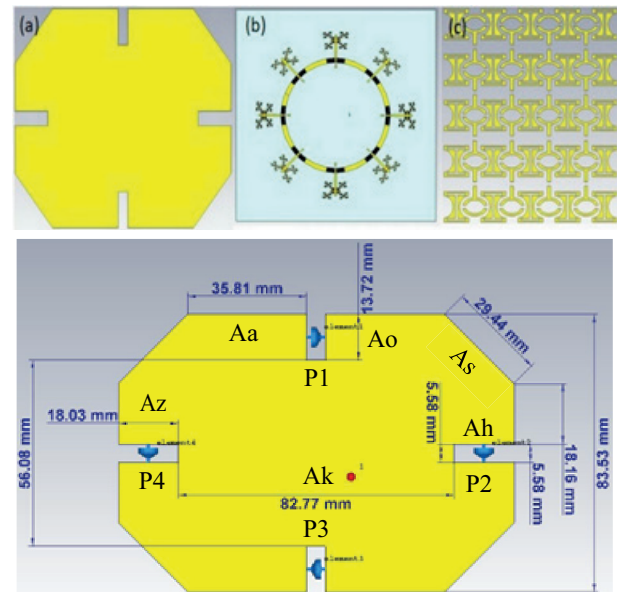


Figure 2: The proposed antenna structure with geometrical details.

Table 1: Overall dimensions of the proposed antenna.

Parameter	Value (mm)	Parameter	Value (mm)
Aa	35.81	Ac	5.58
Az	18.03	As	29.44
Ab	55.08	Ax	83.53
Ao	13.72	Ak	82.77

3 Description of antenna layers

The antenna design process and critical parameters leading to the results are elucidated in this section. The outcomes were assessed utilizing CST software employing the Finite Integration Technique (FIT) tailored for microwave devices. A time-domain solver was used in the analysis for wideband or multiband antennas. All dimensions are expressed in millimeters, with the frequency range extending from 0 GHz to 6 GHz, and a parasitic layer is utilized in the suggested design. The study shows that the proposed design enhances gain bandwidth by mitigating conduction and ground plane capacitance losses and suppressing surface waves by

incorporating electromagnetic band gap (EBG) defects. The simulation and analysis processes are segmented into the following parts.

3.1 Patch antenna (first layer)

This section presented a parametric study to realize the effects of the proposed shape of the patch on the antenna performance. At this step of design illustrated in Figure 3(a), multiple bands of a traditional rectangular patch are obtained, 9 bands from 3 GHz to 5.7 GHz. Meanwhile, a maximum gain of 11.5 dBi at 4.8 GHz is observed. Then, it is medicated by cutting the edge of the rectangle, as depicted in Figure 3 (b). Next, in Figure 3(c), the patch structure includes cutting 4 slots from the corners of the radiators with different dimensions. Figure 4(a and b) displays the results of the reflection coefficient and gain obtained. It is observed that multiple bands are achieved from 2.6 GHz to 5.9 GHz with 15 bands, and the maximum gain is 11.0 dBi at 4.9 and 5.1

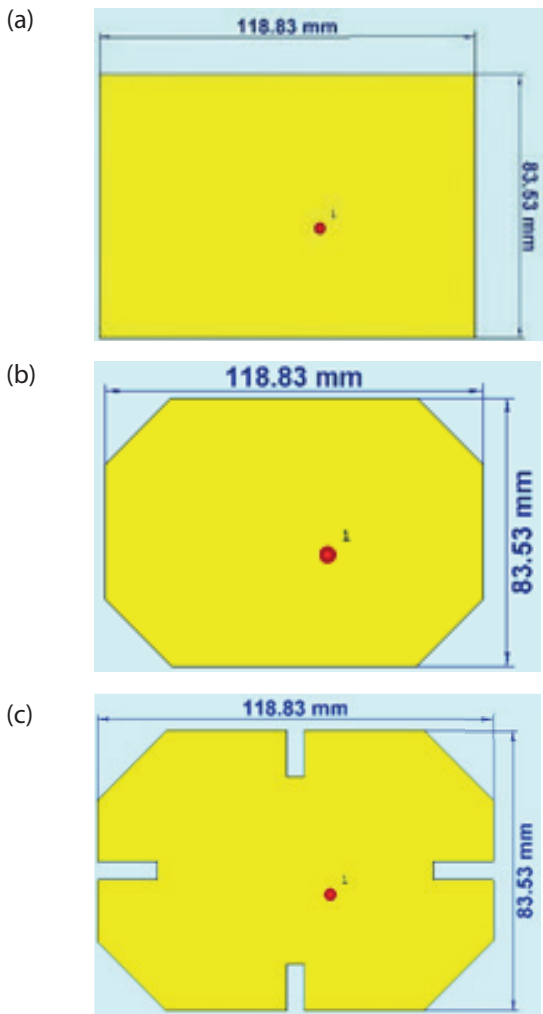


Figure 3: The modeling of patch antenna a) the rectangle patch b) the cutting edge of rectangle c) the antenna proposal.

GHz, the results in current distribution enhancements that improve the antenna. All modeling has the exact dimensions.

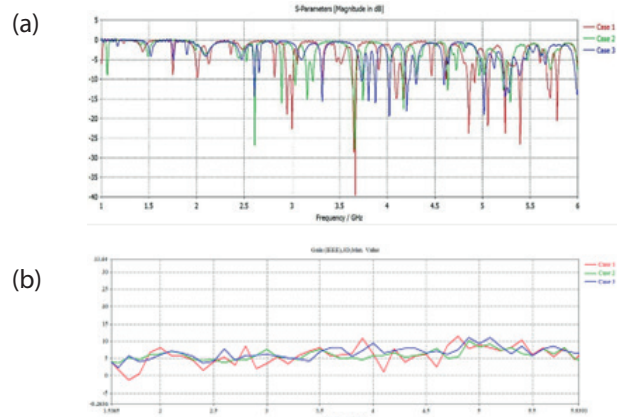


Figure 4: The parametric study of patch antenna (First Layer) a) reflection coefficient of antenna b) the gain of patch antenna.

3.2 The CRLH (second layer)

This section introduces the effects of the second layer of the proposed antenna on the antenna performance by increasing the number of facts (see Figure 5 (a and b)). The reflection coefficient and gain spectra are calculated and presented in Figure 6(a and b). Based on the

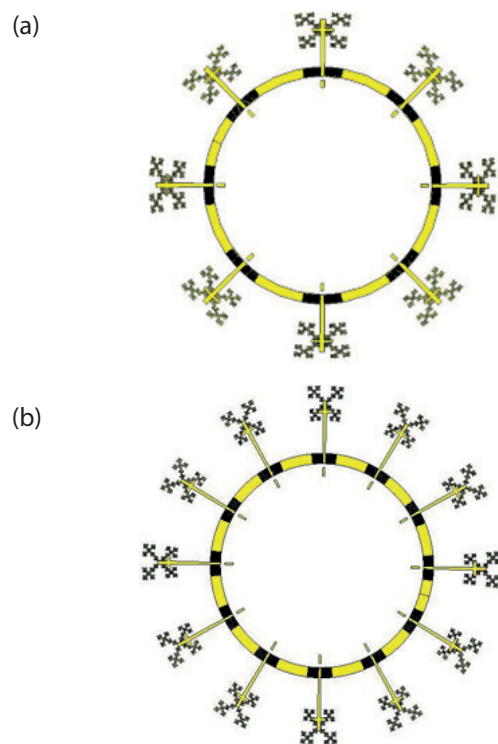


Figure 5: The CRLH structure (second layer) a) the 8 Fractal b) 12 Fractal.

recorded results of mode 1, the reflection coefficient is reduced, and it sometimes shows a gain enhancement, as shown in Figure 5 (a). Next, in mode 2, further improvement in the reflection coefficient and gains are significantly observed. On the other hand, the radiation pattern in mode 2 does not originate at 1.9 GHz, whereas in mode 1, the radiation pattern is exhibited. On the other hand, the reflection coefficient of mode 1 has 12 multiband frequencies from 2.7 GHz to 5.5 GHz and 9 multiband frequencies in mode 2 from 2.6 GHz to 5.6 GHz. Furthermore, gain results in mode 2 are more improved than mode 3, where at the frequency of 3.1 GHz, the gain value attained to 6.37 dBi, and 3.1 GHz in mode 2, the gain is 8.14 dBi.

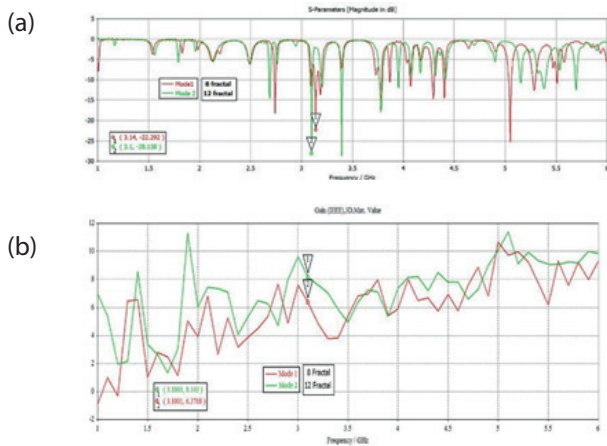


Figure 6: The CRLH structure (second layer) a) reflection coefficient results in b) gain result.

3.3 The MTS structures

This section considers the effect of the proposed MTS on the antenna performance with variation in the distance between the antenna from MTS and the second layer near and far between them (see Figure 7), which is also listed in Table 2. Mode 1 shows a minimized reflection coefficient than the rest modes and provides efficient gain at 4.4 GHz as well. Also, the gain in mode 2 is equal to 14.8 dB, where the MTS near the second layer is found as 25.33 mm with a similar value of the reflection coefficient in the case of mode 1. In addition, the gain decreases at mode 2 as compared with other modes, where the maximum gain at 3 GHz is 11.8 dBi. In mode 3, the MTS are far from the second layer with 60.25 mm. The reflection coefficient also still has the same value as mode 1. In the meantime, the gain value that is produced at this mode shows less than that at mode 1 and better than the gain at mode 2. The overall results are demonstrated in Figure 8.

Table 2: The distance between MTS and the second layer in all cases

Case	Value (mm)
Mode 1	40.28
Mode 2	25.23
Mode 3	60.25

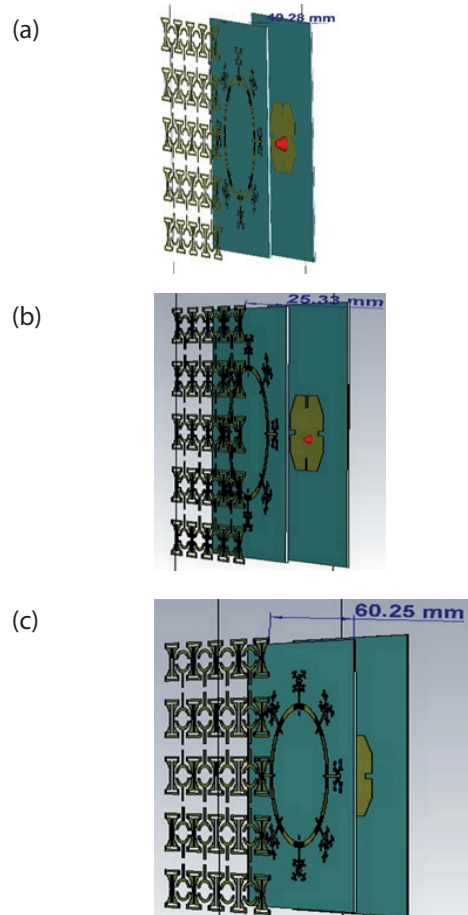


Figure 7: Distances of the MTS structure a) case 1 b) case 2 c) case 3

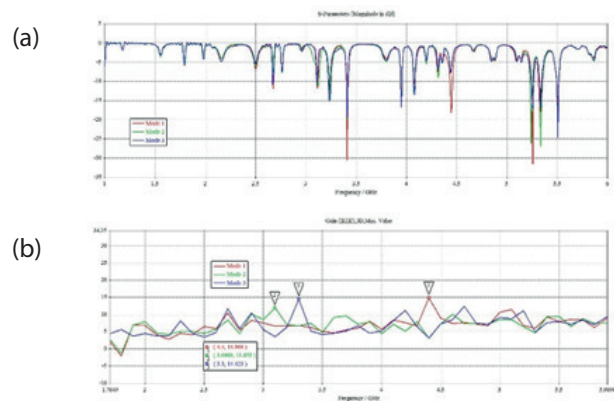


Figure 8: The result of MTS a) the Reflection coefficient of antenna b) the gain

Moreover, the radiation pattern at 4.4, 3.1, and 3.3 GHz are clearly illustrated in Figure 9.

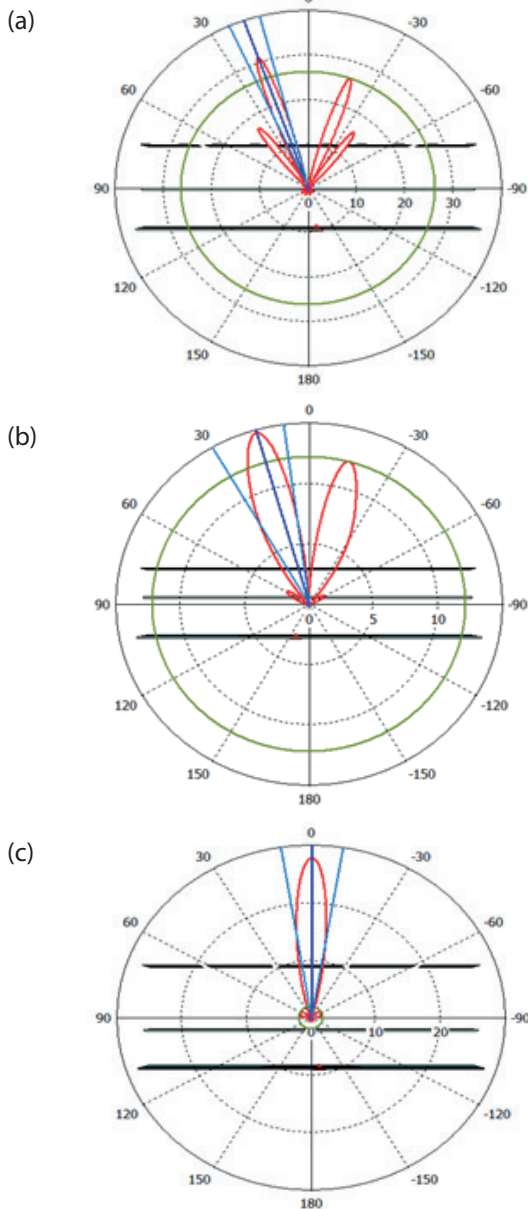


Figure 9: The radiation pattern of antenna at a) 4.4 GHz b) 3.1GHz c) 3.3 GHz

The methodology of the antenna design and the obtaining results are depicted in Figure 10.

The proposed antenna performance based on the first layer is compared to the one based on the second layer of the fractal geometry and MTS layer, as seen in Figure. 11. The antenna performance in terms of the reflection coefficient spectrum is shown for each layer. A significant variation in the reflection coefficient spectra is found due to the individual introduction of each layer. The proposed antenna offers several frequency resonance modes with excellent matching of reflection co-

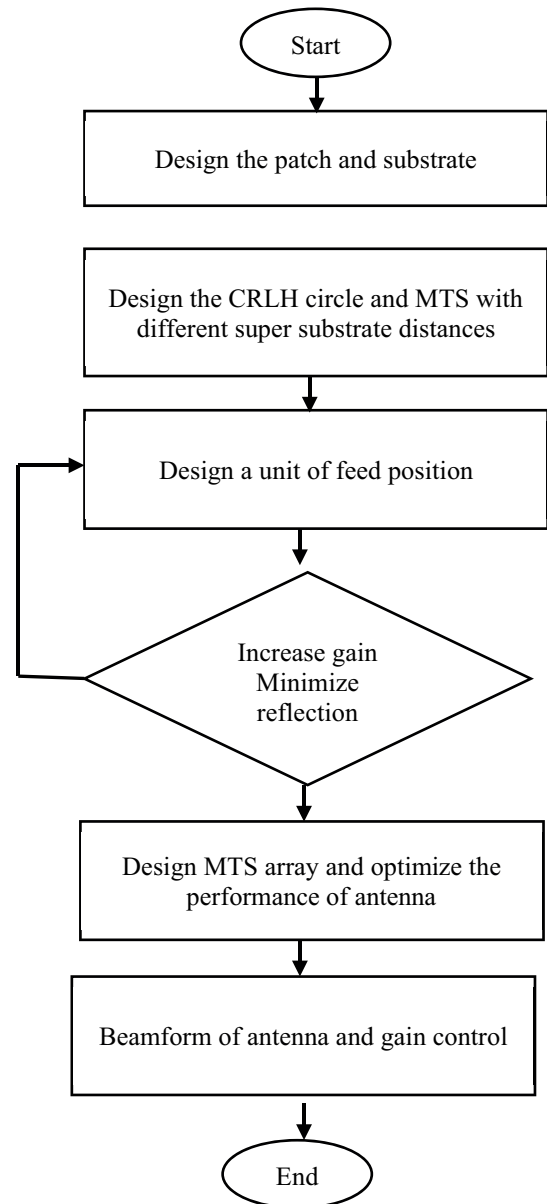


Figure 10: Flowchart of the antenna design

efficient magnitude below -10dB. Such achievements are attributed to the introduction of fractal geometry. The proposed structure is designed and analyzed using CST microwave studio. To excite the radiating structure, a 50Ω discrete port is assigned. The performance parameters, i.e., return loss, gain, and surface current plots, are obtained using the standard boundary conditions in the CST microwave studio and powered by the circular patch. Therefore, a series of simulations were performed, as shown in Table 3—the PIN diode resistance and capacitance in the ON and OFF conditions. By controlling the biasing of the PIN diodes, the distribution of the antenna surface current will be modified; this will deflect the direction of the antenna radiation.

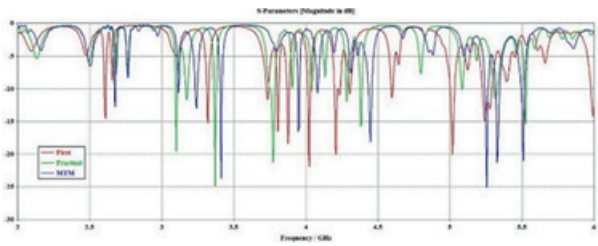


Figure 11: Reflection coefficient results

In the simulation environment, a parallel lumped RLC model with R, L, and C values shown in Figure 12 (a & b) mimics diodes ON and OFF states. It can be seen from Figure 12 (a) that in the ON state, an equivalent circuit having a series combination of 3Ω resistor and 2.6e-10 H inductor is modeled using parallel RLC boundary conditions. On the other hand, in the OFF state, a series combination of 0 H with a similar combination of 20 kΩ resistor and 0.04 pF capacitor, as depicted in Figure 12 (b), is modeled using RLC boundary conditions. The ON and OFF states of PIN diodes change the electrical length of the radiator to allow the appropriate low current density. Consequently, the ON and OFF states of pin diodes matched the impedance at different frequency bands at a time. They resulted in frequency reconfigurability at multiband depending upon the RF current.

The proposed antenna achieved reconfigurability by changing the diodes' switching process to offer an open and short circuit behavior between radiating patches. The antenna has five operating modes, each with a unique resonant frequency scheme. The conditions of the PIN diodes at each mode and respective deep bands are detailed in Table 3. Compared to other types of diodes, Varactor diodes are preferred to use in this work for the capability of producing voltage-controlled variable capacitance in radio frequency or RF circuits. These diodes also produce very little noise and are offered at a reduced cost.

Table 3: The statuses of the antenna reconfiguration.

Case no.	Status of Pin diodes				Frequency/GHz	Gain/dBi
	P1	P2	P3	P4		
1	OFF	OFF	ON	ON	1.7,2.6,4	1.82,6.51,5.82
2	OFF	ON	OFF	ON	2.7,2.8,3.3	2.23,2.8,5.99
3	ON	ON	OFF	OFF	2.7,3.1,4.1	2.18,4.69,7.45
4	ON	OFF	ON	OFF	3.1	4.9
5	OFF	OFF	OFF	OFF	3.1,3.3,4.1,5.1,5.4	5.05,6.08,7.67,9.87,9.62
6	OFF	OFF	ON	OFF	4	7.68
7	ON	ON	ON	ON	2.7,2.8,3.1,4.1	2.48,2.81,
8	OFF	OFF	OFF	ON	1.8,2.7,3.1,3.3,4.1,5.1,5.4	0.19,2.23,5.27,5.95,7.2,11.1,8.81
9	ON	ON	ON	OFF	2.8,3.1	2.81,5.32
10	ON	OFF	ON	ON	1.8,2.7,3.1	0.1,24,4.97

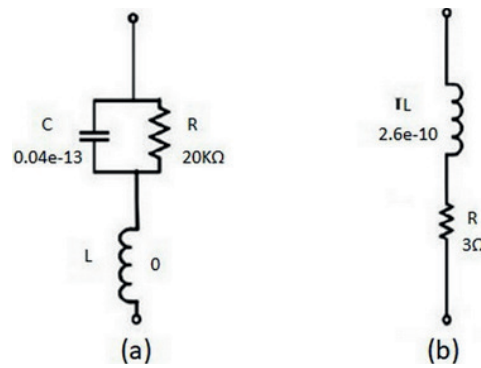


Figure 12: The RLC model operation of antenna: (a) OFF and (b) ON

The presented results in Table 2 illustrate that the proposed antenna has different operating modes. In Figure 13, the three studied cases show a maximum outcome variation. The obtained reflection coefficient indicates that the proposed antenna offers a wideband reconfigurability. For this, the antenna's best performance is achieved when all diodes are switched OFF.

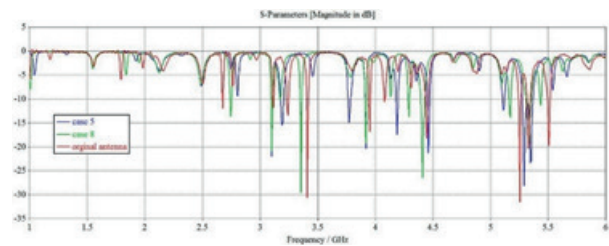


Figure 13: Results of reflection coefficient for the three cases.

On the other hand, the antenna far-field radiation patterns are evaluated using an electromagnetic simulator from case 8. Figure 14 demonstrates the simulated radiation patterns generated by using the CST software. The main antenna beam is observed to be steered according to the switching conditions.

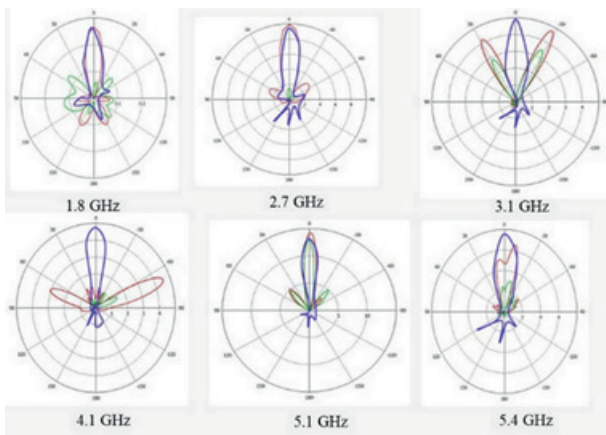


Figure 14: The antenna radiation pattern at different frequency bands.

To compare the proposed performance with other studies and with previously published research in the literature, Table 4 shows that the proposed antenna has a pattern-reconfigurability and enhanced gain and realizes a significant size reduction with less design complexity.

4 Conclusion

This work proposes a reconfigurable antenna controlled using four PIN diodes for modern applications, including direct frequency multiplexing applications. This antenna is designed to operate for different frequency bands with acceptable gain. The antenna performance is very effective in the PIN diode switching change. The characteristics of each case are studied and discussed based on the simulation results obtained. The proposed antenna can be operated with the following frequencies: 1.8 GHz, 2.7 GHz, 3.1 GHz, 3.3 GHz, 4.1 GHz, 5.1 GHz, and 5.4 GHz. Additionally, the antenna achieved an agreement gain of up to 11.1 dBi at 5.1 GHz and 8.81 dBi at 5.2 GHz. Compared with

other related published papers, this antenna exhibits less complexity and is highly efficient for different applications.

5 Conflict of Interest

The authors declare no conflict of interest.

6 References

1. J. Zhu, C.-H. Chu, L. Deng, C. Zhang, Y. Yang, and S. Li, "mm-Wave high gain cavity-backed aperture-coupled patch antenna array," *IEEE Access*, vol. 6, pp. 44050-44058, 2018.
2. J. Khan, S. Ullah, U. Ali, F. A. Tahir, I. Peter, and L. Matekovits, "Design of a millimeter-wave MIMO antenna array for 5G communication terminals," *Sensors*, vol. 22, no. 7, p. 2768, 2022.
3. B. S. Bashar, Z. Rhazali, H. Misran, M. M. Ismail, and M. T. Al-Sharify, "Gain enhancement for patch antenna loading with slotted parasite antenna based on metasurface super substrate," in *AIP Conference Proceedings*, 2023, vol. 2787, no. 1: AIP Publishing.
4. K. Raheel *et al.*, "E-shaped H-slotted dual band mmWave antenna for 5G technology," *Electronics*, vol. 10, no. 9, p. 1019, 2021.
5. H. Ullah and F. A. Tahir, "A broadband wire hexagon antenna array for future 5G communications in 28 GHz band," *Microwave and Optical Technology Letters*, vol. 61, no. 3, pp. 696-701, 2019.
6. Q. Zhu, K. B. Ng, C. H. Chan, and K.-M. Luk, "Substrate-integrated-waveguide-fed array antenna covering 57–71 GHz band for 5G applications," *IEEE Transactions on Antennas and Propagation*, vol. 65, no. 12, pp. 6298-6306, 2017.
7. C.-X. Mao, S. Gao, and Y. Wang, "Broadband high-gain beam-scanning antenna array for millimeter-

Table 4: Comparison between recently proposed antennas and the proposed.

Ref.	Frequency/ GHz	Reconfiguration	Technique	Gain/ dBi	PIN
[7]	3.1, 4.1, 3.8, 2.45, 7.8, 9.5	Frequency/ pattern	Hexagon/CPW	1.56, 4.24, 1.67, 1.68, 3.49, 1.69	2
[24]	2.4, 5.8	Frequency	slots	4	2
[1]	2.4, 5.8	Pattern	EBG	6.2, 6.6	14
[2]	2.6, 3.5, 4.2, 4.5, 5, 5.5	Frequency/ pattern	Parasitic/patch	1.72, 1.94, 2.51, 2.81, 3.66, 3.8	8
[4]	4.66, 5.2, 5.3, 5.8	Frequency	V-Shaped	3.4, 6	2
[5]	5.77-7.10	Frequency	Quasi-Yagi	5.7	4
[6]	5.8	Frequency/ pattern	Patch	5.95	4
[20]	2.6/4.2/5.6	Frequency	MS / supersubstrate	8.2/4.49/6.24	3
[3]	2.3	Gain	Metamaterial	6.15	3
This work	1.8, 2.7, 3.1, 3.3, 4.1, 5.1, 5.4	Frequency/ pattern	diodes	0.19, 2.23, 5.27, 5.95, 7.2, 11.1, 8.81	4

- wave applications," *IEEE Transactions on Antennas and Propagation*, vol. 65, no. 9, pp. 4864-4868, 2017.
8. B. Batagelj, "Centimeter positioning accuracy in modern wireless cellular networks—wish or reality?," *Informacije MIDEM*, vol. 53, no. 4, pp. 239-248, 2023.
 9. H. Ullah and F. A. Tahir, "A novel snowflake fractal antenna for dual-beam applications in 28 GHz band," *IEEE Access*, vol. 8, pp. 19873-19879, 2020.
 10. E. G. Larsson, O. Edfors, F. Tufvesson, and T. L. Marzetta, "Massive MIMO for next generation wireless systems," *IEEE communications magazine*, vol. 52, no. 2, pp. 186-195, 2014.
 11. S. Shamim, U. S. Dina, N. Arafin, and S. Sultana, "Design of efficient 37 GHz millimeter wave microstrip patch antenna for 5G mobile application," *Plasmonics*, vol. 16, no. 4, pp. 1417-1425, 2021.
 12. R. Rashmitha, N. Niran, A. A. Jugale, and M. R. Ahmed, "Microstrip patch antenna design for fixed mobile and satellite 5G communications," *Procedia Computer Science*, vol. 171, pp. 2073-2079, 2020.
 13. N. Ojaroudiparchin, M. Shen, and G. F. Pedersen, "Beam-steerable microstrip-fed bow-tie antenna array for fifth generation cellular communications," in *2016 10th European Conference on Antennas and Propagation (EuCAP)*, 2016: IEEE, pp. 1-5.
 14. M. El Shorbagy, R. M. Shubair, M. I. AlHajri, and N. K. Mallat, "On the design of millimetre-wave antennas for 5G," in *2016 16th Mediterranean Microwave Symposium (MMS)*, 2016: IEEE, pp. 1-4.
 15. I. Elfergani, A. S. Hussaini, A. M. Abdalla, J. Rodriguez, and R. Abd-Alhameed, "Millimeter wave antenna design for 5G applications," *Optical and Wireless Convergence for 5G Networks*, pp. 139-156, 2019.
 16. M. Ur-Rehman, Q. H. Abbasi, A. Rahman, I. Khan, H. T. Chattha, and M. A. Matin, "Millimetre-wave antennas and systems for the future 5G," vol. 2017, ed: Hindawi, 2017.
 17. A. R. Al-tameemi et al., "A Novel Conformal MIMO Antenna Array based a Cylindrical Configuration for 5G Applications," in *2022 9th International Conference on Electrical Engineering, Computer Science and Informatics (EECSI)*, 2022: IEEE, pp. 446-451.
 18. J. Zhang, X. Ge, Q. Li, M. Guizani, and Y. Zhang, "5G millimeter-wave antenna array: Design and challenges," *IEEE Wireless communications*, vol. 24, no. 2, pp. 106-112, 2016.
 19. K. Bangash, M. M. Ali, H. Maab, and R. A. Shaukat, "Effect of embedding H-Shaped slot on the characteristics of millimeter wave microstrip patch antenna for 5G applications," in *2019 2nd International Conference on Computing, Mathematics and Engineering Technologies (iCoMET)*, 2019: IEEE, pp. 1-4.
 20. B. S. Bashar et al., "Antenna beam forming technology based enhanced metamaterial superstrates," in *2022 IEEE 3rd KhPI Week on Advanced Technology (KhPIWeek)*, 2022: IEEE, pp. 1-5.
 21. K. Bangash, M. M. Ali, H. Maab, and H. Ahmed, "Design of a millimeter wave microstrip patch antenna and its array for 5g applications," in *2019 International Conference on Electrical, Communication, and Computer Engineering (ICECCE)*, 2019: IEEE, pp. 1-6.
 22. R. Przesmycki, M. Bugaj, and L. Nowosielski, "Broadband microstrip antenna for 5G wireless systems operating at 28 GHz," *Electronics*, vol. 10, no. 1, p. 1, 2020.
 23. M. Atanasijević-Kunc, V. Kunc, and M. Štiglic, "AUTOMATIC TUNING OF ELECTRICAL SMALL ANTENNAS," *Informacije MIDEM*, vol. 40, no. 3, pp. 174-177, 2010.
 24. Z. Lodro, N. Shah, E. Mahar, S. B. Tirmizi, and M. Lodro, "mmWave novel multiband microstrip patch antenna design for 5G communication," in *2019 2nd International conference on computing, mathematics and engineering technologies (iCoMET)*, 2019: IEEE, pp. 1-4.
 25. Z. Wang, J. Liu, J. Wang, and G. Yue, "Beam squint effect on high-throughput millimeter-wave communication with an ultra-massive phased array," *Frontiers of Information Technology & Electronic Engineering*, vol. 22, no. 4, pp. 560-570, 2021.
 26. I. Laurinavicius, H. Zhu, J. Wang, and Y. Pan, "Beam squint exploitation for linear phased arrays in a mmWave multi-carrier system," in *2019 IEEE Global Communications Conference (GLOBECOM)*, 2019: IEEE, pp. 1-6.
 27. S. Glinsek, V. Furlan, T. Pecnik, M. Vidmar, B. Kmet, and B. Malic, "Elliptically polarized frequency agile antenna on ferroelectric substrate," *Informacije MIDEM*, vol. 48, no. 4, pp. 229-233, 2018.
 28. S. Rangan, T. S. Rappaport, and E. Erkip, "Millimeter-wave cellular wireless networks: Potentials and challenges," *Proceedings of the IEEE*, vol. 102, no. 3, pp. 366-385, 2014.



Copyright © 2024 by the Authors. This is an open access article distributed under the Creative Commons Attribution (CC BY) License (<https://creativecommons.org/licenses/by/4.0/>), which permits unrestricted use, distribution, and reproduction in any medium, provided the original work is properly cited.

Arrived: 17. 01. 2024
Accepted: 22. 03. 2024

Quantum-based serial-parallel multiplier circuit using an efficient nano-scale serial adder

Hongyu Wu¹, Shuai Jiang², Saeid Seyedi³, Nima Jafari Navimipour^{4,5,6}

¹School of Electrical & Mechanical Engineering, Xuchang University, Xuchang, Henan, China

²Xuji Group Co., Ltd. Xuchang, Henan, China

³Department of Computer Engineering, Faculty of Engineering, Bu-Ali Sina University, Hamedan, Iran

⁴Department of Computer Engineering, Faculty of Engineering and Natural Sciences, Kadir Has University, Istanbul, Turkey

⁵Future Technology Research Center, National Yunlin University of Science and Technology, Douliou, Yunlin, Taiwan

⁶Research Center of High Technologies and Innovative Engineering, Western Caspian University, Baku, Azerbaijan

Abstract: Quantum dot cellular automata (QCA) is one of the newest nanotechnologies. The conventional complementary metal oxide semiconductor (CMOS) technology was superbly replaced by QCA technology. This method uses logic states to identify the positions of individual electrons rather than defining voltage levels. A wide range of optimization factors, including reduced power consumption, quick transitions, and an extraordinarily dense structure, are covered by QCA technology. On the other hand, the serial-parallel multiplier (SPM) circuit is an important circuit by itself, and it is also very important in the design of larger circuits. This paper defines an optimized circuit of SPM circuit using QCA. It can integrate serial and parallel processing benefits altogether to increase efficiency and decrease computation time. Thus, all these mentioned advantages make this multiplier framework a crucial element in numerous applications, including complex arithmetic computations and signal processing. This research presents a new QCA-based SPM circuit to optimize the multiplier circuit's performance and enhance the overall design. The proposed framework is an amalgamation of highly performance architecture with efficient path planning. Other than that, the proposed QCA-based SPM circuit is based on the majority gate and 1-bit serial adder (BSA). BCA circuit has 34 cells and a 0.04 μm^2 area and uses 0.5 clock cycles. The outcomes showed the suggested QCA-based SPM circuit occupies a mere 0.28 μm^2 area, requires 222 QCA cells, and demonstrates a latency of 1.25 clock cycles. This work contributes to the existing literature on QCA technology, also emphasizing its capabilities in advancing VLSI circuit layout via optimized performance.

Keywords: Multiplier, Serial-Parallel, Binary multiplier operation, Nano, QCA-based communications

Kvantno vezje zaporedno-paralelnega množilnika z uporabo učinkovitega zaporednega seštevalnika v nano merilu

Izvleček: Kvantni točkovni celični avtomati (QCA) so ena od najnovejših nanotehnologij. Tradicionalno tehnologijo komplementarnih kovinsko oksidnih polprevodnikov (CMOS) je odlično nadomestila tehnologija QCA. Ta metoda uporablja logična stanja za določanje položajev posameznih elektronov in ne definira napetostnih nivojev. Tehnologija QCA pokriva številne optimizacijske dejavnike, vključno z manjšo porabo energije, hitrimi prehodi in izredno gosto strukturo. Po drugi strani pa je vezje serijsko-paralelnega množilnika (SPM) samo po sebi pomembno vezje, zelo pomembno pa je tudi pri načrtovanju večjih vezij. Članek opredeljuje optimizirano vezje SPM z uporabo QCA. V njem lahko združimo prednosti serijske in vzporedne obdelave ter tako povečamo učinkovitost in skrajšamo čas računanja. Zaradi vseh omenjenih prednosti je torej to seštevalno ogrodje ključni element v številnih aplikacijah, vključno s kompleksnimi aritmetičnimi izračuni in obdelavo signalov. V tej raziskavi je predstavljeno novo vezje SPM, ki temelji na QCA, za optimizacijo učinkovitosti vezja množitelja in izboljšanje celotne zasnove. Predlagani okvir je združitev visoko zmogljive arhitekture z učinkovitim načrtovanjem poti. Predlagano vezje SPM, ki temelji na QCA, temelji na večinskih vratih in 1-bitnem zaporednem seštevalniku (BSA). Vezje BCA ima 34 celic in površino 0,04 μm^2 ter porabi 0,5 takta. Rezultati so pokazali, da predlagano vezje SPM, ki temelji na QCA, zavzema le 0,28 μm^2 površine, potrebuje 222 celic QCA in izkazuje zakasnitev 1,25 takta. To delo prispeva k obstoječi literaturi o tehnologiji QCA, pri čemer poudarja tudi njene zmožnosti pri napredku postavitve vezij VLSI prek optimizirane zmogljivosti.

Ključne besede: množilnik, serijsko-vzporedno, binaren množilnik, nano, komunikacije na osnovi QCA

* Corresponding Author's e-mail: 12009044@xcu.edu.cn, JNNima@yuntech.edu.tw

How to cite:

Hongyu Wu et al., "Quantum-based serial-parallel multiplier circuit using an efficient nano-scale serial adder", Inf. Midem-J. Microelectron. Electron. Compon. Mater., Vol. 54, No. 2(2024), pp. 87–93

1 Introduction

Enduring empirical observation in semiconductor technology, exemplified by Moore's Law, outlines the contemporary challenges faced by Very Large-Scale Integration (VLSI). To address these troubling issues, a shift from conventional VLSI computing to molecular, DNA, and quantum computing as some viable alternative options might be helpful. The Quantum-dot Cellular Automata (QCA) is one of these intriguing realization technologies that has garnered greater attention recently (9–13) because of several advantageous qualities. These challenges prompted the solution introduced by Lent in 1997 involving QCA [1]. Moore's Law, established in 1965, signifies the regular doubling of transistors per square inch on integrated circuits and microchips, underpinning the remarkable growth and cost-effectiveness of transistor-based semiconductor technologies such as Complementary Metal-Oxide-Semiconductor (CMOS) and VLSI.

There are examples of actualized quantum circuits that can function at room temperature and are built with semiconductor, magnetic, and molecular technologies. One particularly helpful aspect of QCA technology is that it uses electron interactions—rather than electron flow—to accomplish computation, making it an ultra-low-power implementation method. In comparison to CMOS, it also offers better device density and quicker switching speed. QCA technology is expected to operate in the terahertz frequency domain and attain a density of 10^{12} devices per cm^2 . Because CMOS transistors have constraints in terms of power, area, and performance, QCA technology should be viewed as a promising alternative for implementing complex systems. This is because of all these qualitative qualities [2, 3].

The potential of QCA technology to transform computer usage is generating a lot of excitement. To put it simply, QCA circuits process information by using the power of attraction between electrons, the smallest particles. On the other hand, the Serial-Parallel Multiplier (SPM) is a unique circuit that may be used to solve a wide range of arithmetic problems. Moreover, the SPM takes advantage of QCA technology, which can do many things at once. This helps QCA manage big multiplication tasks really well. A SPM is an important part of QCA technology because it makes it possible to multiply binary numbers in a smart way using the special abilities of QCA cells. Multipliers, especially SPM circuits, are important and essential circuits in QCA technology due to their high speed and accuracy. Based on the issues mentioned, this paper introduces a unique SPM circuit based on QCA. In fact, the primary goal of the presented paper is to design a fast SPM circuit with fast computing capabilities. In fact, this circuit, with its inherent capability of QCA-based computing, tries to

increase the speed, accuracy, and efficiency of the circuits implemented in this technology.

The remaining part of this paper is divided as follows: section 2 is the preliminaries of QCA and related works. Section 3 presents the proposed 1-bit serial adder (BSA) and SPM circuit designs in detail. The simulation and evaluation of the circuits are illustrated in Section 4. Lastly, section 5 concludes the findings of the study and explains the direction of future research.

2 Background

A pair of electrons can be carried across any set of diagonal dots in a QCA cell consisting of four quantum dots. The electrons break into separate points because of the strong potential barrier that exists among every pair of quantum dots. However, the arrangement can be made simpler by using cells with four points; an extra quantum dot can be placed in the cell's center. Because of their high energy, electrons are known to push things. Consequently, the opposite electron is moved to the matching diagonal quantum dot by transferring over the tunneling barrier when one electron moves in the neighboring cells. By going over the tunneling barrier and onto its associated diagonal quantum dot, the other electron is moved to the surrounding cells. The binary numbers 0 and 1 can be assumed to correspond to the two conceivable instances discussed above. [4]. An array of QCA cells makes up the binary wire, which is the fundamental logic component of QCA. Transmitting binary data requires a linear arrangement of the cells. Also, the electrostatic repulsion causes information to flow from input to output. In addition, a diagonal QCA wire is a regular cell that has been rotated. Once it has been rotated, it can likewise be utilized to create a wire [5].

The fundamental components of a QCA are the majority gate, inverter, and QCA wire. The binary value is transferred through Coulombic interactions among cells from input to output. The wire created by cascading cells could be composed of cells orientated at 45 degrees rather than 90 degrees, or it could be arranged in a horizontal row. Furthermore, for QCA cells to properly convey binary signals, they do not need to be in an upright position. Also, the cells that are 90 degrees oriented can be positioned close to cells that are off-centered. This implementation explains the integrated quantum behavior of QCA technology in information processing. QCA is considered a suitable alternative to traditional semiconductor devices [6].

The XOR gate is a fundamental unit in the logical element in QCA for bit-wise manipulation. Usually, it com-

prises a low output (0) if both inputs are low or both are high. On the other hand, if one, and only one, of the inputs to the gate is high, the output will be true (1). Employing coulombic interactions, the XOR logic functions are executed by the QCA XOR gate. Thus, it is of substantial importance in computational systems based on QCA [7].

The QCA-based clocking synchronization system is an important component of nano-scale technology. It determines the efficiency of all computational functions run by the QCA cells. The changes that occur in a clock control system during the clock phase are depicted in four distinct phases. The four phases of the clock—*Switch, Hold, Release, and Relax*—can be changed following how electrons are activated. Hold encodes values 0 and 1, referring to the condition in which the barrier associated with the dot has been increased, inhibiting electron tunneling. The switch involves progressively increasing the barrier corresponding to a dot in an inactivated cell. The release is the state in which the dot barrier is progressively dropped, and Relax is the state in which the barrier decreases, and electron tunneling is made simpler [8].

The fundamental mathematical operations encompass addition, subtraction, division, and multiplication. Out of these, multiplication holds a distinct significance within the context of circuits and digital computing [9]. Multiplication operations find widespread applications in various computational tasks, making them particularly vital. Within processors, multipliers stand as integral components of the arithmetic unit, and their efficiency and speed profoundly impact overall processor performance [10]. The capacity to carry out effective multiplication operations dictates the complexity and speed of processors, so optimizing multipliers is essential to improving the capabilities and efficiency of contemporary processors and digital systems. The standard integer multiplication procedure and binary multiplication are quite similar. The first step is to multiply each binary number's digit by the digit of another binary number. Then, finally, total them all to obtain the outcome. The result is a binary number representing the product of the multiplicand and multiplier. Binary multipliers are integral in digital systems, particularly in microprocessors and digital signal processing, where they perform essential tasks such as integer and fixed-point multiplication, making them a fundamental component of binary arithmetic [11].

2.1 Related works

In this section, the previous designs presented for the SPM circuit have been reviewed.

Edrisi Arani and Rezai [12] proposed the design of a serial-parallel multiplier in quantum-dot cellular automata technology. A new serial-parallel QCA multiplier circuit based on an effective full-adder circuit design was presented and evaluated in this paper. The QCA full-adder circuit was constructed using 31 cells that had an area of $0.03 \mu\text{m}^2$ and a delay of 0.5 clock cycles. It also featured a majority gate and a three-input XOR gate. The 4×4 QCA SPM was designed by 264 QCA cells that use 0.75 clock cycle latency and a $0.27 \mu\text{m}^2$ of area. In this article, QCADesigner 2.0.3 was used to implement the circuits and test them, and the results showed the accuracy of the circuits.

Bahar and Wahid [9] presented and investigated an SPM circuit along with energy analysis. The authors have used a new XOR and a majority gate to design a BSA circuit. The presented XOR gate has used the Coulombic repulsion property of QCA technology. This gate was used in designing circuits of 4-, 8-, 16-, 32-, and 64-bit multipliers. The circuits that were presented were designed and tested by QCADesigner and QCAPro simulators, and the results, according to the researchers, reduced the space consumption and the number of cells compared to previous designs. It is worth mentioning that the QCAPro simulator has been used to determine the energy dissipation of the implemented circuit.

Ahmadpour, et al. [13] presented the design of a multiplier for use in nano-scale IoT systems using atomic silicon. In fact, this article examined an ASiQD-based multiplier circuit for efficient power management in micro-IoT devices. The 4×4 -bit multiplier array was designed with the SiQAD simulation tool technology to reduce space consumption and energy consumption. This circuit and design have significantly reduced energy consumption and space consumption in IoT devices compared to most existing designs.

Also, Premananda, et al. [14] proposed a 4-bit SPM based on QCA. Compared to multipliers that use more complex multiplication methods, SPMs have a simple and scalable architecture. The present paper has proposed a 4-bit SPM circuit based on QCA, which was optimal in energy and area. Using the 4 multipliers, a 4-bit SPM was designed and QCADesigner-E was used to design, analyze, and simulate proposed circuits. This tool used the number of cells, area, and energy that have been used to evaluate the designed circuits. The simulation results showed that compared to the reference architectures, the proposed 4-bit SPM minimizes the number of cells, area, and energy dissipation.

Finally, Sekar, et al. [15] proposed a high-speed SPM in QCA. In addition, in this paper, 4-bit SPM, shift registers, and adders were implemented based on QCA cells.

Shift registers were added to the circuit for parallel and serial computations, to store inputs and outputs, and to improve circuit output stability. The implementation of SPM with shift registers to store input and output in QCA was presented for the first time in this article. Compared to current designs, the proposed multiplier without a shift register was at least 66% faster and more efficient. The 4-bit shift register multiplier had had 2271 cells with a 7.74 μm^2 size and a 25.25 clock cycle latency.

3 Proposed design

An SPM is a digital circuit used to multiply two binary numbers. It combines both serial and parallel processing techniques to perform multiplication efficiently. This type of multiplier is essential in the context of QCA technology, which is an emerging nano-scale computing technology with potential applications in future high-performance and energy-efficient computing systems. In mode a serial-parallel processing is as follows:

Serial Processing: In a serial-parallel multiplier, the multiplication process begins with serial processing, where the bits of one of the operands (*usually the multiplier*) are processed one by one. The other operand (*the multiplicand*) remains fixed during this phase.

Parallel Processing: After serial processing, the multiplier is processed in parallel, meaning multiple bit-wise multiplications occur simultaneously. These parallel multiplication results are then added together to obtain the final product.

Given that, QCA is a novel computing paradigm that utilizes quantum phenomena at the nano-scale level to perform logic and computation. In QCA, information is represented and processed using the quantum properties of electron charge and Coulombic interactions between quantum dots. Unlike conventional CMOS technology, QCA exhibits potential as a technology that holds significant promise for realizing digital logic at the nano-scale. It is a kind of nanotechnology designed specifically for developing computational circuits. Also, some of its attributes, such as less occupied area and lower latency, render it a suitable alternative when compared to the nano-scale CMOS technology. The repulsion between QCA cells and how to communicate between them are fundamental challenges in the design of nanomultipliers for QCA technology. Older multipliers designed using CMOS technology cannot be used for QCA technology because they use Coulombic repulsion. It should be noted that SPMs are particularly important in QCA technology because they can exploit

the inherent parallelism of QCA cells while the input data are serial and perform calculations.

In addition, the SPM circuit significantly performs complex binary multiplication operations, and this important feature makes this circuit a major element in nanocomputing. Thus, all these advantages make this multiplier framework a crucial element in numerous applications, including complex arithmetic computations and signal processing. Also, QCA-based systems often require scalability to handle larger data sizes and more complex computations. SPM can be designed with scalability, making them suitable for various QCA-based computing needs.

To implement the proposed SPM circuit presented in this article, we applied a BSA, which includes an XOR gate and a majority gate. We have made changes to connect one of its inputs to the carry output, as shown in Figure 1, and this connection goes through a 0.5-clock cycle. This circuit has 34 cells and a 0.04 μm^2 area.

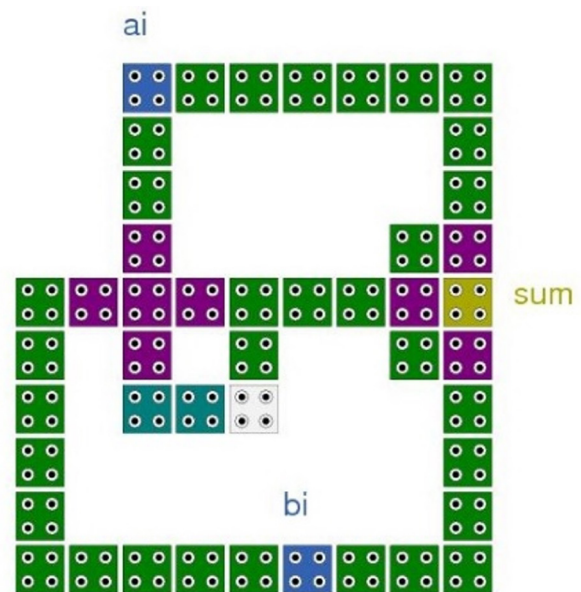


Figure 1: The proposed BSA.

In the pursuit of performance improvements, particularly in terms of reducing circuit area and minimizing cell count, an efficient architecture is utilized, incorporating one-layer crossovers as the selected design strategy. It's essential to note that in scenarios where minimizing signal delay is critical, the integration of one-layer crossovers proves effective for optimizing circuit efficiency. A high-speed BSA serves as the foundational component for creating a high-speed SPM circuit. Notably, the traditional BSA architecture has been enhanced, specifically involving the establishment of feedback connections that link the carry input and out-

put. This innovative design enables the carry output of the BSA to serve as an input for the same BSA, a feature instrumental in designing the QCA SPM circuit. A visual representation of the developed QCA SPM circuit can be found in Figure 2, while Figure 3 provides a detailed layout illustration of this circuit.

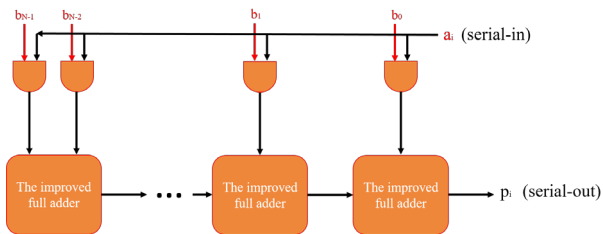


Figure 2: Block diagram of the developed SPM circuit

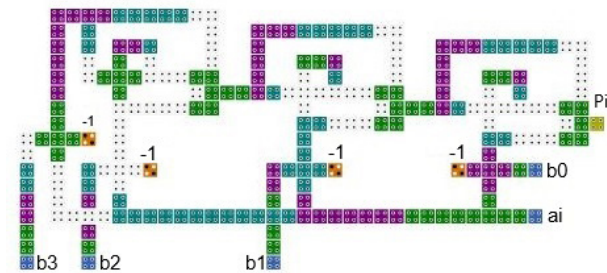


Figure 3: QCA design of the developed SPM circuit

Figure 3 shows the QCA-based design of the developed SPM circuit. It is demonstrated that this circuit is implemented in one layer, and the majority gates and BSAs are located in the main layer. In the provided circuit, access to inputs and outputs is very easy to use. With 1.25 clock cycles and a 0.28 μm^2 area, the proposed QCA SPM circuit comprises 222 cells.

4 Simulation tools and results

Utilizing QCA technology, QCADesigner 2.0.3 is an all-inclusive and adaptable software application employed for the simulation and fabrication of digital circuits. This academic application is meticulously customized to address the particular demands and complexities of QCA-based circuit layouts, presenting scientists and developers with indispensable resources for investigating the futuristic possibilities of this emergent nanoelectronics paradigm. The QCA circuits are designed and simulated using the QCADesigner tool version 2.0.3 using the *bistable approximation* default simulation engine. The area and clock analysis are carried out using the QCADesigner [16-18].

Figure 4 shows the simulation and test outcomes of the proposed 1-bit BSA circuit in QCA, and these results

confirm the correctness of the proposed circuit. In addition, a pair of inputs and the output is reached after 0.5 clock cycles. Figure 5 also shows the simulation and test outcomes, and these results confirm the proposed SPM circuit is working well. In addition, a pair of inputs and the output is reached after 1.25 clock cycles. All the output results are consistent with the results of the correctness table (Table 1), indicating the presented circuit’s accuracy.

On the other hand, Table 2 summarizes the simulation results of the developed QCA BSA and SPM circuits compared to other QCA circuits. According to the comparison results, it is quite visible that the presented circuits have fewer consumption cells and less consumption space than the previous designs due to their one-layers.

Table 1: The truth table of the proposed BSA

ai	bi	Majority gate output	Sum
0	0	0	0
0	1	0	1
1	0	0	1
1	1	1	1
0	0	0	0
0	1	0	1
1	0	0	1
1	1	1	1

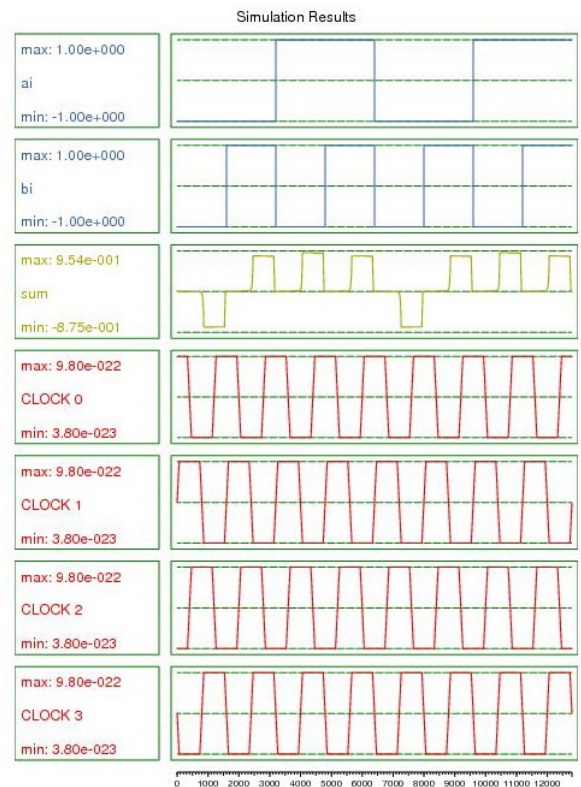


Figure 4: The proposed BSA circuit simulation results

Table 2: Comparisons of multiplier circuits

Designs	Area (μm^2)	Cells	Latency
Cho and Swartzlander [19]	0.493	406	1
Zhang, et al. [20]	0.299	329	1
Zhang, et al. [20]	0.319	330	1.25
Edrisi Arani and Rezai [12]	0.27	264	1.75
Bahar and Wahid [9]	0.243	229	1.25
Proposed BSA design	0.04	34	0.5
Proposed SPM design	0.28	222	1.25

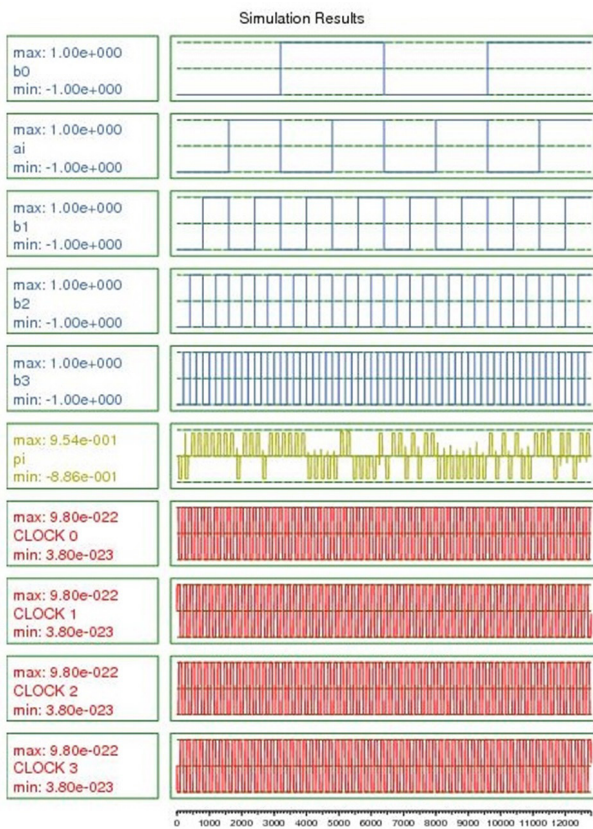


Figure 5: The proposed SPM circuit simulation results.

5 Conclusion and future works

The unique features of QCA, such as their low occupancy and ultralow power consumption, make them particularly attractive candidates for nano-scale technology. Also, BSA and SPM are widely used as building elements in arithmetic circuits. An essential part of digital computing is an SPM because it can efficiently perform complex binary multiplication operations. An efficient BSA gate and SPM circuit in QCA computational circuits can significantly improve efficiency. Therefore, this paper proposes one approach for designing the SPM circuit utilizing a BSA gate. The suggested SPM circuit was validated and simulated. We demonstrated the suggested SPM circuit's functioning. In addition, the

number of cells, delay, and space consumption of the suggested SPM circuit are obtained using QCAdesigner. This SPM circuit is designed with 222 quantum cells. The outcomes show the suggested QCA-based SPM circuit occupies a mere $0.28 \mu\text{m}^2$ area. This circuit has 1.25 clock cycles to create output. Based on the number of cells, occupied area, and latency, the findings showed that the suggested designs work as intended. The suggested SPM appears to offer a workable substitute for the current architecture and is scalable. This circuit may be utilized in larger circuits since it generates n -bit QCA SPM using the suggested QCA SPM.

6 Conflict of interest

The authors declare no conflict of interest.

7 References

1. A. Kamaraj, P. Marichamy, and R. Abirami, "MULTI-PORT RAM DESIGN IN QCA USING LOGICAL CROSSING," *Informacije MIDEM*, vol. 51, no. 1, pp. 49-61, 2021.
2. S. Senthilnathan and S. Kumaravel, "Power-efficient implementation of pseudo-random number generator using quantum dot cellular automata-based D flip flop," *Computers & Electrical Engineering*, vol. 85, p. 106658, 2020.
3. M. Vahabi, E. Rahimi, P. Lyakhov, and A. Otsuki, "A novel QCA circuit-switched network with power dissipation analysis for nano communication applications," *Nano Communication Networks*, vol. 35, p. 100438, 2023.
4. S. Seyedi and N. J. Navimipour, "An optimized design of full adder based on nano-scale quantum-dot cellular automata," *Optik*, vol. 158, pp. 243-256, 2018.
5. S. Seyedi and N. Jafari Navimipour, "Designing a multi-layer full-adder using a new three-input majority gate based on quantum computing," *Concurrency and Computation: Practice and Experience*, vol. 34, no. 4, p. e6653, 2022.
6. S. Seyedi and N. J. Navimipour, "A fault-tolerant image processor for executing the morphology operations based on a nano-scale technology," *Multimedia Tools and Applications*, vol. 82, no. 2, pp. 2489-2502, 2023.
7. S. B. Tripathi, A. Narzary, R. Toppo, M. Goswami, and B. Sen, "Designing efficient configurable QCA nano circuit for morphological operations in image processing," in *Journal of Physics: Conference Series*, 2018, vol. 1039, no. 1: IOP Publishing, p. 012028.

8. R. Marshal and G. Lakshminarayanan, "Fault resistant coplanar QCA full adder-subtractor using clock zone-based crossover," *IETE Journal of Research*, vol. 69, no. 1, pp. 584-591, 2023.
9. A. N. Bahar and K. A. Wahid, "Design of QCA-serial parallel multiplier (QSPM) with energy dissipation analysis," *IEEE transactions on circuits and systems II: express briefs*, vol. 67, no. 10, pp. 1939-1943, 2019.
10. K. R. Sekar, R. Marshal, and G. Lakshminarayanan, "Reliable adder and multipliers in QCA technology," *Semiconductor Science and Technology*, vol. 37, no. 9, p. 095006, 2022.
11. S. Mohammadi Mohaghegh, R. Sabbaghi-Nadooshan, and M. Mohammadi, "Design of a ternary QCA multiplier and multiplexer: a model-based approach," *Analog Integrated Circuits and Signal Processing*, vol. 101, pp. 23-29, 2019.
12. I. Edrisi Arani and A. Rezai, "Novel circuit design of serial-parallel multiplier in quantum-dot cellular automata technology," *Journal of Computational Electronics*, vol. 17, no. 4, pp. 1771-1779, 2018.
13. S.-S. Ahmadpour, A. Heidari, N. J. Navimpour, M.-A. Asadi, and S. Yalcin, "An efficient design of multiplier for using in nano-scale IoT systems using atomic silicon," *IEEE Internet of Things Journal*, 2023.
14. B. Premananda, U. Bhargav, and K. S. Vineeth, "Design and analysis of compact QCA based 4-bit serial-parallel multiplier," in *2018 International conference on electrical, electronics, communication, computer, and optimization techniques (ICEEC-COT)*, 2018: IEEE, pp. 1014-1018.
15. K. R. Sekar, R. Marshal, and G. Lakshminarayanan, "High-speed serial-parallel multiplier in quantum-dot cellular automata," *IEEE Embedded Systems Letters*, vol. 14, no. 1, pp. 31-34, 2021.
16. A. M. Chabi, S. Sayedsalehi, S. Angizi, and K. Navi, "Efficient QCA exclusive-or and multiplexer circuits based on a nanoelectronic-compatible designing approach," *International Scholarly Research Notices*, vol. 2014, 2014.
17. K. Walus, T. J. Dysart, G. A. Jullien, and R. A. Budiman, "QCADesigner: A rapid design and simulation tool for quantum-dot cellular automata," *IEEE transactions on Nanotechnology*, vol. 3, no. 1, pp. 26-31, 2004.
18. K. Walus, "ATIPS Laboratory QCADesigner Homepage. ATIPS Laboratory, Univ. Calgary, Calgary, Canada," ed, 2002.
19. H. Cho and E. E. Swartzlander, "Adder and multiplier design in quantum-dot cellular automata," *IEEE Transactions on Computers*, vol. 58, no. 6, pp. 721-727, 2009.
20. Y. Zhang, H. Lv, H. Du, C. Huang, S. Liu, and G. Xie, "Modular design of QCA carry flow adders and

multiplier with reduced wire crossing and number of logic gates," *International Journal of Circuit Theory and Applications*, vol. 44, no. 7, pp. 1351-1366, 2016.



Copyright © 2024 by the Authors. This is an open access article distributed under the Creative Commons Attribution (CC BY) License (<https://creativecommons.org/licenses/by/4.0/>), which permits unrestricted use, distribution, and reproduction in any medium, provided the original work is properly cited.

Arrived: 16. 11. 2023

Accepted: 12. 04. 2024

A Multiband Meanderline Rectenna: Design and Simulation for Enhanced Performance

Vishnu Raghuthaman Nedungadi¹, Vidhyapriya Ranganathan²

¹Dept. of Biomedical Engineering, PSG College of Technology, Coimbatore, Tamil Nadu, India

²Dept. of Biomedical Engineering, PSG College of Technology, Coimbatore, Tamil Nadu, India

Abstract: This research article presents design, simulation and analysis of a novel meanderline microstrip patch rectenna to harvest energy from the 2.4 GHz and 5.0 GHz frequency bands. The research is approached in two stages. In the first stage, a meanderline microstrip patch antenna offering improved bandwidth, radiation characteristics, and impedance matching is considered. The antenna is constructed on an FR4 substrate, with the radiating patch positioned between the substrate and a solid ground plane. A feedline strip is incorporated in the radiating patch to excite the antenna. An impedance-matching network was designed and implemented in the simulation. A multiband rectifier is utilized to convert RF power into usable output DC voltage. HSMS 2850 Schottky diodes are used to further improve efficiency. The performance of the proposed system is evaluated using Keysight Advanced Design System, taking into account metrics like return loss, radiation pattern, output voltage, and power harvesting efficiency. The proposed rectenna achieved a bandwidth of 1.2 GHz, with a gain of 3.56 dBi at 2.40 GHz and 8.06 dBi at 5.02 GHz. The rectenna demonstrated an output voltage of 3.65 V at an input power level of 30 dBm and -2 mV at -5 dBm input power level. A peak conversion efficiency of 83% was obtained for the overall system. The analysis of simulation and experimental results demonstrated an improved performance of the antenna in terms of increased bandwidth and enhanced power harvesting capabilities.

Keywords: Meanderline Antenna, Rectenna, Impedance Matching, RF Energy Harvesting

Večpasovna Meanderline rektena: načrtovanje in simulacija za večjo zmogljivost

Izveček: Članek predstavlja zasnovo, simulacijo in analizo nove meandrske mikropasne usmerniške antene za zbiranje energije iz frekvenčnih pasov 2,4 GHz in 5,0 GHz. Raziskava je potekala v dveh fazah. V prvi fazi je obravnavana meandrska mikropasna antena z izboljšano pasovno širino, sevalnimi lastnostmi in impedančno usklajenostjo. Antena je izdelana na podlagi FR4, pri čemer je sevalna krpica nameščena med podlago in ozemljitveno ravnino. Za vzbujanje antene je v sevalno krpico vgrajen trak napajalne linije. Za pretvorbo radijske energije v uporabno izhodno enosmerno napetost se uporablja večpasovni usmernik. Za dodatno izboljšanje učinkovitosti so uporabljene Schottkyjeve diode HSMS 2850. Delovanje predlaganega sistema je ocenjeno z uporabo sistema Keysight Advanced Design System, pri čemer so upoštevani kazalniki, kot so povratne izgube, sevalni vzorec, izhodna napetost in učinkovitost zbiranja energije. Predlagana rektena je dosegla pasovno širino 1,2 GHz z ojačitvijo 3,56 dBi pri 2,40 GHz in 8,06 dBi pri 5,02 GHz. Rektena je pokazala izhodno napetost 3,65 V pri vhodni moči 30 dBm in -2 mV pri vhodni moči -5 dBm. Največji izkoristek pretvorbe celotnega sistema je bil 83 %. Analiza simulacijskih in eksperimentalnih rezultatov je pokazala izboljšano delovanje antene v smislu povečane pasovne širine in izboljšanih zmogljivosti zbiranja energije.

Ključne besede: meanderska antena, rectenna, impedančno ujemanje, RF zbiranje energije

* Corresponding Author's e-mail: vishnunedungadi@gmail.com

1 Introduction

In recent years, there has been a growing demand for sustainable and self-powered systems in various fields, ranging from wireless sensor networks to wearable

electronics. This demand has led to extensive research in the field of energy harvesting, which aims to convert ambient energy sources into usable electrical energy. Among the various energy harvesting techniques,

How to cite:

Vi. R. Nedungadi et al., "A Multiband Meanderline Rectenna: Design and Simulation for Enhanced Performance", Inf. Midem-J. Microelectron. Electron. Compon. Mater., Vol. 54, No. 2(2024), pp. 95–106

electromagnetic energy harvesting using antennas has garnered considerable attention due to its ability to scavenge energy from the surrounding electromagnetic field [1]. Microstrip antennas have gained significant popularity in wireless communication applications due to their compact size, low profile, and ease of integration [2-6]. However, traditional microstrip patch antennas face challenges such as limited bandwidth and low efficiency, making them less suitable for energy harvesting applications where maximizing power transfer efficiency is of paramount importance. [7-10]. Therefore, there is a need for novel antenna designs that can address these limitations and enable efficient energy harvesting.

Recent research in the domain of RF energy harvesting has been finding an increased focus to impart multi-band resonance behaviour in microstrip antennas [11-13]. This technique enables an increase in the overall efficiency of the receiving antenna without necessitating any expansion in its dimensions. [12]. This behaviour is achieved by incorporating modifications in the architecture of the antenna, such as the introduction of slots, split ring resonators, parasitic patch [12], defected ground, fractal components etc. [1, 3, 4, 14-18].

Another approach to improve the efficacy of microstrip patch antennas for energy harvesting is the incorporation of meanderline structures. Meanderline structures are periodic geometrical patterns that are introduced into the radiating patch, ground plane, or both of the antenna. These structures effectively increase the electrical length of the antenna within a limited physical footprint, thereby enhancing the antenna's bandwidth and radiation characteristics [19, 20]. The meanderline antennas offer several advantages over conventional designs, such as increased bandwidth, improved impedance matching, and enhanced radiation efficiency. These characteristics make the meanderline antenna an appropriate choice to provide efficient and compact solutions for energy harvesting in wireless communication systems.

This research article aims to investigate the application of meanderline rectennas to harvest energy from 4G, Wi-Fi and WLAN frequency bands. The main objective is to design, optimize, and characterize a meanderline microstrip patch antenna that exhibits improved performance in terms of bandwidth and power harvesting efficiency. The design parameters, such as meanderline geometry, the thickness of substrate material, and variations in the geometry of the feedline will be explored to achieve the desired antenna performance. Keysight Advanced Design Systems 2019 is used to analyze the antenna's characteristics, including return loss, radiation pattern, and power harvesting efficiency.

The primary contributions of this research work are as listed below:

- a. The work focuses on the design methodology and simulation of a novel multiband slotted meanderline microstrip antenna intended for RF energy harvesting from the surrounding environment. The obtained results are compared with existing state-of-the-art works to validate the effectiveness and performance of the proposed antenna design.
- b. Parametric variations on the length, height, and width of the various elements that make up the meanderline structure are considered to identify the optimal dimensions of the overall structure
- c. Suitable impedance matching network and a rectifier-doubler have been developed to convert the captured ambient RF energy into output voltage in DC form.

The proposed architecture of the microstrip meanderline rectenna is simulated and then optimised. The findings of this research article are intended to contribute to the advancement of meanderline microstrip patch rectenna as a viable solution for energy harvesting in wireless communication systems and low-power electronic devices. The improved performance and compactness of these antennas will enable the development of self-powered devices, wireless sensor networks, and IoT applications

The article is arranged as follows. Section 2 discusses the design evolution of the proposed antenna in detail. The impact of modifications in the feedline's length and width, as well as variations in the substrate's thickness, on the proposed antenna's general performance, is also examined. In section 3, an analysis of the performance of the antenna along with that of the impedance matching network and the rectifier-doubler circuit is presented. The potential and the performance of the proposed antenna is summarized in section 4.

2 Materials and methods

The multiband antennas are extremely prevalent in RF energy harvesting applications for their capability to collect energy from different frequency bands. Meanderline antennas exhibit capabilities to address the requirements of such systems [21-26]. These antennas enables wideband operation in addition to the multi-band resonance and good radiation efficiency.

To satisfy the performance criteria for energy harvesting applications, the design of the proposed antenna prioritizes the attainment of acceptable values for parameters like return loss and bandwidth. To achieve

this, modifications are made to the meanderline structure of the antenna, and an impedance-matching network along with a rectifier-voltage doubler circuit is integrated. These additional components enable efficient RF-DC conversion, contributing significantly to the overall efficiency of the antenna system.

The design of the proposed rectenna is covered in two sections. In the initial stage, a patch antenna is considered with 2.4 GHz as the centre frequency to obtain the overall dimensions of the patch. The following design equations from [27] have been utilized for this purpose.

$$w = \frac{c}{2f_{res}} \sqrt{\frac{2}{1 + \epsilon_r}} \tag{1}$$

$$L = \frac{c}{2f_{res}} - 2\Delta l \tag{2}$$

$$\Delta l = 0.412h \left\{ \frac{(0.3 + \epsilon_{eff})(0.264 + w/h)}{(\epsilon_{eff} - 0.258)(0.8 + w/h)} \right\} \tag{3}$$

$$\epsilon_{eff} = \frac{\epsilon_r + 1}{2} + \frac{\epsilon_r - 1}{2} \left\{ 1 + 12h/w \right\}^{-1/2} \tag{4}$$

where w – patch width, L – patch length, c – speed of light, f_{res} – resonant frequency, ϵ_r – relative permittivity of the substrate, h – thickness of the substrate, and ϵ_{eff} – effective permittivity of the substrate.

A primitive meanderline antenna is designed initially. The meanderline structure is modified in consequent stages of the design evolution of the antenna. The Keysight Advanced Design System (ADS) software is utilized to design, simulate and analyze the antenna’s performance characteristics. Each modification performed on the structure of the primitive meanderline antenna is carefully examined to understand its impact on the antenna’s performance. The decision to proceed with the next modification is contingent upon the evaluation of the current design stage. Primarily, return loss (S_{11} parameter) and bandwidth are taken into account to make this decision.

Return loss is a crucial parameter that indicates the level of impedance mismatch. In antennas, a higher value of return loss points to an increased power loss due to reflection. The second parameter, bandwidth represents the range of frequency over which the antenna can function is also taken into account. These parameters are estimated at each stage of design evolution

Table 1: Progression of the design evolution of the proposed antenna.

Design Step	Antenna Design Evolution		Return Loss, S_{11} (dB)	Bandwidth (GHz)	Remarks
1	Primitive Meanderline Design		-22.48 dB at 2.43 GHz	(2.35 - 2.65) GHz	300 MHz total bandwidth obtained. However, multi-band resonance was not observed in this design.
2	Meanderline Antenna with slots of equal lengths		-36.60 dB at 2.57 GHz	(2.51 - 2.67) GHz	A bandwidth of 570 MHz bandwidth obtained. A shift in the frequency resonance to the right was observed. Slight resonance was observed at 4 GHz and 5 GHz range
3	Meanderline antenna with slots of increasing lengths		(4.08 – 4.29) GHz	(4.08 – 4.29) GHz	The bandwidth considerably increased to 1.21 GHz. The return loss value at the higher frequency range can be improved
4	Meanderline antenna with no slot in the first line		(5.47 – 5.67) GHz	(5.47 – 5.67) GHz	A bandwidth of 1.09 GHz was observed. The slight reduction comes at the expense of a better return loss value over the range of frequencies
5	Meanderline antenna with slots of increasing lengths and equal slots at the turns		-23.97 at 2.43 GHz and -18.16 dB at 4.82 GHz	(2.2 – 2.67) GHz	The overall bandwidth has increased to 1.1 GHz. Also, considerable improvement in the return loss value for the two ranges of frequency were also observed

to obtain acceptable performance characteristics over the desired frequency range. A comprehensive explanation of this iterative process is provided in the results and discussion section.

The substrate material and its thickness as well as the dimensions of the feedline strip are significant in the design of the microstrip antenna. The dielectric constant, $\epsilon_{r'}$ of the substrate material determines the effective wavelength, the characteristic impedance of the transmission line, and the velocity [28-30]. The resonant frequency of the antenna is influenced by the thickness of the material, with a higher thickness resulting in a lower resonant frequency. Also, a thicker substrate shall result in a narrower radiation pattern and bandwidth [5, 31, 32]. The variations in the dimensions of the feedline strip affect the performance of the antenna in a similar fashion. Improper design of the feedline strip directly contributes to impedance mismatch, reduced efficiency and introduces cross-polarisation in the radiation patterns [33-35].

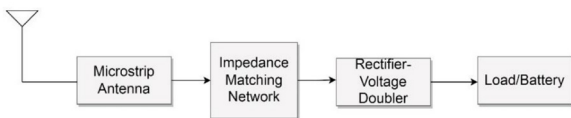


Figure 1: RF energy harvesting system - Block diagram

Proceeding with the rectenna design, the subsequent stage entails the design and integration of an impedance-matching network and a rectifier-voltage doubler circuit for the antenna. A block diagram depicting the overall RF energy harvesting system is shown in figure 1. The impedance-matching network is designed to facilitate the maximum transfer of power from the antenna to the rectification circuit. The rectification–voltage doubler circuit acts as an RF-DC converter and provides DC voltage as output to the load. In the rectifier topology, the rectifier circuit is connected to a Schottky diode. When designing an RF energy harvester, it is preferable to use a rectifier circuit based on CMOS and Schottky diodes [7, 9-11, 13-17, 33, 35].

2.1 Design progression of the proposed meanderline antenna

Table 1 illustrates the progression of design evolution of the proposed antenna. At each stage of evolution, the return loss and bandwidth are keenly observed to understand the effectiveness of the antenna design. Figure 2 depicts the S11 vs frequency plot for each stage of design evolution. A primitive meanderline structure is initially considered. This was developed to harvest from the 2.4 GHz Wi-Fi band.

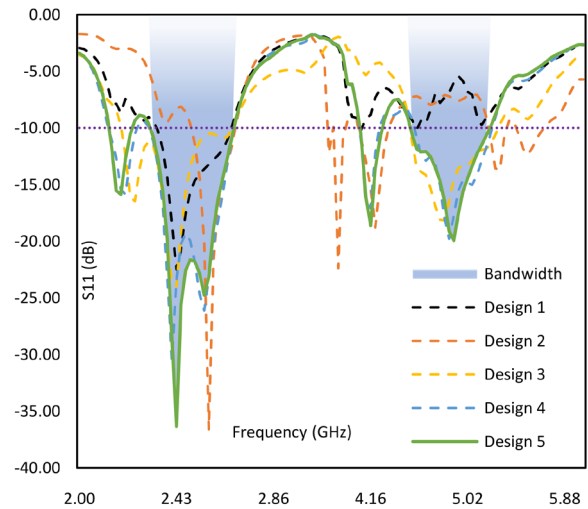


Figure 2: S11 vs Frequency plots for each stage of design evolution

The primitive meanderline antenna exhibited an overall bandwidth of 300 MHz and the minimum value of return loss was observed at 2.43 GHz. In this design stage, multiband resonance was not observed. To achieve this trait, slots were introduced in the design. The simulated results showed that multiband resonance was achieved and the bandwidth had increased by 700 MHz. However, the return loss values at the higher frequencies were observed to be close to -10.00 dB reference line. This suggests that though the antenna exhibited multiband resonance, the performance is affected at the higher end of the frequency range.

To improve this condition while maintaining the overall bandwidth, the lengths of the slots were varied. It was found that by having slots of increasing lengths (traversing from bottom to top), the required performance of the antenna results showed that multiband resonance was achieved and the bandwidth had increased by 700 MHz. However, the return loss values at the higher frequencies were observed to be close to -10.00 dB reference line. This suggests that though the antenna exhibited multiband resonance, the performance is affected at the higher end of the frequency range. This is depicted in the third stage of design evolution.

Data from Table 1 indicates that the return loss of the proposed antenna at the third stage is higher than the return loss value obtained initially. This suggests a scope for improving the performance of the antenna still exists. Upon studying the effect of slots on the overall performance, it was found that the slot in the lowest horizontal section of the meanderline had a detrimental influence. Hence, in the 4th stage of design evolution, a design without the presence of this slot is

considered. The simulated results confirmed the same. The return loss value was observed to have dropped to -30.44 dB and the bandwidth stood at 1.09 GHz at this stage.

The addition of slots in the 5th stage of design evolution is implemented to improve the overall bandwidth and the S11 values in the target frequency range. This modification reduced the return loss to -36.35 dB at 2.43 GHz and improved the bandwidth by 200 MHz. The S11 value at 5.5 GHz also dropped, by a very small margin, to -20.00 dB due to the addition of these slots.

Since the desired return loss and bandwidth values were achieved in this stage, design at the fifth stage of evolution was finalized. Figure 3 shows the final form of the antenna design evolution. Table 2 gives the value of lengths and widths of each component of the antenna.

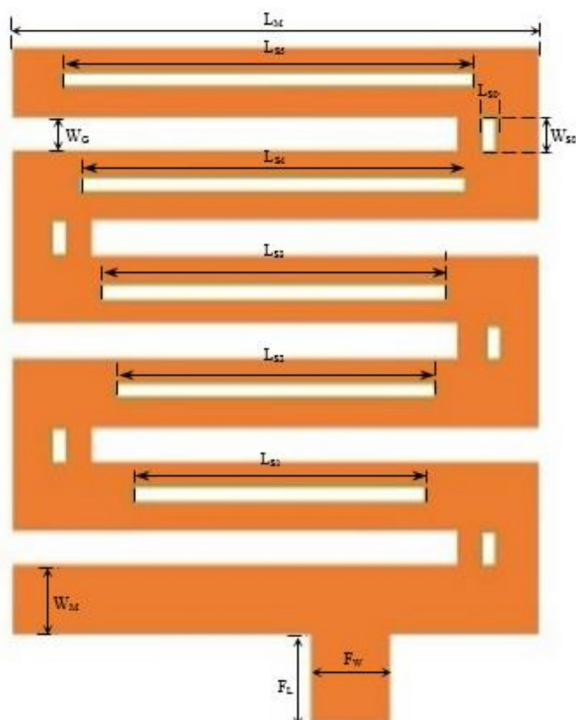


Figure 3: Final form of antenna design evolution

2.1.1 Effect of substrate thickness

In the proposed antenna, FR4, a flame retardant glass epoxy laminate, is used as the substrate material. FR4 is widely recognized for its stability, durability, and cost-effectiveness, making it a popular choice in various electronic applications. With the goal of identifying the ideal thickness of the substrate at which the antenna offers the desired performance characteristics, several thicknesses of the substrate are taken into consideration.

Table 2: Dimensions of the proposed antenna

Parameter	Dimension (mm)
L_M	50
W_G	4
F_W	8
L_{S4}	40
L_{S1}	25
L_{S0}	1.5
W_{S0}	4
F_L	7
L_{S3}	35
W_{S1}	2
W_M	6
H_T	16
L_{S5}	45
L_{S2}	30
W_{S2}	2

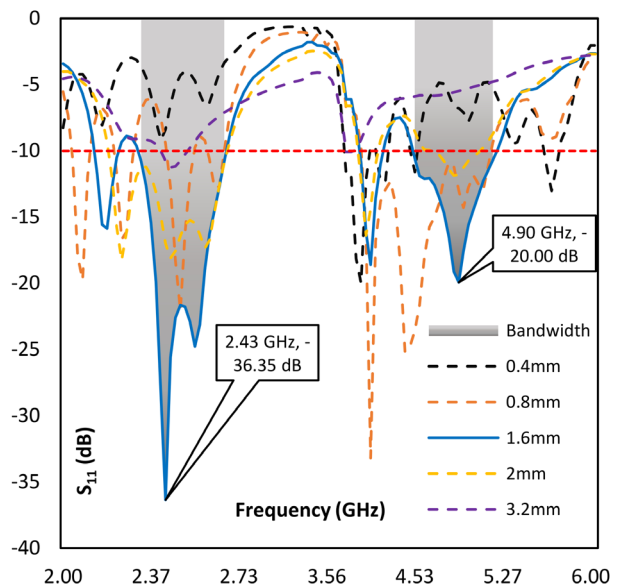


Figure 4: S11 vs Frequency plot for varying thickness of dielectric material

Figure 4 shows the performance of the proposed antenna to varying thicknesses of the substrate material. It can be understood from this plot that the reflection coefficients varied greatly with variations in the thickness of the dielectric material. The best performance of the antenna was achieved at a thickness of 1.6 mm. At this thickness, the return loss value was observed to be -36.35 dB at 2.43 GHz and -20.00 dB at 4.93 GHz. The overall bandwidth was observed to be 1.10 GHz.

2.1.2 Effect of feedline strip

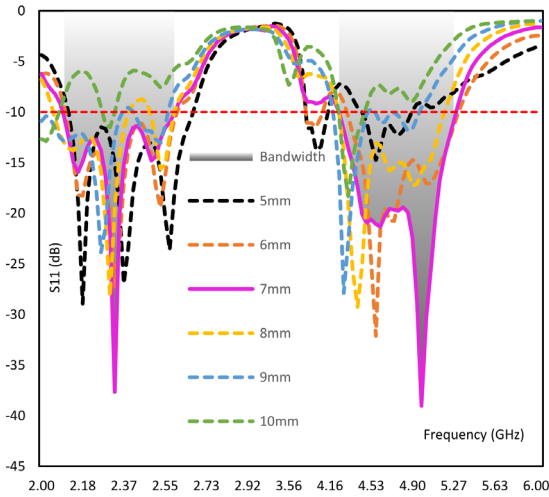


Figure 5: S11 vs Frequency plot for varying length of feedline strip

To identify the optimal length of the feedline strip in the proposed antenna, the length of the feedline is varied from 4 mm to 25 mm. The return loss versus frequency plot depicting this variation is shown in Figure 5. An analysis similar to that of the effect of variation in dielectric thickness was performed. During this analysis, close attention is given to the observed return loss and bandwidth values. The optimal performance of the antenna was obtained at a length of 7 mm of the feedline strip. Though comparable bandwidths were observed with 6 mm and 8 mm lengths, the value of S11 parameter was found to be inferior in these cases. Hence, the 7 mm length is finalized for the design.

3 Results and discussions

The performance of the proposed antenna along with that of the impedance matching network and rectifier-doubler circuit is discussed in this section. The proposed antenna is fabricated on a double-sided copper sheet based on a FR4 substrate. A visual representation of the front and rear of the proposed antenna is shown in figure 6.

Parameters like gain, radiation pattern, efficiency, and output voltage are utilized to estimate the overall performance of the RF energy harvesting system. To evaluate the reflection coefficient (S11) of the MMA, Keysight Fieldfox N9926A vector network analyzer was utilized. The radiation patterns of the antenna were obtained by performing tests in an anechoic chamber.



(a) – Front (b) – Rear

Figure 6: Proposed Antenna

A transmitting horn antenna with a gain of 15 dBi along with a RF signal Generator was used for the tests. The experimental setup is as shown in figure 7. The Device-under-Test (Proposed Antenna) is placed at a distance of 1.5m from the Horn Antenna.

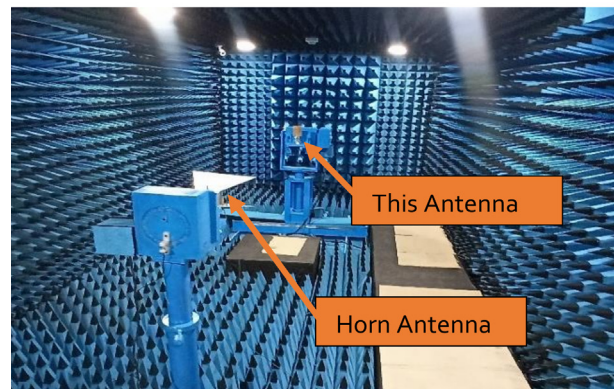


Figure 7: Experimental Setup Inside the Anechoic Chamber

3.1 Performance analysis of the proposed antenna

The return loss curve of an antenna, depicted in Figure 8, displays the relationship between return loss and frequency, integrating results from both simulation and measurement. At 2.37 GHz, the S11 value was recorded at -28.3 dB, while at 5.1 GHz, it measured -25.7 dB. This analysis reveals an overall bandwidth of 1.1 GHz based on the observed data.

The variation in the value of gain of the proposed antenna across the desired frequency range can be observed in Figure 9. A maximum gain of 8.06 dBi was observed at 5.02 GHz. At 2.4 GHz, the value of gain was observed to be 3.56 dBi. The radiation properties of the proposed antenna can be better understood by examining the E-Plane and H-Plane patterns, which represent the electric field and magnetic field vectors, respectively.

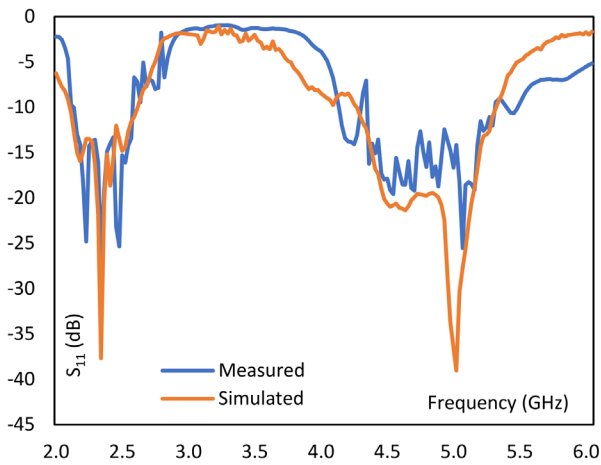


Figure 8: Simulated and Measured S_{11} vs Frequency

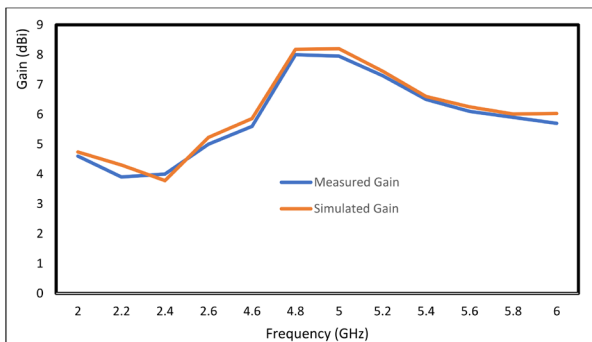


Figure 9: Gain vs Frequency of the proposed antenna

Figure 10 and Figure 11 showcase the 2D radiation patterns of the proposed antenna.

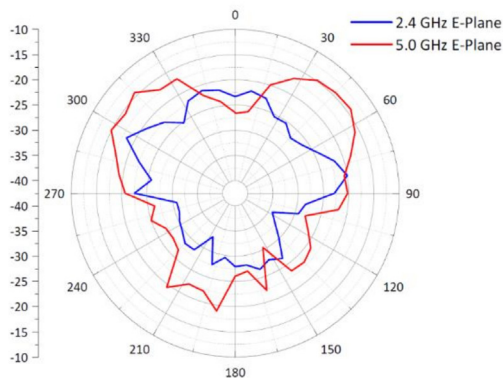


Figure 10: Measured E-Plane Pattern of the Proposed Antenna

The radiation patterns of the antenna demonstrate effective radiation. The absence of slots or defects in the solid ground ensures that there is no back propagation of the electric field. Figure 12 (a) and (b) illustrate the spatial representation of surface current distribution in the proposed antenna at frequencies of 2.4 GHz and 5.0 GHz, respectively. It is evident from this distribution that at higher frequencies, the currents are more

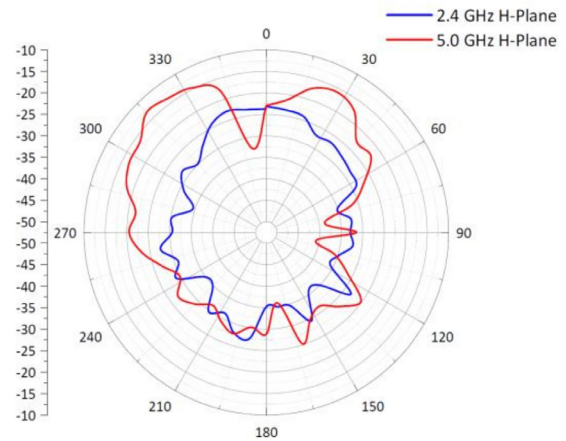


Figure 11: Measured H-Plane Radiation Pattern of the Proposed Antenna

dominant along the feedline and the lower horizontal element.

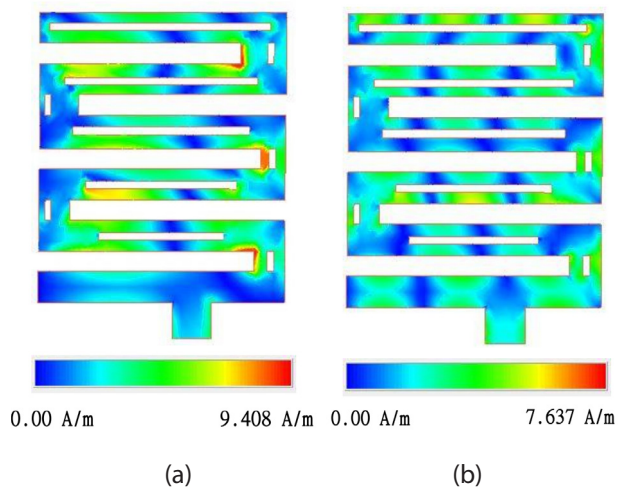


Figure 12: Spatial representation of the surface current distribution of the proposed antenna at (a) 2.4 GHz and (b) 5.0 GHz

3.2 Impedance matching network

The design and analysis of an impedance-matching network is discussed in this section. The incident power on the antenna is transferred to a rectifier circuit for RF-DC conversion. The efficiency of the overall system depends greatly on the extent of power transfer between the antenna and the rectifier circuit. To effect this requirement, different types of impedance matching networks are utilised [12-16]. Typically, L, pi, and T networks are used in these scenarios.

In this work, an impedance-matching network is designed with the aid of a smith chart available in the ADS environment. The S_{11} values of the designed antenna are plotted in the smith chart as shown in Figure 13. A smith chart serves as a graphical aid employed to

visualize and compute the characteristics of electrical impedance and reflection coefficients along a transmission line.

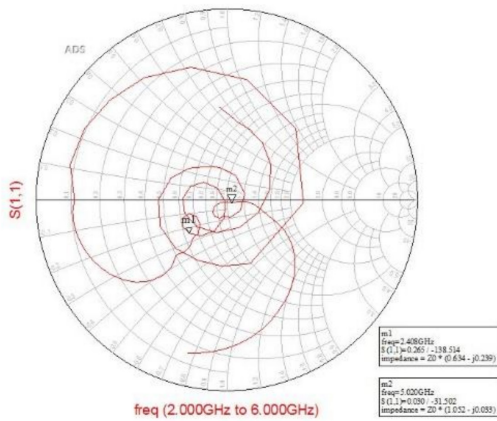


Figure 13: S11 Parameter plotted in the smith chart for the proposed antenna

From this plot, the impedance at the frequencies of interest is identified. The reference impedance is set to 50Ω. The designed impedance matching network for the proposed work is shown in Figure 14. Two inverted L-shaped L-C networks are connected to bring about the required matching characteristics.

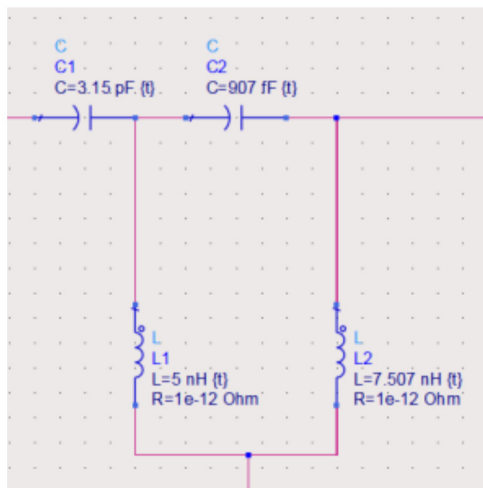


Figure 14: Impedance matching network for the proposed antenna

3.3 Multiband rectifier-voltage doubler

In this section, the design, simulation, and analysis of a rectifier-voltage doubler circuit are performed using the Keysight ADS software. The purpose of this circuit is to convert the RF signal captured by the proposed micropatch meanderline antenna into an equivalent DC output voltage. Figure 15 shows the circuit diagram of the overall multiband RF energy harvesting circuit.

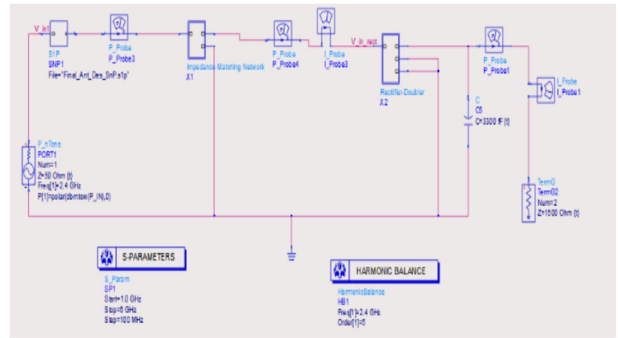


Figure 15: RF Energy Harvesting Circuit Used in ADS

The integration of impedance matching ascertains the transfer of maximum power from the antenna to the rectifier circuit. Also, the losses introduced by the two conventional diodes have been taken into consideration. To address this issue, these diodes were replaced by HSMS 2850 series Schottky diodes. The rectifier-doubler is fabricated on the same 1.6 mm thick FR4 based double sided copper sheet. This is shown in figure 16.

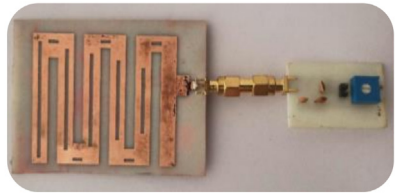


Figure 16: Proposed RF Energy Harvesting Circuit

The S11 vs frequency plot for an input power of 0 dBm is shown in Figure 17. In the simulation of the rectenna, a load resistance of 1 kΩ was utilised. The simulated results clearly show that the rectifier has been properly matched with the 50 Ω reference. The overall bandwidth of 2.1 GHz was obtained for the rectenna. Return loss values of -21.64 dB at 2.3 GHz and -21.93 dB at 5.6 GHz were observed in the simulated results.

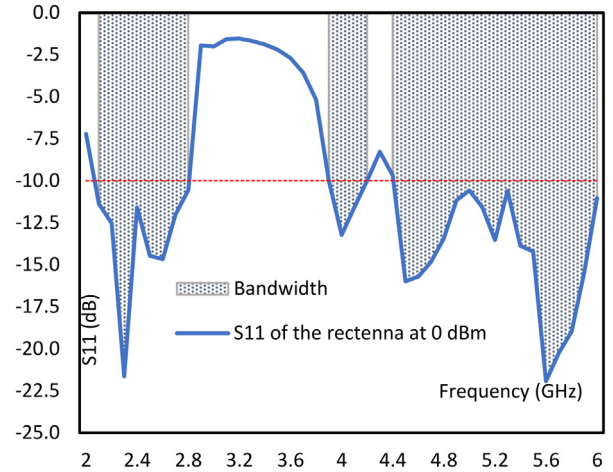


Figure 17: Reflection coefficient of rectenna at 0 dBm

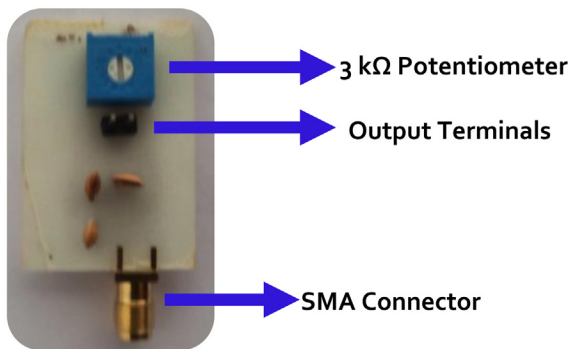
The antenna is connected to the rectifier through an impedance-matching network in the simulation, facilitated by the SnP file. The file provides return loss values across the frequency range intended for the antenna's operation.

The efficiency of RF to DC conversion process performed by the rectenna is estimated using the following equation [36].

$$Efficiency, \eta = \frac{V_L^2}{R_l \times P_R} \times 100 \tag{5}$$

where R_l - load resistance, V_L - output voltage, and P_R - input power.

The proposed rectenna is shown in figure 17. Figures 18 (a) and (b) depicts the front and back view of the fabricated rectifier multiplier circuit. The impedance matching network is effected using the distributed component technique. A rectangular microstripline of 3.08 mm x 3.56 mm is cascaded with the feedline of the antenna to bring the impedance to 50 ohms. A variable resistor is used at the load to check the performance of the rectenna at different load resistance values.



(a). Front View



(b). Back View

Figure 18: Front and Back View of the Rectifier-Multiplier Circuit

Variations in load resistance affect the efficiency of the rectenna. Therefore, the input power was varied from -5 dBm to 30 dBm, and the corresponding output voltage and efficiency were noted. The efficiency versus input power and the output voltage versus input power curves of the designed rectenna at different load resistances are depicted in Figure 19 and Figure 20 respectively. From the simulation result it was inferred that a peak efficiency of 84.38% was achieved at an input power level of 21 dBm. The experimental validation showed that a peak efficiency of 77.8 % was achieved at a power level of 27 dBm.

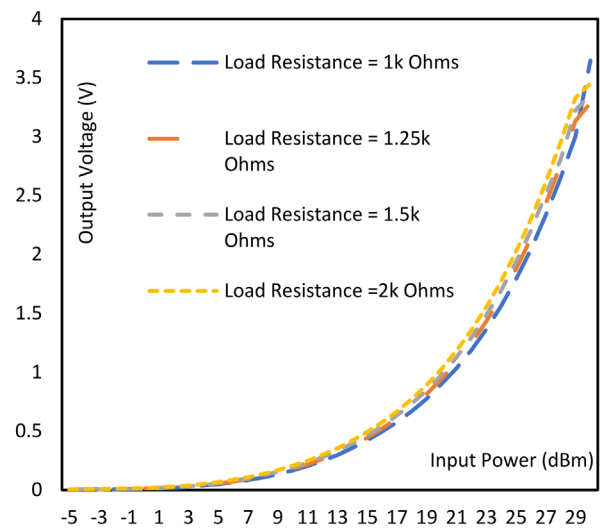


Figure 19: Input Power vs Efficiency for Different Load Resistances

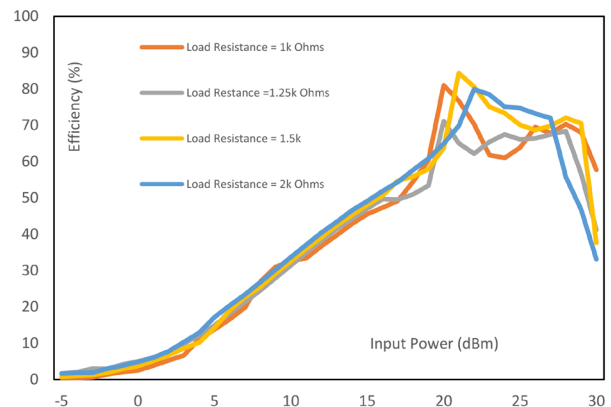


Figure 20: Output Voltage vs Input Power at Different Load Resistances

Based on the simulation results, the proposed rectenna demonstrated a minimum voltage of 2 mV at an input power of -5 dBm. Moreover, by utilizing a 1 kΩ load resistance and an input power of 30 dBm, a maximum output voltage of 3.65 V was achieved in the simulation. The experimental results exhibited that a peak output voltage of 2.84 V was achieved from the 2.4

GHz Band and an output voltage of 1.84 from the 5.0 GHz band. It is evident from the nature of the plot that the output voltage increases with an escalation in the input power and the efficiency initially increases and then decreases with an increase in the input power. This is plotted in figure 21 and 22 respectively. The efficiency dip occurs since the output voltage does not increase by a great factor with continuous increase in the input power level.

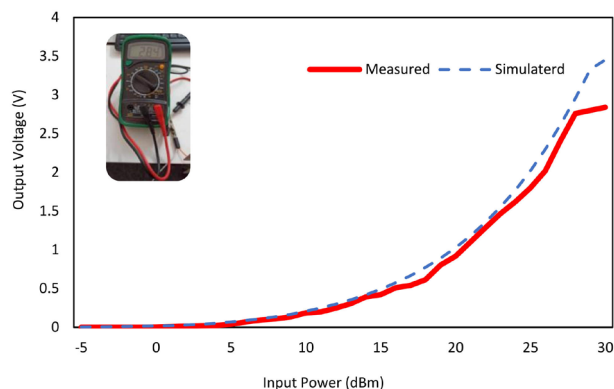


Figure 21: Input Power vs Output Voltage

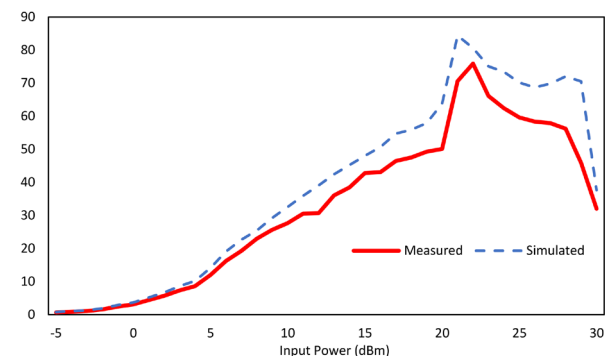


Figure 22: Input Power vs Efficiency

The proposed rectenna is compared with recent works available in the literature. The comparison is given in Table 3.

4 Conclusion

This work has successfully demonstrated the application of meanderline microstrip antennas for harvesting RF energy from wireless communication systems’ frequencies. The findings highlight the potential of meanderline structures in overcoming the limitations of conventional microstrip patch antennas and improving their performance in terms of bandwidth and power harvesting efficiency. By introducing slots in the meanderline structures of the antenna’s radiating patch, the overall performance of the antenna has been significantly enhanced. This improvement has led to an

Table 3: Comparison with recent works

Ref	Frequency Band	Gain (dBi)	Peak RF-DC Efficiency (%)	BW (GHz)	Peak Output Voltage (V)
[4]	Broadband	10	72.5	0.4	4.5
[10]	2.4 GHz and 5.8 GHz	3.83	67.62	--	2.62
[7]	2.4 GHz, 3.0 GHz and 5.8 GHz	9	70	0.8	1.9
[33]	2.45 GHz	3.78	77	0.3	1.1
[25]	Broadband	4.3	88.58	2.5	10.7
This Work	2.4 GHz, 5.0 GHz	8.65	84.4	1.2 GHz	3.65

expanded operating bandwidth of 1.1 GHz, which is crucial for capturing a wide range of electromagnetic energy sources.

Electromagnetic simulation results revealed that the proposed antenna design exhibits improved impedance matching, reduced return loss (-36.3 dB), and enhanced radiation characteristics (8.646 dBi gain) compared to conventional designs. The experimental results were in line with the simulation results. However, a slight reduction in the overall performance was observed. It is an indication of the losses encountered during the experimentation. Nonetheless, these results indicate the practical feasibility of using meanderline microstrip patch antennas to harvest RF energy from Wi-Fi and WLAN frequency bands. The improved performance and compactness of these antennas offer a promising solution for sustainable and self-powered wireless communication systems, thereby advancing energy harvesting technology.

5 Conflict of interest

The authors of this document does not have any Conflict of Interest (COI) in publishing this paper

6 References

1. W. A. Khan, R. Raad, F. Tubbal, and G. Mansour, "Design of a compact antenna and rectifier for a dual band rectenna operating at 2.4 GHz and 5.8 GHz," in *INT C TELECOMMUN SYS*, 2022, pp. 1-5: IEEE. <https://doi.org/10.1109/TSSA56819.2022.10063929>.

2. S.-E. Adami *et al.*, "A flexible 2.45-GHz power harvesting wristband with net system output from–24.3 dBm of RF power," *IEEE T MICROW THEORY* vol. 66, no. 1, pp. 380-395, 2017.
<https://doi.org/10.1109/TMTT.2017.2700299>.
3. N. M. Din, C. K. Chakrabarty, A. B. Ismail, K. K. A. Devi, and W.-Y. Chen, "Design of RF energy harvesting system for energizing low power devices," *PR ELECTROMAGN RES M*, vol. 132, pp. 49-69, 2012.
<https://doi.org/10.2528/PIER12072002>
4. M.-J. Nie, X.-X. Yang, G.-N. Tan, and B. Han, "A compact 2.45-GHz broadband rectenna using grounded coplanar waveguide," *IEEE antennas wireless propagation letters*, vol. 14, pp. 986-989, 2015.
<https://doi.org/10.1109/LAWP.2015.2388789>.
5. C. Song, Y. Huang, J. Zhou, J. Zhang, S. Yuan, and P. Carter, "A high-efficiency broadband rectenna for ambient wireless energy harvesting," *IEEE T ANTENN PROPAG LET*, vol. 63, no. 8, pp. 3486-3495, 2015.
<https://doi.org/10.1109/TAP.2015.2431719>.
6. H. Takhedmit, L. Cirio, S. Bellal, D. Delcroix, and O. Picon, "Compact and efficient 2.45 GHz circularly polarised shorted ring-slot rectenna," *ELECTRON LETT* vol. 48, no. 5, pp. 253-254, 2012.
<https://doi.org/10.1049/el.2011.3890>.
7. M. Aboualalaa, I. Mansour, and R. K. Pokharel, "Energy Harvesting Rectenna Using High-gain Triple-band Antenna for Powering Internet-of-Things (IoT) Devices in a Smart Office," *IEEE T INSTRUM MEAS* 2023.
<https://doi.org/10.1109/TIM.2023.3238050>.
8. S. Agrawal, M. S. Parihar, and P. N. Kondekar, "A dual-band rectenna using broadband DRA loaded with slot," *INT J MICROW WIREL T* vol. 10, no. 1, pp. 59-66, 2018.
<https://doi.org/10.1017/S1759078717001234>.
9. M. A. Al-Janabi and S. K. Kayhan, "Flexible vivaldi antenna based on a fractal design for RF-energy harvesting," *PR ELECTROMAGN RES M*, vol. 97, pp. 177-188, 2020.
<https://doi.org/10.2528/PIERM20073003>.
10. K. Bhatt, S. Kumar, P. Kumar, and C. C. Tripathi, "Highly efficient 2.4 and 5.8 GHz dual-band rectenna for energy harvesting applications," *IEEE T ANTENN PROPAG LET*, vol. 18, no. 12, pp. 2637-2641, 2019.
<https://doi.org/10.1109/LAWP.2019.2946911>.
11. Y. Chang, P. Zhang, and L. Wang, "Highly efficient differential rectenna for RF energy harvesting," *MICROW OPT TECHN LET* vol. 61, no. 12, pp. 2662-2668, 2019.
<https://doi.org/10.1002/mop.31945>.
12. M. C. Derbal and M. Nedil, "A high gain dual band rectenna for RF energy harvesting applications," *PR ELECTROMAGN RES Lett*, vol. 90, pp. 29-36, 2020.
<https://doi.org/10.2528/PIERL19122604>.
13. S. Divakaran and D. Krishna, "Dual-band multiport rectenna for RF energy harvesting," *PR ELECTROMAGN RES C* vol. 107, pp. 17-31, 2021.
<https://doi.org/10.2528/PIERC20100802>.
14. S. Chandravanshi and M. Akhtar, "An efficient dual-band rectenna using symmetrical rectifying circuit and slotted monopole antenna array," *INT J RF MICROW CE*, vol. 30, no. 4, p. e22117, 2020.
<https://doi.org/10.1002/mmce.22117>.
15. S. Chandravanshi, S. S. Sarma, and M. J. Akhtar, "Design of triple band differential rectenna for RF energy harvesting," *IEEE T ANTENN PROPAG LET*, vol. 66, no. 6, pp. 2716-2726, 2018.
<https://doi.org/10.1109/TAP.2018.2819699>.
16. D. Colaiuda, I. Ulisse, and G. Ferri, "Rectifiers' design and optimization for a dual-channel RF energy harvester," *J LOW POWER ELECTRON APPL* vol. 10, no. 2, p. 11, 2020.
<https://doi.org/10.3390/jlpea10020011>.
17. A. Karampatea and K. Siakavara, "Synthesis of rectenna for powering micro-watt sensors by harvesting ambient RF signals' power," *Electronics* vol. 8, no. 10, p. 1108, 2019.
<https://doi.org/10.3390/electronics8101108>.
18. N. Kashyap and D. Singh, "A Novel Circularly Polarized Annular Slotted Multiband Rectenna for Low Power Sensor Applications," *PR ELECTROMAGN RES B* vol. 99, pp. 103-119, 2023.
<https://doi.org/10.2528/PIERB22122606>.
19. H. H. Ibrahim, M. S. Singh, S. S. Al-Bawri, and M. T. Islam, "Synthesis, characterization and development of energy harvesting techniques incorporated with antennas: A review study," *Sensors*, vol. 20, no. 10, p. 2772, 2020.
<https://doi.org/10.3390/s20102772>.
20. S. Ullah, C. Ruan, M. S. Sadiq, T. U. Haq, A. K. Fahad, and W. He, "Super wide band, defected ground structure (DGS), and stepped meander line antenna for WLAN/ISM/WiMAX/UWB and other wireless communication applications," *Sensors*, vol. 20, no. 6, p. 1735, 2020.
<https://doi.org/10.3390/s20061735>.
21. S. Muhammad, J. J. Tiang, S. K. Wong, A. Smida, M. I. Waly, and A. Iqbal, "Efficient quad-band RF energy harvesting rectifier for wireless power communications," *INT J ELECTRON COMM* vol. 139, p. 153927, 2021.
<https://doi.org/10.1016/j.aeue.2021.153927>.
22. P. V. Naidu, A. Kumar, and R. Rajkumar, "Design, analysis and fabrication of compact dual band uniplanar meandered ACS fed antenna for 2.5/5 GHz applications," *MICROSYST TECHNOL* vol. 25, pp. 97-104, 2019.
<https://doi.org/10.1007/s00542-018-3937-8>.
23. A. Okba, A. Takacs, H. Aubert, S. Charlot, and P.-F. Calmon, "Multiband rectenna for microwave ap-

- plications," *C R PHYS* vol. 18, no. 2, pp. 107-117, 2017.
<https://doi.org/10.1016/j.crhy.2016.12.002>.
24. N. Othman, N. Samsuri, M. Rahim, K. Kamardin, and H. Majid, "Meander bowtie antenna for wearable application," *TELKOMNIKA* vol. 16, no. 4, pp. 1522-1526, 2018.
<https://doi.org/10.12928/telkomnika.v16i4.9061>.
 25. R. Pandey, A. K. Shankhwar, and A. Singh, "An improved conversion efficiency of 1.975 to 4.744 GHz rectenna for wireless sensor applications," *PR ELECTROMAGN RES C*, vol. 109, pp. 217-225, 2021.
<https://doi.org/10.2528/PIERC20121102>.
 26. Y. Shi, Y. Fan, Y. Li, L. Yang, and M. Wang, "An efficient broadband slotted rectenna for wireless power transfer at LTE band," *IEEE T ANTENN PROPAG*, vol. 67, no. 2, pp. 814-822, 2018.
<https://doi.org/10.1109/TAP.2018.2882632>.
 27. J. D. Kraus and R. J. Marhefka, *Antennas for all applications*, 2002. [Online]. Available.
 28. B. V. S. Suwan, W. W. G. Vidula, W. Wanniarachchi, C. H. Manathunga, and S. Jayawardhana, "The Design and Implementation of an RF Energy Harvesting System Using Dynamic Pi-Matching, Enabling Low-Power Device Activation and Energy Storage," *PR ELECTROMAGN RES C*, vol. 119, 2022.
<https://doi.org/10.2528/PIERC21121802>.
 29. D. Vital, S. Bhardwaj, and J. L. Volakis, "Textile-based large area RF-power harvesting system for wearable applications," *IEEE T ANTENN PROPAG*, vol. 68, no. 3, pp. 2323-2331, 2019.
<https://doi.org/10.1109/TAP.2019.2948521>.
 30. F. Zanon, U. Resende, G. Brandao, and I. Soares, "Energy Harvesting System Using Rectenna Applied to Wireless Powered Remote Temperature Sensing," *PR ELECTROMAGN RES C*, vol. 114, pp. 203-217, 2021.
<https://doi.org/10.2528/PIERC21060901>.
 31. K. Shafique *et al.*, "Energy harvesting using a low-cost rectenna for Internet of Things (IoT) applications," *IEEE access* vol. 6, pp. 30932-30941, 2018.
<https://doi.org/10.1109/ACCESS.2018.2834392>.
 32. H. H. R. Sherazi, D. Zorbas, and B. O'Flynn, "A comprehensive survey on RF energy harvesting: Applications and performance determinants," *Sensors* vol. 22, no. 8, p. 2990, 2022.
<https://doi.org/10.3390/s22082990>.
 33. K. Çelik and E. Kurt, "A novel meander line integrated E-shaped rectenna for energy harvesting applications," *INT J RF MICROW CE* vol. 29, no. 1, p. e21627, 2019.
<https://doi.org/10.1002/mmce.21627>.
 34. M. Koohestani, J. Tissier, and M. Latrach, "A miniaturized printed rectenna for wireless RF energy harvesting around 2.45 GHz," *INT J ELECTRON COMM* vol. 127, p. 153478, 2020.
 35. M. Mathur, A. Agrawal, G. Singh, and S. K. J. P. I. E. R. M. Bhatnagar, "A compact coplanar waveguide fed wideband monopole antenna for RF energy harvesting applications," *PR ELECTROMAGN RES M* vol. 63, pp. 175-184, 2018.
<https://doi.org/10.2528/PIERM17101201>.
 36. R. Pandey, A. K. Shankhwar, and A. Singh, "An improved conversion efficiency of 1.975 to 4.744 GHz rectenna for wireless sensor applications," *Progress In Electromagnetics Research C* vol. 109, pp. 217-225, 2021.



Copyright © 2024 by the Authors. This is an open access article distributed under the Creative Commons Attribution (CC BY) License (<https://creativecommons.org/licenses/by/4.0/>), which permits unrestricted use, distribution, and reproduction in any medium, provided the original work is properly cited.

Arrived: 07. 08. 2023

Accepted: 22. 04. 2024

Optimization of Mobile Ad-hoc Networks Communication Using Ad-hoc On-demand Multipath Distance Vector With Novel Aging Multi Population Strategy for Effectual Energy Utilization

Janani Ramasamy Selvaraj¹, Asokan Ramasamy²

¹*Department of Electronics and Communication Engineering, Kongunadu College of Engineering and Technology, Trichy, India*

²*Department of Electronics and Communication Engineering, Kongunadu College of Engineering and Technology, Thottiam, Trichy, India*

Abstract: In today's world, wireless technologies play a vital role in numerous real-world applications, particularly Mobile Ad-hoc Networks (MANETs), which offer bidirectional transmission capabilities through intermediary nodes. However, packet collision poses a significant challenge in MANETs due to the random movement of nodes at unpredictable speeds, leading to degraded throughput, increased routing overhead, and higher end-to-end delays. Moreover, frequent node mobility causes topological shifts and link instability, further lowering data delivery rates. Limited possible routes to the destination network also contribute to traffic congestion at intermediary nodes, hindering successful packet delivery, especially in real-world MANET applications. The proposed approach introduces a novel strategy utilizing the concept of "age" to evaluate each particle's local area search capacity within the MANET environment, termed Aging Multi Population Optimization (AMPO). Particles are categorized into distinct age groups based on their ages to maintain population diversity during the search process. Particles within each age group can only select younger particles or those within their own clusters/groups as preferred neighbors. To determine the optimal route to the destination, multiple pathways returned by the Adhoc On-demand Multipath Distance Vector (AOMDV) mechanism are optimized, considering the route with the highest fitness value as the most ideal. Additionally, a parameter setting mechanism based on age groups is introduced to accelerate convergence, where particles in different age groups possess distinct parameters. Finally, the proposed approach is evaluated against existing methods such as AOMDV-TA and EHO-AOMDV, considering network overhead, throughput, delay, energy usage, and packet delivery range as crucial performance metrics.

Keywords: Fitness range, aging population, MANETs, AOMDV, optimization.

Optimizacija komunikacije v mobilnih omrežjih Ad-hoc z uporabo vektorja razdalje na zahtevo z novo strategijo staranja večje populacije za učinkovito rabo energije

Izveček: V današnjem svetu imajo brezžične tehnologije ključno vlogo v številnih aplikacijah v resničnem svetu, zlasti v mobilnih omrežjih ad hoc (MANET), ki omogočajo dvosmerni prenos preko vmesnih vozlišč. Trk paketov v omrežjih MANET je velik izziv zaradi naključnega gibanja vozlišč z nepredvidljivo hitrostjo, kar vodi do zmanjšanja prepustnosti, povečanja odvečnega usmerjanja in večjih zamud med koncema. Poleg tega pogosta mobilnost vozlišč povzroča topološke spremembe in nestabilnost povezav, kar še

How to cite:

J. R. Selvaraj et al., "Optimization of Mobile Ad-hoc Networks Communication Using Ad-hoc On-demand Multipath Distance Vector With Novel Aging Multi Population Strategy for Effectual Energy Utilization", Inf. Midem-J. Microelectron. Electron. Compon. Mater., Vol. 54, No. 2(2024), pp. 107–122

dodatno zmanjšuje hitrost dostave podatkov. Omejene možne poti do ciljnega omrežja prispevajo tudi k zastojem prometa v vmesnih vozliščih, kar ovira uspešno dostavo paketov, zlasti v resničnih aplikacijah MANET. Predlagani pristop uvaja novo strategijo, ki uporablja koncept „starosti“ za ocenjevanje zmogljivosti iskanja vsakega delca na lokalnem območju v okolju MANET, imenovano Aging Multi Population Optimization (AMPO). Delci so razvrščeni v različne starostne skupine na podlagi njihove starosti, da se med postopkom iskanja ohrani raznolikost populacije. Delci v vsaki starostni skupini lahko kot prednostne sosede izberejo le mlajše delce ali delce znotraj svojih grozdov/skupin. Za določitev optimalne poti do cilja se optimizira več poti, ki jih vrne mehanizem AOMDV (Adhoc On-demand Multipath Distance Vector), pri čemer se kot najbolj idealna upošteva pot z najvišjo vrednostjo sposobnosti. Poleg tega se za pospešitev konvergence uvede mehanizem za določanje parametrov na podlagi starostnih skupin, pri čemer imajo delci v različnih starostnih skupinah različne parametre. Nazadnje je predlagani pristop ocenjen v primerjavi z obstoječimi metodami, kot sta AOMDV in EHO-AOMDV, pri čemer se kot ključni kazalniki uspešnosti upoštevajo odvečno usmerjanje, prepustnost, zamuda, poraba energije in doseg dostave paketov.

Ključne besede: sposobnost, staranje populacije, MANET-i, AOMDV, optimizacija.

*Corresponding Author's e-mail: spjs92@gmail.com

1 Introduction

Mobile Ad-hoc Network (MANET) comprised of self-configuring wireless nodes. The Fig. 1 shows the mobility of networks, indicating the movement of data within the network rather than the networks themselves. Each Mobile ad-hoc device has a router that knows the necessary network activity and can forward messages reliably. The gadget can operate on its own or join a massive group. This feature has improved Mobile ad-hoc use [1]. The absence of centralized management in mobile wireless ad hoc networks causes several issues [2]. Because of mobile nodes, routing techniques respond to dynamic routing, increasing network congestion control [3]. Maintaining effective networking and Quality of services (QoS) while taking appropriate broadband and power restrictions into account are still challenging. Hierarchical structures scale effectively because Mobile nodes have many mobile nodes [4]. Building node hierarchies enables network structure, which may solve Routing protocol challenges. Mobile ad hoc networks have a well-established technique called grouping [5]. Numerous proposed algorithms take into consideration different measures and focus on different objectives. The bulk of existing techniques, however, are unable to produce stable cluster structures. They are crucially dependent on the continuous delivery of control messages, which raises internet usage and demands more power from Multi-Homing (MH). Spending extra money or time on ad-hoc networks is unnecessary. In a Mobile Ad-hoc Network, every network device serves as both the network and a typical host. Mobile node rechargeable batteries, periodic network connectivity, and bandwidth limitations imposed on node mobility are still problems for Mobile Ad-hoc Network [6,7]. Numerous clustering algorithms have been proposed to handle complex and dynamic environments [8,9]. For one-hop, multi-hop, and self-organizing networking, many routing techniques have

been created [10,11]. Three sorts of routing exist: reactive, proactively, and mixed. Even when no content is sent, proactively protocols maintain the networks working and route knowledge available.

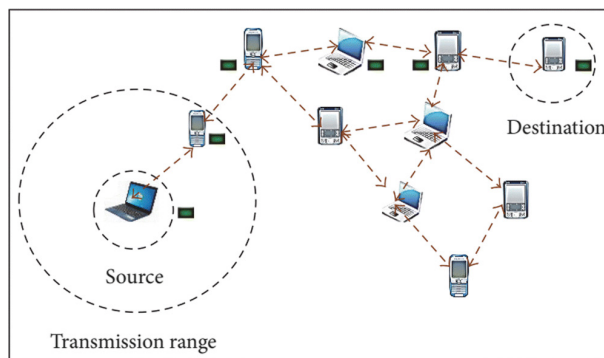


Figure 1: Basic Mobile Ad-hoc Network topology

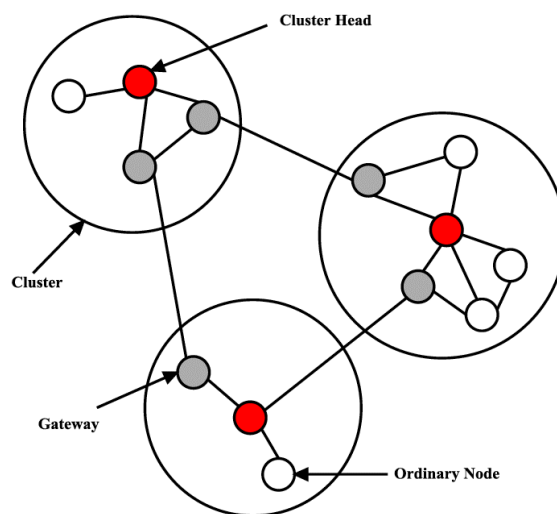


Figure 2: Clustering in MANET

The clustering technique is the most often used tactic in Mobile Ad-hoc Network, although figuring out what it needs and how successful it is still difficult [12].

The standard clustering algorithm in Mobile Ad-hoc Network is shown in Fig. 2. A CHs represents each sub-structure throughout the classification stage, while a gateway node mediates inter-cluster connectivity. The groups that have survived are regular nodes. A cluster's borders are determined by its transmission zone or Cluster Head (CH). Cluster-based forwarded networks are abnormal nodes. The proposed work has suggested a clusters coordinator-based Cluster head election mechanism.

Nodes in Mobile Ad-hoc Network are unaware of the structure of their networks and must determine it on their own because an ad hoc network's topology is changeable. The fundamental rules say that whenever a new node enters an ad hoc network, it must broadcast an indication of its existence as well as pay more attention to broadcasting of a similar nature received from mobile nodes already in the network. The proposed research takes into account the Adhoc On-demand Multipath Distance Vector routing mechanism, which is utilised to find numerous routes from the origin to the destination, in this regard. In this work, a brand-new fitness function is proposed as an optimization method. Adhoc On-demand Multipath Distance Vector (AOMDV) and Aging Multi Population Optimization (AMPO) combined, based on Fuzzy Logic – based Fairness (FF). For FF, the most important metrics to consider while choosing the most reliable and efficient route from origin to destination are data packet collision, queue length, and connection stability. Thus, the following are the primary contributions of this paper:

- The innovative aspect of Aging Multi Population Optimization (AMPO) lies in its utilization of age-based grouping to guide the selection of preferred neighbors, allowing particles to consider only younger particles or those within their own clusters/groups. This approach facilitates more efficient routing decisions by leveraging the knowledge accumulated over time within the network.
- Using the parameters alteration in the age-group based topological structure, the particle of the ageing multi population approach converges at the local optimal threshold.
- Before to data transmission, all detected paths will be meticulously sorted, with the data load being distributed across the paths depending on path energy relative to all paths' capacity.

This research article is arranged in the following manner. Section 2 deliberates related works. Section 3 goes through the Aging Multi Population Optimization optimization algorithm in depth, as well as the proposed Aging Multi Population Optimization with Adhoc On-demand Multipath Distance Vector. The experimental procedure and performance assessment are presented

in Section 4. Finally, Section 5 summarises the key conclusions and discusses potential future study.

2 Related works

Adhoc On-demand Multipath Distance Vector (AOMDV) is a flexible multi-path routing Protocol that allows mobile edge computation. When a network received a request to transmit, then it first evaluates the fact that the route listing contains a route to the network it intends to communicate with. If no route exists, a route inquiry is issued. The least hop count determines the optimum route when there are several possibilities. Trust-Aware Adhoc On-demand Multipath Distance Vector (TA-AOMDV), which was proposed by researchers in [13], aims to lessen data traffic. This protocol would suffer in dynamic configurations when route safety and network diversity are required. In general, this strategy hardly boosts performance compared to alternative approaches, which often outperform it.

[14] proposed the energy-efficient, shortest path algorithm Fuzzy logic – based Fairness Adhoc On-demand Multipath Distance Vector (FF-AOMDV). In the case of a network outage or crash, AOMDV will automatically change to the next shortest distance in the route cache. FF-AOMDV performance is lower than AOMDV since it only considers energy and the shortest distance, thus network lifespan enhancement is limited. AOMDV directional conventions and the bio-enhanced computation known as Elephant Herding Optimization (EHO) were used to build an energy-efficient steering convention in their article [15]. The inventors' work streamlines hub energy use by dividing them into two kinds. A way from the test hub class with sufficient transmission energy might be selected, reducing the likelihood of routing disappointments and the growing number of disconnected hubs as a consequence of increased information retrieval. Following each transmission cycle, the EHO updating administration adjusts classes by an isolating administration that assesses hubs depending on the energy residual. The results obtained by the author demonstrate that EHO outcomes are preferable to those obtained by other techniques. As a result of the node's clan needing to be updated often, which drives up routing costs and introduces delay, there is, nevertheless, a significant amount of delays and communication expenses.

By switching to a different route when the primary one is stopped and allowing information to progress, the AOMDVs [16] networking strategy may provide a minimum QoS guarantee. But moving to other pathways results in a larger networking overhead since maintaining the path would need more data. [17] designed the

QoS-AOMDV routing protocol to increase QoS. This technique gathers cross-layer statistics on remaining energy and queuing length to choose high-quality paths. The packet transmission ratio is low due to information collisions, which increases the latency. [18] suggests a MANET routing scheme. Migration causes random data stream loss & connectivity failures. The authors proposed an efficiency function that accounts for traffic volume, range among the source and destination nodes, and sustainable energy. Efficiency avoids crowded channels. AOMDV uses the efficiency function to choose the best routes. The number of data transmissions even if a networking connection is sometimes dropped, the quantity of energy used, and a short path length are a few elements to consider while selecting the best fitness approach. The dependability of the routes, as measured by the rate of information conflict and connection stability, was not taken into account by this technique. A multipath relay node based on link reliability is suggested by the approach in [19]. The simulation model and the size of the forwarding queue are used by the algorithm to estimate the confidence in the ability probabilities. This raises the likelihood that the relationship will remain stable. However, the power consumption of the network is significant since regular route modifications need additional nodes to ensure network stability.

AOMDV provide a congestion management method [20]. The technique uses a rate-based wireless data system with queue-based congestion management to progress the effectiveness of the system. The results showed better delivery of packets and less communication overhead. However, the system's utilization is relatively low because of the high network congestion brought on by collisions. One of the most significant difficulties with MANET is traffic congestion and connection breakdown. The network should have as little end-to-end latency as possible while delivering data packets from one place to another. But if there is overcrowding on the source nodes, it will be difficult to accomplish this because it will lengthen the queue, which will add to the delay. Consequently, [21] suggested a M-ary Quadrature Amplitude Modulation (MQAM) routing approach based on the Multi-Criteria Decision Making (MCDM) metric. Results reveal that MQAM routing is improved than Multi Protocol- Optimized Link State Routing Protocol (MP-OLSR) throughput. However, because of transmission errors, the delay is relatively high. [22] introduced an original communication protocol Congestion-Aware Clusters & Forwarding to ease congestion and cluster in Wireless Sensor Network (WSN).

It was claimed in [23] that Transmission control Protocol (TCP) transmission over Time Division Multiple

Access (TDMA) based MANETs might be utilized without interference with sender-side network congestion and prototype resource predictions. While together algorithms provide efficient congestion reduction networking techniques, they neglected to account for stochastic transmission errors, which would have unnecessarily reduced the traffic load. Wireless bandwidth transmission across mobile nodes must be managed and dispersed since MANETs lack a central organizer. MANET typically use Carrier sense multiple access/collision avoidance (CSMA/CA) and its alternatives. All of these Carrier sense multiple access collision (CSMAC) methods are, however, affected by the "secret terminal" problem [24]. Compared to standard communication networks, ad-hoc networks are more difficult. In [25], researchers advocated replacing hop count with link efficiency and impact frequency. This technique makes use of the single-path, antiquated interface AODV. The routing identification procedure must be started in the event of a connection loss, which will increase delay and routing expense.

In [26], a hybrid Genetic Algorithm -Hill Climb approach is employed in the (GAHC)route. A projected hybridization technique interpolates CHs and aggregating pathway attributes including throughput, latency, and node interconnectedness are utilized to pick routes. This suggested approach provides the highest bandwidth, detection accuracy, and ratio of packets delivered with the least amount of energy and latency. However, this approach is predicated on nodes with slow mobility. Authors in [27] investigated the route efficiency of the algorithm for WSNs. Two key experiment instances used Djekstra and a genetic algorithm. Depending on OLSR, [28] proposed an Artificial Immune System - Optimized Link State Routing Protocol (AIS-OLSR) approach that chooses the best path depending on base stations, node-accepting fuel qualities, and repository node proximity. This strategy could increase the network's capacity and end-to-end latency effectiveness. The significant amount of energy that must be used to calculate routes is one of the key concerns raised by this protocol.

A multipath high-quality of SR-MQMRs, according to [29], is reliable for the mobile ad-hoc network. This technique uses node signal power to pick the most reliable connections while considering throughput. The SR-MQMR protocol uses fewer specific times than MQMR, which boosts success. Additionally, choosing steady routes significantly increased dependability. The sudden change in system architecture and node stochastic velocities, however, have an impact on the network signal quality and reduce system performance by reducing the Packet delivery ratio (PDR).

When mobile networks are stationed at a steady speed and adopt a random path, the research [30] introduces novel Local Congestion Mitigation (LCM) and Personal digital Assistant (PDA) methodologies to evaluate the route dependability. Link expiration time, angular speed, connection, and reliability affect the LCM procedures of adjacent nodes, depending on the method provided. Both analytical and simulation findings that correctly forecast route integrity under dynamic topology, improving global network connection, demonstrate the LCM with the PDA approach's usefulness. The length of the connection expiration time generates additional latency, whereas a shorter duration increases routing overhead in the network.

Locating MANET adjacent nodes is the main goal of [31], which focuses on building multipath routing in varied mobility patterns. It efficiently manages congestion, data dissemination, and packet sequencing. The paper explains stable node forecasting, security evaluation, route finding, and package distribution. The optimum route is determined by linking stable connections between both the destinations and the source. A failed routing relationship activates path recovery. As a consequence, data packets are automatically dispersed along several paths. This approach has a very poor optimization performance owing to erroneous convergence, as revealed by an experimental investigation. Additionally, because each data packet is transmitted across numerous paths concurrently and only one of these channels is necessary, each node consumes a significant amount of energy.

2.1 Research gaps identified from the literature review

The following are some of the limitations that have been found, all of which will be addressed with greater depth in the subsequent research.

- An organised topology is inadequate for dealing with massive MANET systems.
- An ineffective monitoring system causes excessive network disruptions as well as failure of device.
- Existing approaches are ineffective when dealing with fluctuating topology.
- MANETs are consuming high bandwidth and energy.
- The lack of an effective procedure/protocol has a serious affect on PDR.

The proposed model overcomes the existing limitations with the concept of "age" in AMPO helps maintain population diversity, enabling more effective routing decisions in large-scale MANET systems. By categorizing particles into distinct age groups, the proposed approach ensures better adaptability to the dynamic and

expansive nature of MANET. The novel routing strategy introduced by AMPO, coupled with the parameter setting mechanism based on age groups, enhances packet delivery rates by optimizing route selection and accelerating convergence. This leads to more reliable and efficient packet delivery within the MANET environment.

Overall, the proposed approach addresses key limitations of MANET by introducing innovative routing strategies based on age-based optimization, thereby improving network performance, reliability, and efficiency. Through comprehensive evaluations against existing methods, the proposed approach demonstrates significant advancements in overcoming the challenges associated with MANET, paving the way for more robust and scalable wireless communication systems.

3 Proposed taxonomy: AOMDV with aging multi population optimization

AOMDV is a multihop protocol designed for network routing that supports MANET and is accessible on demand. Current research offers a system that uses a AMPO strategy to optimise routes in order to bypass unstable links as well as linkages that have traffic difficulties (such as linkages that are overcrowded or links with a higher collisions frequency). Several tribes of populations with younger men live under a head, whereas adult males prefer to keep apart but communicate through low-frequency influences. To imitate mature male populations leaving their tribes and to boost population diversification later on, two factors are employed. Population activity within tribes is tracked and updated using this method. The AMPO is divided into four stages:

- Stage 1) The clan-based split of the aging population
- Stage 2) The eldest male and eldest female for each clan are the matriarchs.
- Stage 3) The attitude of populations in herds may be modified according to the input of two operators Clan upgrading operator for adjusting the matriarch's location based on data from all clan populations.
- Stage 4) Based on the separation operator determined to use the upper and the lower limit of the location of the populations, the young males depart the clan. The departing adults may still communicate with the household female through minimum -frequencies vibes.

From the above, the explanation is that AMPO optimization addresses the problem of MANET network ener-

gy consumption. The MANET aging population, is separated into two clans, maybe with all interconnections. The division processes, based on nodal radiation, will establish each node's class, while the updates regulatory, that signal networks' reserves, will be changed for every transmission and is discussed in the next section.

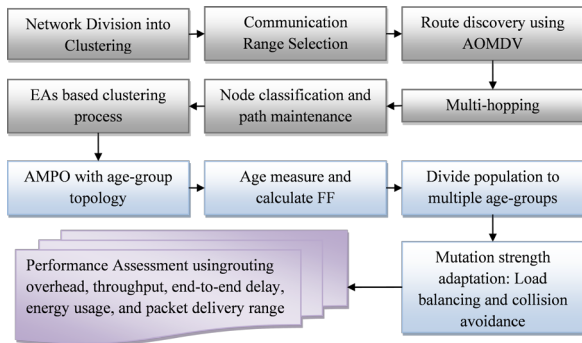


Figure 3: Working flow of the AOMDV-AMPO strategy

3.1 Routing protocol using AMPO-AOMDV

AMPO-AOMDV, a spread spectrum load-balancing communication system based on both AMPO& AOMDV, serves as the basis for this system. By splitting node communities into two tribes based on nodal energy, also known as the division operation, AMPO is employed largely to minimize node electricity usage. Nodes that have more energy than is required to transport all of the messages via the network will be assigned to the clan, whereas the rest will be assigned to the second clan. The AOMDV protocol discovers T multilink disjoint pathways by Broadcasting Route Request Packet(RREQ) signals from origin node S to target D, creating numerous reverse paths at the relay node and the endpoint. Similar Source IP addresses and ID duplication output RREQs replace RREQs with lower central transmission power and higher usage. The pathway between S to D will be arranged by nodal efficiency.

According to the proportion of route energy compared to the total energy of all identified pathways, the data burden is distributed across the T-detected paths. If all paths fail or there is an upgrade in any part from the initial clan all access points in both the 2nd clan members would be inspected, and also the clans will indeed be revised by swapping clusters. We may break down the AMPO-AOMDVs into its four primary phases network classification, Paths Identification, Information Bandwidth Allocation, and Paths Maintenance—to provide more specifics.

Network Classifier: As noted earlier, the AMPO is identifying the endpoints based on the show's maximum alive nodes, which are employed as the automated update controllers, to decrease the number of extremi-

ties in use. Endpoints that have more minimum energy than is required to transmit all incoming packets PTE_{n_i} across the ground station n_i will be classified as belonging to the first clan; alternatively, they will be placed in the second clan.

Algorithm 1: Classifying the network

```

    For i=1 to M (total nodes in network) do
       $PTE_{n_i} = TP * \beta(n_i, n_{i+1}) //$  separation operator
    If  $E_{n_i} > PTE_{n_i}$  Then  $n_i \in C_1$  Else C
    End If
  End For
  
```

Algorithm 1 shows the pseudo-code of C1& C2clan nodes, where TPs is the total no. of frames, indicates the effort consumption in transmitter & receiver packages views in one hop, then PTE_{n_i} is the strength desirable to carry all incoming packets over the single router. This stage reduces dead networks by ensuring that only networks with enough energy to broadcast will send.

Discovery of Path: The discontinuous trails investigation (shown in Figure 3) starts after categorizing the endpoints. This is accomplished by transferring RREQs from the S to D utilizing the AOMDV protocol. To retain the RREQ with both the maximum network original force and the smallest hops, repetitive RREQs using the same source and Identity will be evaluated. It will ensure that the fastest pathway with the greatest quantity of energy was found for transferring the whole collected data.

Maintenance of Path: If all routes fail (Eq 4) or any detected paths lose energy, resume the nodes categorization process. The update operators evaluate all network connections in the two tribes to move the dead locations. The terminals had rotating inertia and initially had insufficient fuel for communications, but they assumed power and were able to communicate from the 1st clan to the next and it start the routes for a path.

Data load balances: The T-found pathways are ranked in decreasing order by their maximum nodal remaining energy Pet , determined from the minimum remaining power of all X vertices on a way.

Path: Approach on the path power % concerning all found path energies, as specified in algorithm.

The nodes in green in Fig 9 represent those that were classified into Category 1 because their remaining energy was larger than the energy required to transport all packets over a single hop, while the remaining

nodes were classified into Category 2. RREQs are exclusively sent among nodes in clan C1—all nodes excluding node J, which has no predecessors in clan C1—as stated in portion (c) of the clarification. Only two identified pathways, t1D[S-A-B-G-D] and t2D[S-C-F-H-D] are shown in portion (d), and they will be arranged in decreasing order of nodal residual energy. Finally, the amount of information carried by every route will be calculated based on its frequency percentage concerning the combined power of all paths. For example, if there are 100 packages, 60 will be transmitted on t1 and 40 on t2.

Algorithm 2: Procedure for finding the routes

```

For j = 1 to R (for all nodes in Clan Cj) do
Flood RREQs from source S to destination D
Establishing numerous reversal routes at destination
and intermediate nodes
Using the source and intermediate nodes as nodes,
traverse the reverse paths back via several Route Reply
(RREP) to build multiple forwards paths to the target
Maintain RREQs with the lowest hop count and highest
nodal remaining energy
End For
    
```

3.2 Age-based evolutionary algorithms (EAs)

There are three aging operators, based on the techniques employed to calculate age: evolution age, static pure age, & genomic age. In evolutionary age, crossing or mutations children are given age 0, and each surviving individual's age increases by one per cycle. In static simple aging, a newborn's lifetime is 0 if its fitness is higher than its parents', or its relatives' ages. Unlike static pure aging, genetic variability overaged assigns generation 0 to offspring who have the same objective function value and differing coordination position than their parents. For a minimization issue, the three aging processors determine duration as in the following lemmas:

- Lemma 1: (evolutionary age). y age = 0.
- Lemma2: (static pure age). If $f(y) < f(x)$ then y age = 0 else y age = x age.
- Lemma 3: (genotypic age). if $f(y) \leq f(x)$ $\wedge y \neq x$ f(y) then y age = 0 else y age = x age.

When a person's age is detected, the aging operation is utilized to replace any person whose age exceeds the maximum age with a brand-new, randomly generated person. whereas adaptive aging may optimize functioning with plateaus. This is thus because a person's fitness stagnation causes their static pure age to increase without affecting their evolving age. Genotypic aging recognizes optimum solution and peak because it enables random stroll on the level. [32] describes age

as the population's genetic evolution. Depending on this age measurement, an Application Layer Protocol for Subnetworks (ALPS) is suggested to limit large inter-individual competition and procreation. Age 1 plus the oldest possible parent's age is the starting point for individuals produced via mutation or crossover. In ALPS, the majority are divided into multiple agelayers according to their ages, and each member may cross across with just another member of that layer or the one before it.

3.2.1 EAs-based clustering

A collection of M unidentified objects in the d i/pgap is represented by $\mathbf{O} = \{\mathbf{o}_1, \mathbf{o}_2, \dots, \mathbf{o}_n\}$. The j^{th} real-value characteristic of the i^{th} object ($i=1,2, \dots, n$) is represented by each member of the vector \mathbf{o}_{ij} ($\mathbf{o}_{ij}=1,2, \dots, d$). When faced with such a collection, a region-based segmentation clustering algorithm must choose a separation $C = \{C_1, C_2, \dots, C_k \mid \forall k: C_k \neq \emptyset$ such that the similarity of the items within the same clusters is maximized while the items within separate clusters are as dissimilar as feasible. The relationship among any two objects, \mathbf{o}_i and \mathbf{o}_j is described as follows in the most widely used correlation-based technique known as Euclidean distance:

$$D(\mathbf{o}_i, \mathbf{o}_j) = \sqrt{\sum_{m=1}^d (\mathbf{o}_{i,m} - \mathbf{o}_{j,m})^2} = \mathbf{x}_i - \mathbf{x}_j \quad (1)$$

This statistical method defines the cluster analysis issue mathematically [33]:

$$\text{Min} \sum_{k=1}^K \sum_{i=1}^n w_{ik} D(\mathbf{o}_i, \mathbf{z}_k) \quad (2)$$

where $\sum_{i=1}^n w_{ik} = 1$ for $i=1, \dots, n$ and \mathbf{z}_k be the center vertex C_k kth node. The Euclidean distance $C_k D(\mathbf{o}_i, \mathbf{z}_k)$ between an object's center and the kth cluster's (C_k) center is shown. Even $K=2$ is NP-hard [34]. The traditional K-means method and its various variations were regularly shown to be susceptible to being caught in a local optimum.

EAs were introduced to clustering because of K-means' local optima difficulty. An early use of EA for clustering produced cluster centroids using an evolution method [35], which were subsequently partitioned as in standard K-means algorithms. Although a genetic algorithm rather than an evolution technique has been used to evolve cluster centroids, this approach has continued to be refined. Ant colony optimization, different evolution, artificial bee colony, and particle swarm optimization are recent examples of population-based global optimization approaches that have been employed for clustering. Some studies develop cluster

centroids and find the ideal number of groups. The EAs increase the likelihood that the clustering algorithms will converge to an optimum solution, albeit at the sacrifice of convergence rate. Local search techniques, such as the K-means algorithm, were often used with EAs to refine the solutions found by EAs and speed up convergence to provide a thorough analysis of the EA-based clustering methods.

3.3 PSO with age-group approach

Particle Swarm Optimization Age Group (PSOAG) improves Particle Swarm Optimization (PSO) in situations with multiple local optimums. It is planned to add three additional features. First, a particular age description for PSO is suggested to determine how old each particle in the swarm is. Additionally, a topological architecture for age groups depending on this new metric is created to control swarm variety. The variable adaptation approach adjusts inertial weight, acceleration parameters, and mutation intensity periodically.

3.3.1 Measure of Age

The pbest location of a particle has not changed till predicting the optimal exploration.

The following describes the new age.

Indication 4: if $f(\mathbf{x}_i) < f(\mathbf{p}_i)$ then \mathbf{x}_i , age = 0 else \mathbf{x}_i , age = \mathbf{x}_i , age + 1.

Each randomly generated particle in the first basic aspect is off at age 0, if it is unable to locate a position that is superior to the current pbest, its age is increased by one in one iteration. Additionally, a difference like a mutation does not change the particle's age. If a particle's lifespan surpasses the preset maximum age, it is eliminated from the existing population as well as a new element is produced at random in the state space.

Particle age is calculated using the quantum state pbest origin and present situation. PSO does not modify particle positioning if it overlaps with a local solution. However, if it oscillates about a locally optimal, its real location likewise oscillates while the pbest position is held constant. Here, we refer to the two circumstances as fitness fluctuation and immobility. The pbest data may be utilized to identify the two phenomena since it stays constant in each of them. Because only performance in the current and preceding iterations is taken into account for calculating time. Therefore, the age of every particle is determined using the pbest position. If the particle's pbest location is not altered during the new age test, the particle's age will increase by one with each iteration if the position is not changed. This growth procedure goes on until the component finds

a more suitable pbest site or exceeds its maximum age and gets picked up.

3.3.2 Age-group topology structure

The people are divided into age groups to effectively use data from particles of various ages. Particles may be mapped to various age groups using a variety of mapping techniques, including Fibonacci, logarithmic, and polynomials processes. For example, using a mathematical equation, the age requirement within every age group is 1, 2, 4, 9,16, & the equivalent age limit is 1, 2,3 4,5 9,10 16, Age groups are shown in broad strokes in Fig. 1.

We define age-group topology from the age-grouped swarm. A random architecture is applied in the proposed circuit to determine neighbors for each particle. Instead of selecting k neighborhoods from the whole community, choose the neighbors from its groups together with the other older ensembles. The youngest group's nanoparticles are limited to choosing neighborhoods solely within their groupings. If age-group g_i and g_{i-1} have fewer nanoparticles than k, the current gbest component will be its only neighbor. Nevertheless, if the number is not lower than $k < 1$, k neighbors are randomly picked among them, and the element with a superior pbest placement is chosen as its best part of town for the current implementation.

3.4 Adaptation of parameter: x & ci adaptation

Acceleration constants c_1 and c_2 , which are utilized to maintain a balance between exploiting and exploring

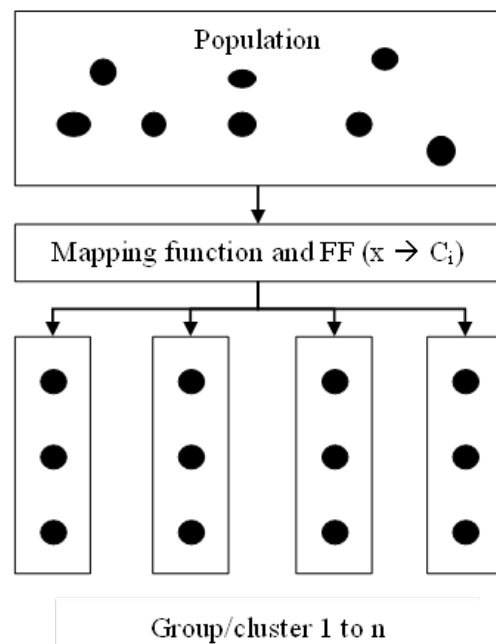


Figure 4: Segregating populations into several age groups via mapping functions. (The terms “x and ci” is particle age and target node)

in the query, have a substantial impact on PSO's performance. PSOAG automatically adjusts the three parameters for each particle based on its agegroup. The three components are adjusted to make the search better selective if a particle is old sufficient to be allocated to an older age group. This change is intended to help antiquity nanoparticles upgrade their pbests by enhancing their local search capabilities.

Furthermore, every particle aged 0 is allocated the average range of, ω , c_1 and c_2 , with 0.730, 1.430 & 1.438. Putting a component in an older age group changes the three components [34]:

$$\omega_i^t = \omega - \theta \cdot g_i^t \tag{3}$$

$$c_{1,i}^t = c_1 - \theta \cdot g_i^t \tag{4}$$

$$c_{2,i}^t = c_2 + \theta \cdot g_i^t \tag{5}$$

where g_i^t is particles i 's age-group in the t^{th} repetition and θ influences. Based on these EQs, if input in an older group, and ω and c_1 are decreased by Θ and c_2

goes up. They have chosen the value of g_i^t . which is a very tiny Θ variable that makes sure the three factors vary within a reasonable range.

3.5 Mutation strength alteration

An essential operator in this work is the mutation operator. Unlike typical individual line or stochastic length modification in PSOs, the proposed evolutionary scheme employs element lifespan to determine mutation intensity. This operator increases ancient particles' pbest updating chances. Mutation frequency (ms) for component i :

$$ms_i = \begin{cases} \frac{D}{2^{s-z_i^t+1} - s + g_i^t} & \alpha_i \leq \tau \\ \frac{D}{2} & \alpha_i > \tau \end{cases} \tag{6}$$

where the mapping function determines the population's maximum agegroups. If $\alpha_i = 0$ just one dimension of the particle i will be altered, much as with one point mutation. The mutation length l_p , which ranges from one to half of the dimension of the particles, grows along with the growth in α_i . If $\alpha_i > \tau$, PSOAG's maximum size is $D/2$. PSOAG's architecture is Algorithm.

Algorithm 3: Particle role in AMPO

1. Initialize the variable limit x_{\min} & x_{\max} ;
2. Produced an original swarm S utilizing range P ;
3. evaluate these count intervals =0;
4. initialize the swarm particles $\alpha_i = 0 (i=1,2, \dots, P)$;
5. when the halt condition is not met, progress
6. The aging operator age groups (S, α_i) are used to remove atoms $\alpha > \tau$ and replace them with new ones. The age-group topological structure is constructed using the () function.
7. end if
8. for $i = 1:P$ do
9. $A w_i$ alteration (S, ω, α); B inertial weight adjust
10. C_i adaptation (S, c_1, c_2, α); velocity remains constant
11. Inform the position & velocity
12. if the mutation form is fulfilled then
13. ms_adaptation (S, a).
14. end i
15. fitness calculate ($S, fevals$);
16. Update age accordingly.

In this instance, the sender network greets the nodes along a specified path that AOMDV has returned. We suggest that if no CTS is generated, then $F_c = 0$, which indicates the presence of a collision.

$$F_c = \begin{cases} 1 / RTT, & \text{CTS is received} \\ 0, & \text{No CTS is received} \end{cases} \tag{7}$$

Data packets may be dropped throughout a route if $Q \leq N$ because of anticipated traffic congestion at one node. It is preferable in this instance to avoid excluding this method from the suggested alternatives. If $Q \leq N$, the calculated route may join the pool of optimal routes dependent on the other fitness operating characteristic. The proposed model offers a method for the fitness functional where the overloaded efficiency functional element F_q will either have any values or be restored to 0, depending on the condition $Q \leq N$. Equation (8) is used to calculate the value, and B is the reservoir size. If $Q \leq N$ is true, which denotes that the route may receive packets for transferring data, then the value is computed. If not, the route probably has traffic at one or more of its endpoints, so we can modify the value of F_q to 0.

The current method provides the fitness service where another overloaded fitness functional portion F_q either has some values or restores to 0, depending on the condition $Q \leq N$. Equation (8) is used to calculate the value, wherein B is the buffering size. If $Q \leq N$ is true, which denotes that the network may receive packages for the transmission of data, then the value is computed. Otherwise, the route probably experiences congest-

tion at individual or many of its terminals, so we simply change F_q to 0.

$$F_q = \begin{cases} 1 - \frac{Q}{B}, & Q \leq N \\ 0, & Q > N. \end{cases} \quad (8)$$

Where F_c : collision, F_q : queue length and F_s : stability. All routes between the origin and the target FFs are sorted from greatest to lowest, and the path with the greatest FF ratio is chosen. As shown in Fig 12, shows the connection S& D. The threshold value is calculated by averaging each component. (I.e. F_{cavg} , F_{qavg} and F_{savg}) using equation (9). We construct this mean amount as our predefined threshold and determine if every element have a larger value than the normal range in equation 9 by evaluating it to the overall average [35].

$$F_{xavg} = \frac{\sum_{i=1}^n \sum_{j=1}^m F_{xij}}{n \times m} \quad (9)$$

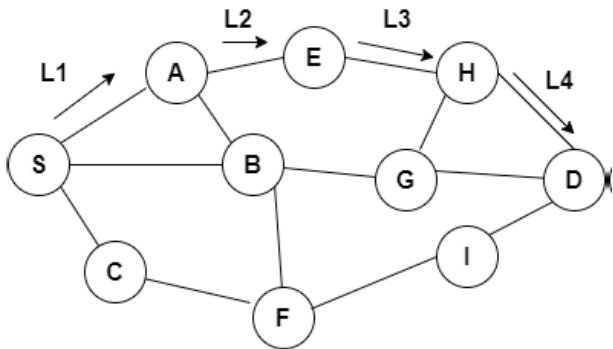


Figure 5: AOMDV-routing mechanism

3.6 Path stability probabilities (PSPs)

When a packet arrives at an RREPs from the target address, the PSP value can be obtained eq (10) [21] this computes the LBPs values between both networks and the optimization algorithm of the link security F_s .

$$PSP_i = \prod_{l=1}^L (1 - LBP_l) \quad (10)$$

$$F_s = PSP_i$$

PSPs are computed for route l for every connection l in the collection of links L . To calculate the new PSPs number and modify the PSPs, utilize eq (11). Lastly, eq (12) chooses the most reliable AOMDV method pathway.

Algorithm 4: Fitness evaluation for every router

- 1: l/p : For every router data retrieved from AOMDV-AMPO
- 2: O/p : Array of Function data
- 3: for every ($i=0; i \leq n; i++$)
- 4: F_c evaluation in eq 7
- 5: F_q Evaluation
- 6: F_s Evaluation
- 7: F_{xavg} evaluation
- 8: if ($F_c > F_{cavg}$)
- 9: if ($F_q > F_{qavg}$)
- 10: if ($F_s > F_{savg}$)
- 11: $FF = F_c + F_q + F_s$
- 12: end all

4 Experimental results and discussions

For the proposed model, the FF values has to be equalized to their defined average as per the aging population strategy. The performance of BCSMT scheme is analyzed by using NS2. The nodes have to be configured as mobile nodes by using the node-config command in NS2. The radio waves are propagated by using the propagation model two ray ground. The nodes are distributed in the simulation environment. The parameters used for the simulation of AMPO scheme is described in Table. The simulation of AMPO has 100 nodes deployed in the simulation area 500×500 . The nodes are communicated with each other by using the communication protocol User Datagram Protocol (UDP). The nodes are moved randomly within the simulation area by using the mobility model Random waypoint. All the nodes receive the signal from all direction by using the Omni directional antenna. The traffic is handled using the traffic model Constant Bit rate (CBR). The performance of AMPO scheme is evaluated by the parameters PDR, routing overhead, end to end delay, throughput etc.

Table 1: Simulation setup

Parameter	Value
Number of Nodes	100
Simulation Area	$500 \times 500 m^2$
Channel BW	1Mbps
Size of data packet	1 kB
Initial energy (Normal-Nodes-77)	1J
Initial energy (Advanced-Nodes-23)	5J
Processing Delay	50 μ s
ϵ_{fs}	10pJ/bit/ m^2
ϵ_{mp}	0.0013pJ/bit/ m^4
E_{elect}	50nJ/bit
E_{DA}	5nJ/bit/signal

Packet delivery ratio assessment

Fig 6 & 7 compare the PDR to the number of networks and simulated period. The simulated duration increases, routing protocol monitoring the much more packets. It increases network traffic, which causes congestion at the relay nodes or collisions at connections. That results in much more lost or colliding bits and hence impacts the system severely. AOMDV-AMPOs and AOMDV-FFs provide more packets than AOMDV-TAs and EHO-AOMDVs. Congested networks or accidents will consequence the low FFs ratings, therefore pathways were to be kept away from it. Other methods don't utilize this approach. Table 2 shows that AOMDV-AMPO increases PDR by 4.5%, 10.29%, & 15% compared to AOMDV-FFs, AOMDV-TAs, & EHO-AOMDVs.

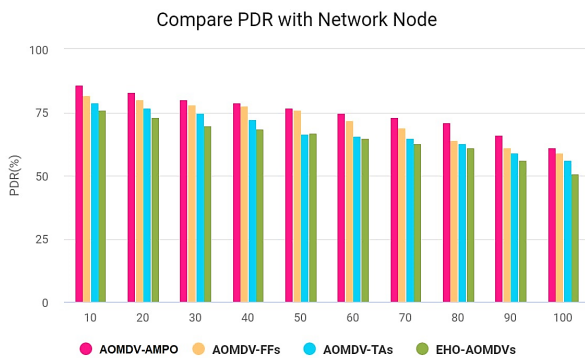


Figure 6: Computation of PDR vs network nodes

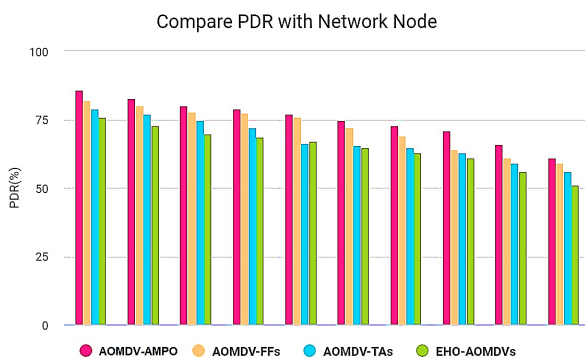


Figure 7: Computation of PDR vs simulation time

Table 2: PDR computation

No. of Vertices	AOMDV-AMPO	AOMDV-FFs	AOMDV-TAs	EHO-AOMDVs
10	86	82	79	76
20	83	80	77	73
30	80	78	74.9	70
40	79.13	77.53	72.3	68.8
50	77	76	66.6	67
60	75	72	65.6	65
70	73	69	65	63
80	71	64	63	61

90	66	61	59	56
100	61	59	56	51
Sum	742.13	709.53	673	641.8
Gain %		4.5	10.29	16

B. Throughput assessment

The number of nodes, percentage of defective endpoints, mobility speed (m/s), loss of packets (%), and simulated duration are used to measure throughput (s). Figure 8 shows how network performance depends on node count. With additional nodes available for packet data transfers comes the risk of traffic congestion and even more conflicts at the network's intermediate nodes. This will lower throughput. Our suggested protocols, AOMDV-AMPOs, and AOMDV-FFs concentrate on selecting the route with the greatest network reliability and least unreliable, which lowers the likelihood of traffic issues like congestion and conflict.

Fig 9 shows throughput vs malfunctioning nodes. We assume malfunctioning nodes in AOMDV networks and test each protocol in different circumstances. There may be a variety of causes for malfunctioning nodes, including battery drain or collisions between mobile nodes. We are concentrating on four distinct scenarios for malfunctioning nodes. Networking performance degrades as the frequency of defective networks increases and more node failures mean that less incoming information will reach the target, which lowers the transmission speed. This is because routes with problematic nodes will be ignored since the Round Trip Time (RTT) is in formulae (1) and (2).

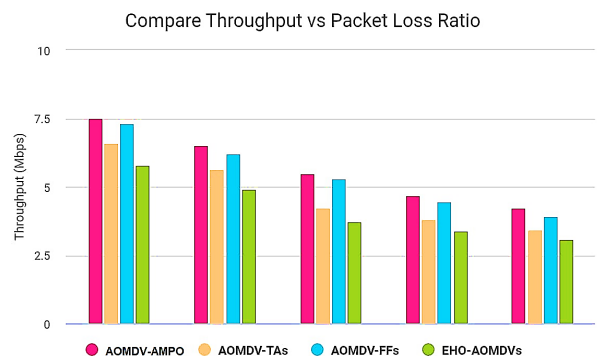


Figure 8: Computation of throughput vs node numbers

The efficiency is shown against mobility speed in Fig 10. Links are often unstable as a result of the nodes' constant movement. Our program chooses the most stable path with the fewest velocities and node motion. At high node speeds, when such unstable pathways are avoided by our algorithms, this system performance becomes more apparent.

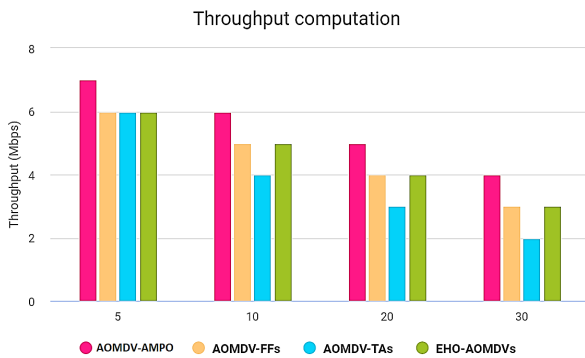


Figure 9: Computation of throughput vs faulty nodes



Figure 10: Computation of throughput vs speed of mobility

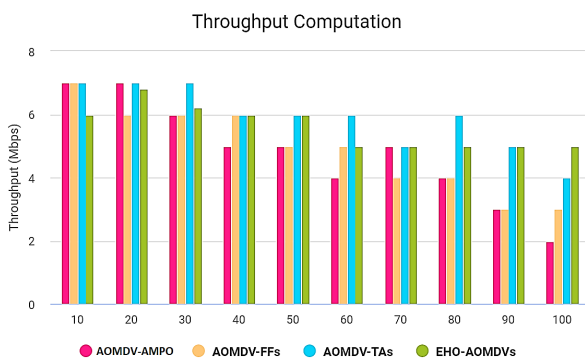


Figure 11: Computation of throughput vs loss of packets

Fig 12 shows how packet loss impacts network performance. The total quantity of packets not acquired at the target is multiplied by the amount of data packets from the source to get the packet loss rate. Data collision, insufficient node energy, and excessive node mobility are all potential causes of packet loss. Because we are concentrating on lowering the frequency of collisions in a certain network, our suggested protocols AOMDV-AMPO and AOMDV-FF are performing better than AOMDV-TA and EHO-AOMDV. According to Table 3, AOMDV-AMPOs increase throughput evaluation to AOMDV-FFs, AOMDV-TAs, and EHO-AOMDVs by 4.38%, 20.19%, and 35.70%, correspondingly. The stochastic

network of nobilities, such as data latency and collision rises with time, and hence throughput decreases. Our methods, therefore, keep clear of these risky pathways, which improves throughput performance in comparison to other procedures.

Table 3: Throughput vs Packet Loss Range

Packet loss	AOMDV-AMPOs	AOMDV-TAs	AOMDV-FFs	EHO-AOMDVs
0	7.51	6.61	7.31	5.81
1	6.51	5.64	6.25	4.91
2	5.51	4.21	5.32	3.74
3	4.71	3.81	4.46	3.41
4	4.22	3.43	3.92	3.11
Sum	28.5	23.64	27.22	20.94
Gain %		20.19	4.38	35.68

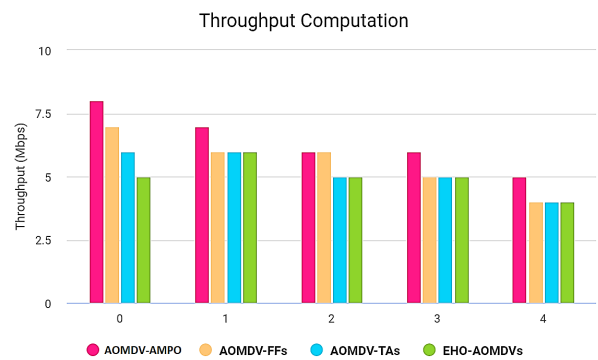


Figure 12: Computation of throughput vs simulation time

End 2 end latency assessment

Data retransmissions rise as a result of the traffic difficulties in Fig. 21 and as the total number of nodes rises. This requires more nodes and time to identify the optimum paths. These factors will extend the process. The time required by our suggested techniques decreases as the quantity of packet forwarding decreases.

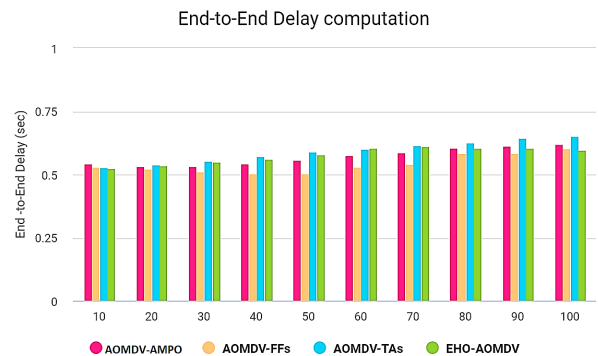


Figure 13: Computation of latency vs node numbers

Fig 13 shows how broken nodes affect end-to-end latency, similar to Figure 13. Before or during information transfer, the network might malfunction. If this happens while data is being sent, a time delay is needed to alert the transmitters of the route connection, an alternate route is investigated, and information restoration is started. The end-to-end latency would therefore decrease. If a network fails before data transmission, our methods will eliminate specific pathways.



Figure 14: Computation of latency vs faulty nodes

Routes would probably be lost due to the movement of nodes, which might lead to packets dropping. Repeated data transfers would lengthen the end-to-end latency. This procedure performed then the rivals as they eliminate those problematic routes

Energy consumption assessment

Fig 15 & 16 show how our procedures cut down on the nodes' efficiency use by reducing the number of times packets have to be sent again. As nodes or time advance, computational time and energy increase. According to Table 4, AOMDV-AMPO saves fuel evaluate to AOMDV-FFs, AOMDV-TAs & EHO-AOMDVs by 10.76%, 61.97%, and 32.33%, respectively.

Routing overhead assessment

Fig 17 & 18 shows the no. of computational cost progression boosts the quantity of RREQs packets floods in the system, increasing the latency in the 132960

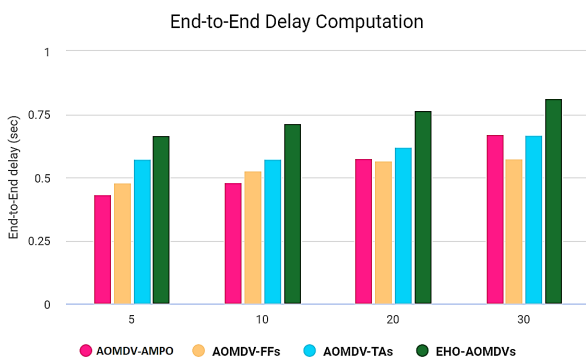


Figure 15: Computation of latency vs speed

VOLUME network. The route discovery procedure is activated more often due to node migration and route instabilities, which increases this overhead. As mentioned previously, our algorithms base their route optimization on the FF.

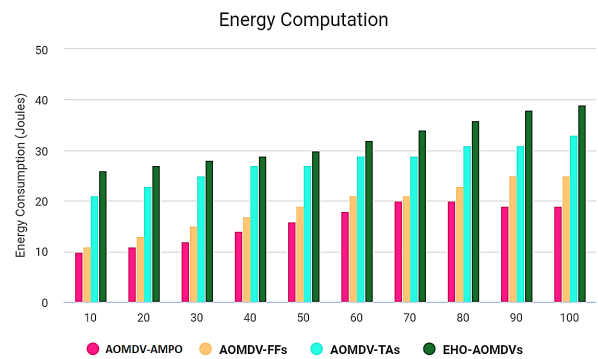


Figure 16: Computation of energy utilization vs node number

Table 4: Energy utilization

No. of Vertices	AOMDV-AMPOs	AOMDV-FFs	AOMDV-TAs	EHO-AOMDVs
10	17	18	32	27
20	19	20	32.3	27.3
30	19	22	7434	27.10
40	22.13	23.53	7236	28.2
50	22.9	24.5	6639	28.9
60	24	27	6540.3	32.6
70	26	29	42.8	33.8
80	30	30.9	46	35.6
90	32	33.8	47.3	36.8
100	33	35	47.5	38
Sum	235.9	254.10	380.4	310.8
Gain %		10.78	62.97	33.33

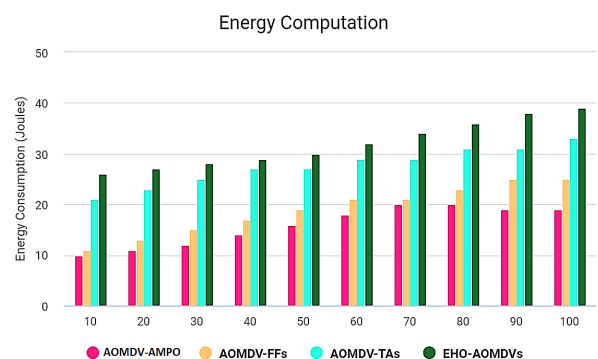


Figure 17: Computation of energy utilization vs node number

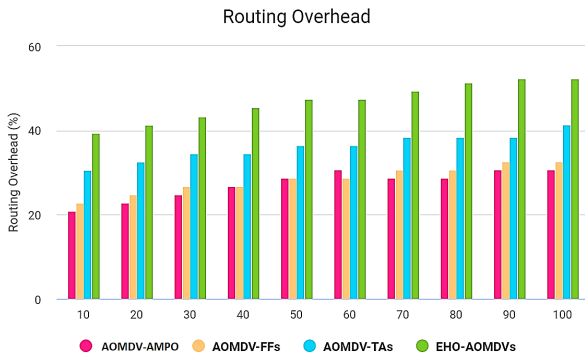


Figure 18: Computation of routing overhead vs node number

As a consequence, our methods have less complexity than conventional methods. AOMDV-AMPO decreases network loops by 12.55%, 33.35%, and 74.45%, respectively, when compared to AOMDV-FFs, AOMDV-TAs, & EHO-AOMDVs, as shown in Table 5.

Table 5: Routing overhead

No. of Vertices	AOMDV-AMPOs	AOMDV-FFs	AOMDV-TAs	EHO-AOMDVs
10	27	28	35	47
20	27.3	31	37	49
30	27.30	32	38.91	49
40	28.2	34	38.61	50.7
50	32.7	35.82	41.8	53
60	33.8	37	43	57
70	34.6	38.37	43.8	59
80	37	41	45.6	60.3
90	5.2	42.54	48	61.2
100	39	43	50	61.9
Sum	310.8	350.70	416.4	543
Gain %		13.55	33.36	75.45



Figure 19: Computation of routing overhead vs simulation period

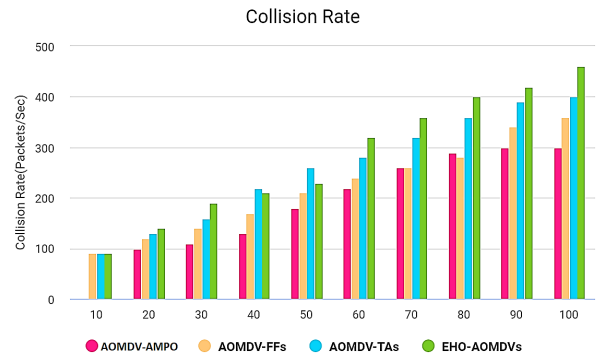


Figure 20: Computation of collision rate vs node number

Rate of collision assessment

Fig. 20 displays this frequency at packet headers lost. With more nodes, more information must be sent so that the likelihood of a collision grows. Utilizing the equation's RTT algorithm our procedure chooses the path with the lowest likelihood of a collision.

Broken nodes cause the routers to terminate much more often. By increasing the number of RREQ frames broadcasting in the network. Thus, data conflicts commonly occur in the three-way handshake phase, as shown in Fig. 21 and 22. Our methods provide more dependable routes, which lowers the number of RREQ messages and Request To Send / Clear To Send (RTS/CTS) exchanges while also reducing collision rates.

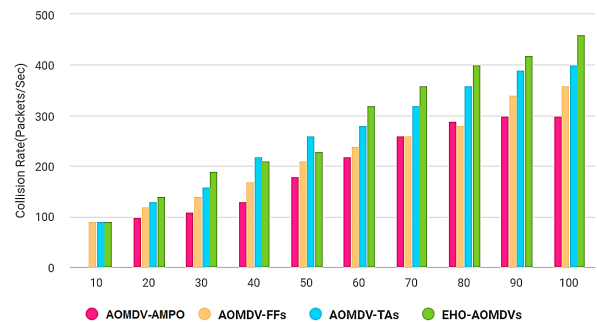


Figure 21: Computation of collision rate vs speed of mobility

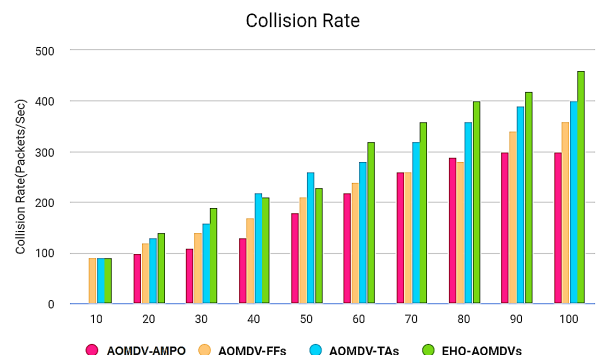


Figure 22: Computation of collision rate vs faulty nodes

5 Conclusions

The rapid rate of mobility of nodes produces data collision, which ultimately results in the loss of packets and has a devastating effect on the performance of the network by reducing its throughput. Random node movement produces unstable linkages and topological change. Additionally, the bottlenecks of the intermediary nodes may experience traffic congestion, which results in data dropouts. Packet retransmission is induced in certain circumstances, which increases the network overhead and overflows the network, exacerbating the traffic issues. As a result, the network's overall lifespan is decreased and the end-to-end delay increases. In this study, we make use of and improve the routes the AOMDV technique returns. The focus of the suggested AMPO technique is on establishing reliable connectivity with minimal PDR and energy consumption to fix the flaw of ineffective cluster system monitoring. We introduced the FF concept, and the communication as a whole is built on FF. The comparison results show that the suggested optimization outperforms the current approaches across the board.

Security must be taken into account in futuristic work with the usage of a confidence aware secure efficient energy navigating model in MANETs by utilising hybrid techniques, and the effectiveness of those algorithms will be analysed by enforcing higher number of security vulnerabilities.

6 Conflict of interest

The authors declare no conflict of interest.

7 References

1. Sandeep Monga, J.L. Rana, Jitendra Agarwal, Clustering schemes in mobile ad-hoc network (MANET): a review, 08, Int. J. Sci. Technol. Res. 8 (AUGUST 2019), 2277–8616.
2. L.M. Tuan, L.H. Son, H.V. Long, L.R. Priya, K.R. Soundar, Y.H. Robinson, R. Kumar, ITFDS: channel-aware integrated time and frequency-based downlink LTE scheduling in MANET, Sensors 20 (12) (2020) 1–20.
3. Vargheese, M., Vanithamani, S., David, D. S., & Rao, G. R. K. (2023). Design of Fuzzy Logic Control Framework for QoS Routing in MANET. Intelligent Automation & Soft Computing, 35(3).
4. P. Elamparithi, K. RubaSoundar, Trusted sensing model for mobile ad hoc network using differential evolution algorithm, Int. J. Information. Technol. Control 49 (4) (December 2020) 556 563.
5. Houlding, P. (2023). A Review of the Replicability and Implementation of the Efficient Clustering Scheme for MANETs in Remote Canadian Communities.
6. V. Selvakumar, K. RubaSoundar, Deep Reinforcement Learning for Building Honeypots against Runtime DoS Attack” International Journal of Intelligent Systems, Wiley online library, October 2021, <https://doi.org/10.1002/int.22708>.
7. A.V. Vasilakos, Z. Li, G. Simon, W. You, Information-centric network: research challenges and opportunities, J. Netw. Comput. Appl. 52 (2015) 1–10 (Elsevier Ltd).
8. Preethi, P., & Asokan, R. (2020, December). Neural network oriented roni prediction for embedding process with hex code encryption in dicom images. In Proceedings of the 2nd International Conference on Advances in Computing, Communication Control and Networking (ICACCCN), Greater Noida, India (pp. 18-19).
9. Bai, D. P., & Preethi, P. (2016). Security Enhancement of Health Information Exchange Based on Cloud Computing System. International Journal of Scientific Engineering and Research, 4(10), 79-82.
10. Karthick, K., & Asokan, R. (2021). Mobility aware quality enhanced cluster based routing protocol for mobile ad-hoc networks using hybrid optimization algorithm. Wireless Personal Communications, 119(4), 3063-3087.
11. Nivetha, S. K., Asokan, R., & Senthilkumaran, N. (2019, May). Metaheuristics in Mobile AdHoc Network Route Optimization. In 2019 TEQIP III Sponsored International Conference on Microwave Integrated Circuits, Photonics and Wireless Networks (IMICPW) (pp. 414-418). IEEE.
12. Sunil Pathak, Sonal Jain, An optimized stable clustering algorithm for mobile ad hoc networks, Pathak Jain EURASIP J. Wireless Commun. Networking (2017) (2017) 51, <https://doi.org/10.1186/s13638-017-0832->
13. Z. Chen, W. Zhou, S. Wu, and L. Cheng, “An adaptive on-demand mul-tipath routing protocol with QoS support for high-speed MANET,” IEEEAccess, vol. 8, pp. 44760_44773, 2020.
14. A. Taha, R. Alsaqour, M. Uddin, M. Abdelhaq, and T. Saba, “Energy efficient multipath routing protocol for mobile Ad-hoc network using the fitness function,” IEEE Access, vol. 5, pp. 10369_10381, 2017.
15. S. Sarhan and S. Sarhan, “Elephant herding optimization Adhoc on-demand multipath distance vector routing protocol forMANET,” IEEE Access, vol. 9, pp. 39489_39499, 2021, <https://doi.org/10.1109/ACCESS.2021.3065288>.

16. Al-Shareeda, M. A., & Manickam, S. (2022). Man-in-the-middle attacks in mobile ad hoc networks (MANETs): Analysis and evaluation. *Symmetry*, 14(8), 1543.
17. Singh, S., Pise, A., Alfarraj, O., Tolba, A., & Yoon, B. (2022). A cryptographic approach to prevent network incursion for enhancement of QoS in sustainable smart city using MANET. *Sustainable Cities and Society*, 79, 103483.
18. A. Bhardwaj and H. El-Ocla, "Multipath routing protocol using genetic algorithm in mobile Ad hoc networks," *IEEE Access*, vol. 8, pp. 177534_177548, 2020, <https://doi.org/10.1109/ACCESS.2020.3027043>.
19. Z. Lin and J. Sun, "Routing protocol based on link stability in MANET," in *Proc. World Automat. Congr. (WAC)*, Aug. 2021, pp. 260_264, <https://doi.org/10.23919/WAC50355.2021.9559469>.
20. Skokowski, P., Malon, K., & Łopatka, J. (2022). Building the Electromagnetic Situation Awareness in MANET Cognitive Radio Networks for Urban Areas. *Sensors*, 22(3), 716.
21. V. Tilwari, A. Bani-Bakr, F. Qamar, M. N. Hindia, D. N. K. Jayakody, and R. Hassan, "Mobility and queue length aware routing approach for network stability and load balancing in MANET," in *Proc. Int. Conf. Electr. Eng. Informat. (ICEEI)*, Oct. 2021, pp. 1_5, <https://doi.org/10.1109/ICEEI52609.2021.9611119>.
22. M. Farsi, M. Badawy, M. Moustafa, H. Arafat Ali, and Y. Abdulazeem, "A congestion-aware clustering and routing (CCR) protocol for mitigating congestion in WSN," *IEEE Access*, vol. 7, pp. 105402_105419, 2019.
23. P. Pal, S. Tripathi, and C. Kumar, "Bandwidth estimation in high mobility scenarios of IEEE 802.11 infrastructure-less mobile Ad hoc networks," *Int. J. Commun. Syst.*, vol. 32, no. 15, p. e4080, Oct. 2019.
24. Patel, S., & Pathak, H. (2022). A mathematical framework for link failure time estimation in MANETs. *Engineering Science and Technology, an International Journal*, 25, 100984.
25. N. R. Patel, S. Kumar, and S. K. Singh, "Energy and collision aware WSN routing protocol for sustainable and intelligent IoT applications," *IEEE Sensors J.*, vol. 21, no. 22, pp. 25282_25292, Nov. 2021, <https://doi.org/10.1109/JSEN.2021.3076192>.
26. U. Srilakshmi, N. Veeraiah, Y. Alotaibi, S. A. Alghamdi, O. I. Khalaf, and B. V. Subbayamma, "An improved hybrid secure multipath routing protocol for MANET," *IEEE Access*, vol. 9, pp. 163043_163053, 2021, <https://doi.org/10.1109/ACCESS.2021.3133882>.
27. N. Muruganantham and H. El-Ocla, "Routing using genetic algorithm in a wireless sensor network," *Wireless Pers. Commun.*, vol. 111, no. 4, pp. 2703_2732, Apr. 2020.
28. F. Sarkohaki, R. Fotohi, and V. Ashra'an, "An efficient routing protocol in mobile Ad-hoc networks by using artificial immune system," 2020.
29. M. Ghafouri Vaighan and M. A. JabraeilJamali, "A multipath QoS multi-cast routing protocol based on link stability and route reliability in mobile Ad-hoc networks," *J. Ambient Intell. Humanized Comput.*, vol. 10, no. 1, pp. 107_123, Jan. 2019, <https://doi.org/10.1007/s12652-017-0609-y>.
30. A. Naushad, G. Abbas, Z. H. Abbas, and A. Pagourtzis, "Novel strategies for path stability estimation under topology change using hello messaging in MANETs," *Ad Hoc Netw.*, vol. 87, pp. 76_99, May 2019.
31. R. Hemalatha, R. Umamaheswari, and S. Jothi, "An efficient stable node selection based on Garson's pruned recurrent neural network and MSO model for multipath routing in MANET," *Concurrency Comput., Pract. Exper.*, vol. 34, no. 21, Sep. 2022, <https://doi.org/10.1002/cpe.7105>
32. Ramalingam, R., Muniyan, R., Dumka, A., Singh, D. P., Mohamed, H. G., Singh, R., ... & Noya, I. D. (2022). Routing Protocol for MANET Based on QoS-Aware Service Composition with Dynamic Secured Broker Selection. *Electronics*, 11(17), 2637.
33. Venkatasubramanian, S. (2022, January). Fruit-Fly Algorithm Based Dynamic Source Routing Algorithm for Energy Efficient Multipath Routing in MANET. In *2022 International Conference on Computer Communication and Informatics (ICCCI)* (pp. 01-08). IEEE.
34. Branko Skocir, Gregor Papa, Anton Biasizzo, "Multi-hop communication in Bluetooth Low Energy ad-hoc wireless sensor network," *Informacije MIDEM*, vol. 48, no. 2, 2018, pp. 61-68.
35. Kumar, M. P., Kumar, M. M., Shobana, S., Padmanaban, L., Nageswaran, A., & Krishnamoorthy, R. (2022, April). Enhanced Secure Routing in MANET using Collaborative Machine Learning Approach. In *2022 8th International Conference on Smart Structures and Systems (ICSSS)* (pp. 1-6). IEEE.



Copyright © 2024 by the Authors. This is an open access article distributed under the Creative Commons Attribution (CC BY) License (<https://creativecommons.org/licenses/by/4.0/>), which permits unrestricted use, distribution, and reproduction in any medium, provided the original work is properly cited.

Arrived: 06. 01.2 024
Accepted: 22. 04. 2024

Software Defined Network Architecture Based Network Slicing in Fifth Generation Networks

Parameswaran Ramesh¹, Bhuvaneshwari Mohan¹, Lavanya Viswanath¹, Bino Jesu Stephen^{1,2}

¹Department of Electronics Engineering, Madras Institute of Technology, Anna University, Chennai, India

²Department of Electronics and Communication Engineering, St. Joseph's Institute of Technology, Chennai, India

Abstract: Network slicing is a promising approach that can cater to the need for differential services. It can be employed to improve the performance of users. In Fifth Generation (5G) networks, it is adopted to enhance the Quality of Experience (QoE) of the clients of differential services. In this research, 5G clients of five distinct services in different combinations in two scenarios are considered. They are Enhanced Mobile Broadband (eMBB), Massive Machine Type Communication (mMTC), Ultra Reliable Low Latency Communication (URLLC), voice, and Enhanced Mobile Broadband Prioritized (eMBB_p) clients. This study develops Software Defined Networks (SDN) architecture-based network slicing in a 5G network. It is simulated using Python 3.7. Whenever the bandwidth available on the client-associated Base Stations is not sufficient to meet their service requirements, the process of network slicing is invoked. It consists of slice creation and slice allocation. Both of these modules are governed by Network slicing management. The amount of slice depends on the service requirements of the active clients. In scenario 1, the active clients are assumed to be 96. There are some combinations: 70 eMBB, 10 mMTC, 10 URLLC, 2 voice, and 4 eMBB_p. while in scenario 2, it is 52 eMBB, 21 mMTC, 15 URLLC, 24 voice, and 5 eMBB_p. As per the 3GPP standard, the bandwidth required for eMBB_p is 10 G bit/s. The bandwidth available per Base Station is 6 G bit/s; however, 1 G bit/s is assigned for signaling, and hence only 5 G bit/s are available per Base Station to serve the clients. From the simulation results, it is found that scenarios 1 and 2 achieve bandwidth utilization of 24% and 38%, respectively.

Keywords: Network Slicing; 5G; SDN; QoE

Programsko definirana omrežna arhitektura, ki temelji na rezinjenju omrežja v omrežjih pete generacije

Izveček: Rezinjenje omrežja je obetaven pristop, ki lahko zadovolji potrebe po različnih storitvah. Uporablja se lahko za izboljšanje zmogljivosti uporabnikov. V omrežjih pete generacije (5G) se uporablja za izboljšanje kakovosti izkušenj (QoE) odjemalcev različnih storitev. V tej raziskavi so obravnavani odjemalci petih različnih storitev 5G v različnih kombinacijah v dveh scenarijih. To so izboljšani mobilni širokopasovni odjemalci (eMBB), masivna komunikacija strojnega tipa (mMTC), zelo zanesljiva komunikacija z nizko zakasnitvijo (URLLC), glas in izboljšani mobilni širokopasovni prednostni odjemalci (eMBB_p). Študija razvija na arhitekturi SDN (Software Defined Networks) temelječe rezinjenje omrežja v omrežju 5G. Simulirana je z uporabo programa Python 3.7. Kadar pasovna širina, ki je na voljo na baznih postajah z odjemalci, ne zadostuje za izpolnitev njihovih zahtev po storitvah, se sproži postopek delitve omrežja. Sestavljen je iz ustvarjanja in dodeljevanja rezin. Oba modula ureja upravljanje rezinjenje omrežja. Količina rezine je odvisna od storitvenih zahtev aktivnih odjemalcev. V scenariju 1 se predpostavlja, da je aktivnih odjemalcev 96. Obstaja nekaj kombinacij: 70 eMBB, 10 mMTC, 10 URLLC, 2 glas in 4 eMBB_p. V scenariju 2 je to 52 eMBB, 21 mMTC, 15 URLLC, 24 glas in 5 eMBB_p. V skladu s standardom 3GPP je pasovna širina, potrebna za eMBB_p, 10 G bit/s. Pasovna širina, ki je na voljo na bazno postajo, je 6 G bit/s; vendar je 1 G bit/s dodeljen za signalizacijo, zato je na voljo le 5 G bit/s za servisiranje odjemalcev. Iz rezultatov simulacije je razvidno, da scenarija 1 in 2 dosegata 24-odstotno oziroma 38-odstotno izkoriščenost pasovne širine.

Ključne besede: rezinjenje omrežja; 5G; SDN; QoE

* Corresponding Author's e-mail: parameswaran0789@gmail.com

How to cite:

P. Ramesh et al., "Software Defined Network Architecture Based Network Slicing in Fifth Generation Networks", Inf. Midem-J. Microelectron. Compon. Mater., Vol. 54, No. 2(2024), pp. 123–130

1 Introduction

In general, public networks [1] provide ease of usage and a wider range of coverage with limited resources as the number of users availing of the resources increases. It suffers from latency and bandwidth constraints, which in turn influence the Quality of Service (QoS) experienced by the customers. On the other hand, a standalone private network [2] ensures services to limited customers with assured QoS. The private network can be considered a logical or virtual network. One of the primary factors contributing to the emergence of future fifth generation (5G) networks is the imperative to efficiently support a wide range of novel use cases on a shared network infrastructure.

5G of wireless communication is envisioned to provide a higher data rate, lesser latency, and enhanced capacity when compared to existing Fourth Generation (4G) networks. Various industries that are moving towards complete automation have slowly started to adopt 5G since the connectivity services offered by 5G are more promising. The connectivity services can be classified into three categories: enhanced mobile broadband (eMBB), massive Machine Type Communication (mMTC), and ultra-reliable low latency communication (URLLC) [3]. Due to the enhanced features supported by 5G, the QoS experienced by applications also gets enhanced.

In order to increase revenue, the service providers of 5G are exploring the business model through the concept of network slicing. Network slicing [4] is fundamentally overlaying a private or virtual network onto the existing infrastructure network. The flexibility is introduced so that each slice of the network can have its own logical structure, security protocol, performance requirements, etc.

The concept of network slicing introduced in 4G [5] confined its operations within the same infrastructure. Access Point Name Routing, Multi-Operator Core Network (MOCN), and Dedicated Core Network [6] are used for this realization. The concept of virtualization [7] is introduced in 5G along with the existing Radio Access Networks (RANs) [8] to realize network slicing. Through network slicing, the service providers make meaningful commitments to the customers by ensuring their expected QoS.

A network slice possesses self-contained characteristics, meaning that it may function independently after deployment, without requiring human involvement, by relying on the provided customizable governance model. This characteristic renders slices as customized virtual networks that provide self-contained function-

ality. In this context, it is possible for each network slice to possess distinct network architecture, engineering methods, and dynamic resource provisioning algorithms. With these features in place, the network slice may function as a smart platform that can automatically adjust its settings to meet the requirements of any given use case.

Network slicing allows a mobile operator to create virtual networks tailored to individual customers and use cases. 5G envisions support for applications such as mobile broadband, machine-to-machine communications, connected cars, etc. These applications need faster, lower-latency, and edge computing resources. A 5G operator may tailor solutions to individual enterprises by prioritizing resources in distinct slices. Slicing can tremendously assist Mobile Virtual Network operators (MVNOs) [9]. Slicing may also improve service continuity by constructing a virtual network that spans numerous local or national networks or by enabling a host network to create an optimal virtual network that matches the devices available in the existing network [10].

As mentioned earlier, all the applications that are driven by 5G can be classified under various categories, namely eMBB, mMTC, and URLLC. The QoS requirements of each of the above vary with respect to latency, bandwidth, and connectivity.

eMBB [3] is used in Smart offices and large-scale event applications. They are driven by voluminous data and, hence, are in need of higher data rates over a wider area. The applications of URLLC [3] are remote surgery, autonomous cars, and Tactile Internet. They have rigorous standards to deal with latency and dependability. The requirement of mMTC [3] is to handle a higher number of devices in a limited area that may only transmit data intermittently. The Internet of Things (IoT) is one of the use cases in this category. Hence, to satisfy the above application-specific QoS, portioning in the logical network is made by the service providers through the concept of network slicing.

The rest of the Article is organized as follows: Section II discusses the state of the art related to existing work. Section III describes the proposed work in detail. Section IV describes the observations made based on the findings. Section V culminates by detailing the importance of the outcome of the study and highlighting the prospects of future work.

2 Literature survey

The author of [11] has presented a comprehensive review of the advancement of wireless technology solu-

tions, namely 5G cellular network designs. The author elaborated on the following concepts, which will include a subset of the technical components: Device to Device Communication (D2D), Massive Machine Communication (MMC), and Ultra-reliable Networks (URN). The primary propagation challenges associated with mm wave propagation for 5G wireless communications are route loss, blocking, atmospheric effects, and absorption.

The author of [12] examined 5G wireless mobile technologies that are made up of two logical layers: namely, a radio network and a network cloud. In terms of data throughput, spectrum efficiency, latency, capacity, energy efficiency, and QoS, the essential criteria of 5th generation wireless communication have been examined.

In [13], the author discusses the taxonomy developed for network slicing on the basis of various characteristics, namely core design concepts, enablers, slicing resource categories, customer-centric supply chaining schemes, basic infrastructure, and privacy. The author also explained the enabled smart applications, namely intelligent transport systems, smart industries, smart homes, health care, and smart grids.

In [14], the author developed an architecture of network slicing in 5G communications for heterogeneous wireless domains. The architecture is developed using cutting-edge technologies such as Long-Term Evolution-Advanced (LTE-A), Software Defined Network (SDN), etc. The author has presented the performance enhancements that could be achieved through the new architecture in various scenarios.

The author of [15] presented the benefits of incorporating network slicing concepts by integrating the physical 5G Infrastructure with SDN and Network Function Virtualization (NFV). From the studies carried out by introducing the dynamic architecture, it was found that a wide range of applications with expected performance were achieved.

The author of [16] examined the impact made by network slicing on the layered architecture of 5G. The layers considered for analysis are the infrastructure layer, network function layer, service layer, and Management and Orchestration (MANO). The functionalities of each layer were studied in context with network lifetime enhancement and the security of the network.

The authors of [17] investigated the performance of 5G by incorporating Network Slicing. A priority-driven, entry-controlled strategy is adopted for allocating resources to the incoming 5G traffic. This strategy con-

sists of both inter- and intra-slice priorities. The traffic pertaining to mMTC and eMBB is being investigated. The performance of NS3 simulator in reducing network congestion is analyzed.

From the above literature, it is observed that not much work has been carried out to investigate the impact of network slicing in 5G. The authors [17] have investigated the performance of the 5G incorporated in network slicing pertaining to traffic mMTC and eMBB.

In a realistic environment, the 5G network can have the composition of all services, namely eMBB, mMTC, URLLC, voice, and Enhanced Mobile Broadband Prioritized (eMBB_p). Hence, to explore the importance of network slicing with respect to bandwidth utilization.

This research considers different scenarios, and the results obtained for the best scenario are detailed in this article, which is claimed to be the novelty behind this research.

The investigation into QoS achieved by each service and different scenarios under the bandwidth utilization strategy adopted above is in progress.

3 Proposed methodology

In this research, two scenarios are investigated in order to allocate bandwidth to customers. By creating network slices on demand, mobile operators may effortlessly and dynamically serve new use cases. The services offered by 5G will create demand based on user requirements and by incorporating the SDN network to maintain QoS.

3.1 System Model

The system model of network slicing in 5G is presented in Figure 1. In this, the 5G network is layered with SDN to provide efficient bandwidth to the user.

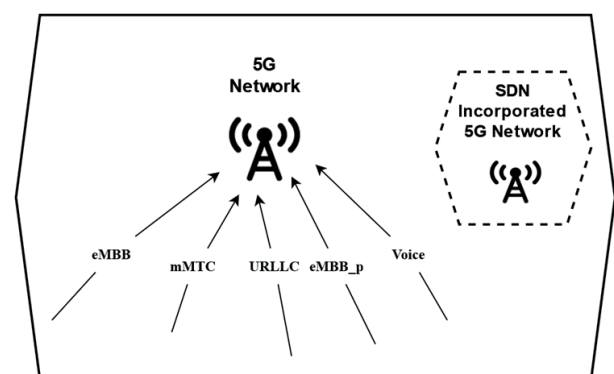


Figure 1: System model of network slicing in 5G Network

In this investigation, the services that are supported by the concept of network slicing are eMBB, mMTC, URLLC, voice, and eMBB_p. In cases where the bandwidth is not sufficient for the transmission of data offered by these services, they are regulated by using the SDN-incorporated 5G network to maintain the QoS.

3.2 Network Slicing in 5G

Let β_{ϵ_i} be the total bandwidth required for the differential services associated with the Base station. Let β_{5G} be the bandwidth available in the associated Base Station (BS) and β_{SDN} be the bandwidth offered through network slicing. Let ϵ_i be the service class of the clients dwelling in the network at any particular instant. Such that i varies from 1 to N . As mentioned earlier, each class of ϵ_i exhibits different service requirements as given in Table 1. Let ϕ_j be the number of BS present in the considered 5G scenario. Let δ_j be their serving capacity. Let α be the number of clients falling under ϵ_i service class being served by ϕ_j BS at any particular instant. Let Υ_{α} be the QoS requirements of each of these clients. The degradation in Υ is generally realized whenever the clients are not well connected with the BS. It also depends on their allocated resources. Whenever any of this reasoning is observed, the process of Network slicing is invoked. When β_{5G} exceeds its full capacity, a slice of resources pertaining to β_{SDN} is assigned to these clients. Thereby, the Υ offered to them is strengthened.

Table 1: 5G Services and its Bandwidth

Services	Bandwidth	Class
eMBB_p	10 G bit/s	5
eMBB	100 M bit/s	4
Voice	100 M bit/s	3
mMTC	10 M bit/s	2
URLLC	1 M bit/s	1

The SDN architecture-based network slicing in the 5G Network is shown in Figure 2. It consists of five different services, namely eMBB, mMTC, URLLC, Voice, and eMBB_p, which request Bandwidth from the serving BS and its class is shown in the Table 1. The BS initially checks whether the bandwidth available is sufficient to provide service-specific QoS to the requested client. If sufficient, services will be provided, and performance will be analyzed. Otherwise, the BS request from SDN Serving BS to provide slices to accommodate the requirements of the clients Thus, SDN allows different virtual networks to be overlaid on the same physical infrastructure.

eMBB_p traffic might be expressed mathematically as a function of user traffic. The mean arrival of λ_i of a single

user may be determined using the number of users (a_i) as follows:

$$\lambda_{eMBB_p} = a_i * \lambda_i \tag{1}$$

In this research, Network slicing is considered the primary component of the system model. This component assists in the generation of slices to meet the resource requirements of the client services considered in the scenario. Its generation depends on the features of the core network, RAN, and UE. It is further broken down into its subcomponents, namely, Slice creation, Slice allocation, and Slice management. Slice creation does the slicing of the 5G network with the aid of SDN. Slice allocation separates the entire type of slices, while slice management controls the entire process involved in the above two.

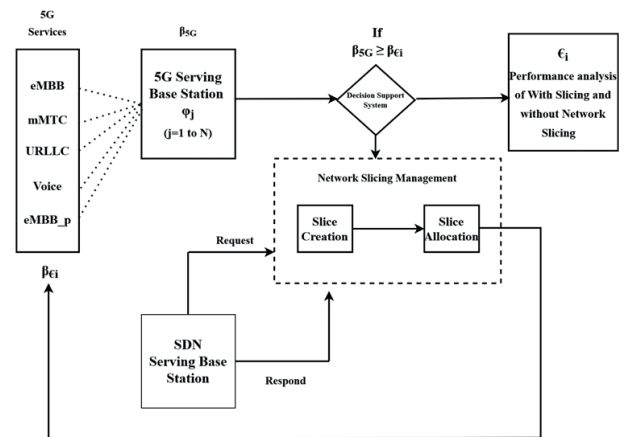


Figure 2: Proposed SDN Architecture Based Network Slicing in 5G network

After slicing, using the feedback mechanism, it provides bandwidth to all the services.

3.3 5G networks

Slices of the 5G network [18] may be constructed in random areas. The region of the networks that are sliced is a crucial consideration when implementing network slicing. The main parts of the 5G network are the RAN and the Core Network. User devices are linked to the central node of the network through RAN. The RAN is provided by connected BSs and controllers. The core network is connected to other networks through the Internet. A network node is the segment of the 5G network where network slicing can be applied.

Flexible network slicing allows slices to be constructed on top of a shared infrastructure, each delivering customized network services to meet the demands of the use case.

3.4 Software Defined Networks

Sectioning the connection to implement the concept of Network slicing is realized through SDN architecture, as shown in Figure 3.

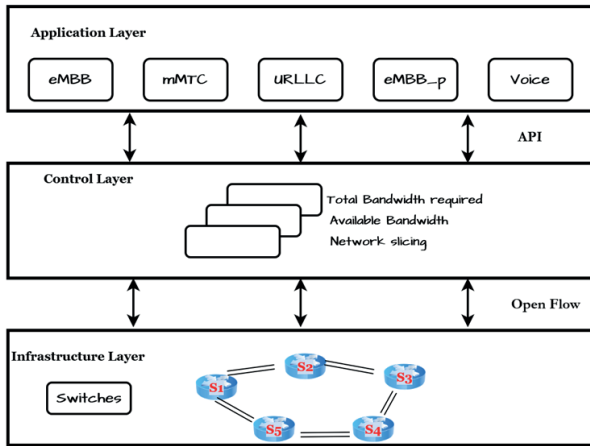


Figure 3: SDN Architecture

It is used to regulate traffic flows via the Application Programming Interface (APIs) of a central control plane. Using the application layer, the control plane configures Bandwidth resources so as to meet the requirements of individual clients.

On the basis of their service category, the infrastructure layer of SDN takes responsibility for data forwarding and rule processing needed for the control plane. It also governs essential tasks required for networking. The network slice controller maps and monitors the inter-layer functionality of the network. In the proposed research, the developed methodology is emulated using Python 3.7. It uses various packages, namely: `simpy`, `matplotlib`, `KDTree`, `shapely`, `ski learn`, `random`, `Kiwi Solver`, `numpy`, `pillow`, `pyarsing`, `random color`, and `python-dateutil`, to create the SDN architecture. `YAML` (Aint Markup Language) is used for reading input configuration. The operations of the clients are asynchronous as they use discrete event simulation. `Matplotlib` is used for data visualization. It is accomplished through a 2D plot. `KDTree` is used to determine the nearest-neighbor lookup. `Shapely` is used for the manipulation and analysis of planar geometric objects. The various classes of services used in this research are eMBB, mMTC, URLLC, and voice.

4 Results and discussion

4.1 Simulation parameters

In this research, the proposed system is constructed using the network slicing notion of services offered. Two

distinct cases are analyzed. The simulation parameters considered are represented in Table 2.

Table 2: 5G Simulation Parameters

S. No	Parameters with Notations	Value
1.	ϵI (Serving Class)	5
2.	ϕj (Base Station)	20
3.	δj (Serving Capacity)	6 G bit/s (Payload: 5 G bit/s)
4.	α (Total number of Clients)	100
5.	$\beta \epsilon I$ (Total Bandwidth)	120 G bit/s
6.	$\beta 5G$ (Bandwidth available in the Base Station)	40 G bit/s
7.	βSDN (Bandwidth offered through Network Slicing)	20 G bit/s
8.	$\alpha 1$ -No. of active Clients scenario 1 $\alpha 2$ -No. of active Clients scenario 2	96 97
9.	$\phi 1$ -No. of BS Scenario 1 $\phi 2$ -No. of BS Scenario 2	10 15

4.2 Simulation Scenarios

The simulation scenario is shown in Figure 4. This scenario is created using the Python IDE, and the number of clients considered is 100.

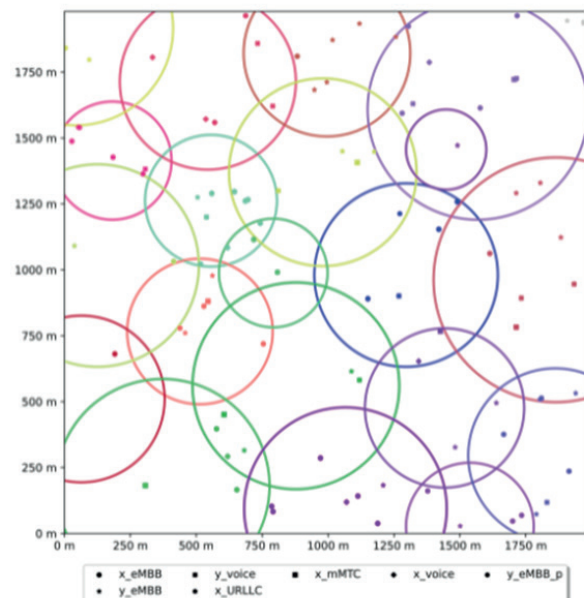


Figure 4: Simulation Scenario for network slicing

4.3 Performance Analysis

In the proposed research, two scenarios with the adoption of network slicing are considered.

To understand the impact of network slicing when the 5G network is accommodated with all five kinds of services, distributed in different ratios, it needs to be investigated. Several scenarios meeting the above requirement have been constructed and investigated. The results obtained from two scenarios with a wide range of variations with respect to the types of services are presented here.

4.3.1 Scenario 1

The performance evaluation of scenario 1 with and without network slicing is shown in Figure 5. Out of the total 100 clients considered, 96 were linked to five different services and assumed to be active clients. The service distribution among the clients is: 70 eMBB clients, 10 mMTC clients, 10 URLLC clients, 2 voice clients, and 4 eMBB_p clients. From Table 1, 47.31 G bit/s is found to be the total bandwidth requirement of these 96 Clients. In this scenario, 10 BSs are required to provide the above bandwidth requirement. Each BS can serve up to 5 G bit/s. Thus, the total offered bandwidth is 50 G bit/s (5 x 10). The required additional bandwidth is provided by network slicing techniques. According to the simulation findings, it is observed that the associated BS offers 35.789 G bit/s while the Network Slicing offers 11.521 G bit/s.

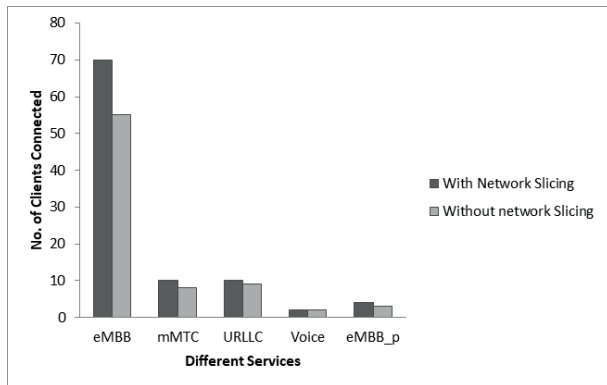


Figure 5: Clients Connected ratio for Scenario 1

The network slice for eMBB_p is shown in Figure 6. BS 1, BS 5, BS 7, and BS 10 have eMBB_p services with a bandwidth of 10 G bit/s. In such a scenario, a single BS cannot provide the needed bandwidth; network slicing is used to obtain the bandwidth available from the nearby BS. The additional bandwidth of 5.521 G bit/s required by BS 1 is sliced between BS 2 and BS 3. Each slice is assumed to have 1 G bit/s. Consequently, BS2 provides 4 slices, while BS3 provides 2 Slices to BS 1. In a similar manner, the allocation of slices is regulated based on the requirements of the BS.

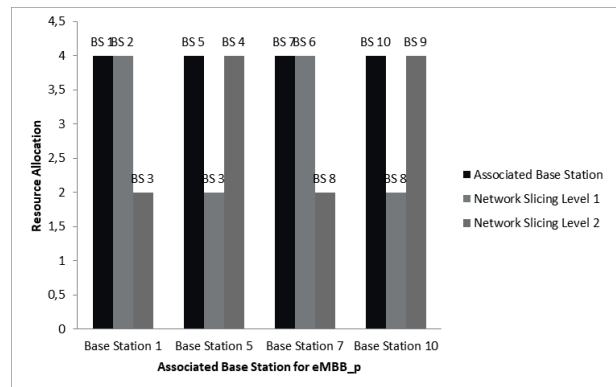


Figure 6: Network slicing for eMBB_p in Scenario 1

4.3.2 Scenario 2

The performance evaluation of scenario 2 with and without network slicing is shown in Figure 7. Out of the total 100 clients considered, 97 were linked to five different services and assumed to be active clients. The service distribution among the clients is: 52 eMBB clients, 21 mMTC clients, 15 URLLC clients, 24 voice clients, and 5 eMBB_p clients. From Table 1, 47.31 G bit/s is found to be the total bandwidth requirement of these 97 Clients. In this scenario, 15 BSs are required to provide the above bandwidth requirement. Each BS can serve up to 5 G bit/s. Thus, the total offered bandwidth is 75 G bit/s. However, G bit/s is required to maintain QoS. The required additional bandwidth is provided by network slicing techniques. According to the simulation findings, it is observed that the associated BS offers 34.372 G bit/s while the Network Slicing offers 21.453 G bit/s.

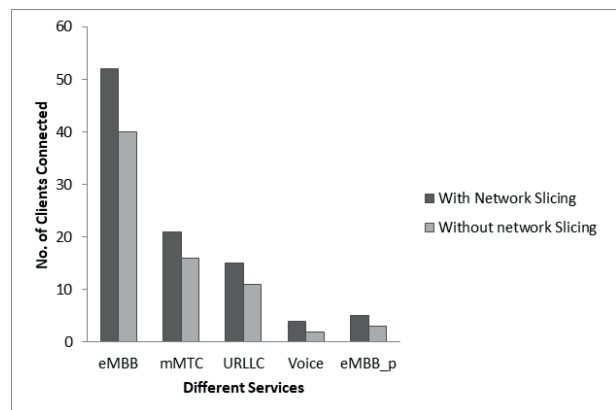


Figure 7: Clients Connected ratio for Scenario 2

The network slice for eMBB_p is shown in Figure 8. BS 1, BS 4, BS 7, BS 12, and BS 14 have eMBB_p services with a bandwidth of 10 G bit/s. In such a scenario, a single BS cannot provide the needed bandwidth; network slicing is used to obtain the bandwidth available from the nearby BS. The additional bandwidth of 5.332 G bit/s required by BS 4 is sliced between BS 5 and BS 6. Each slice is assumed to have 1 G bit/s. Consequently, BS2 provides 3 slices, while BS2 provides 3 Slices to BS 4.

In a similar manner, the allocation of slices is regulated based on the requirements of the BS.

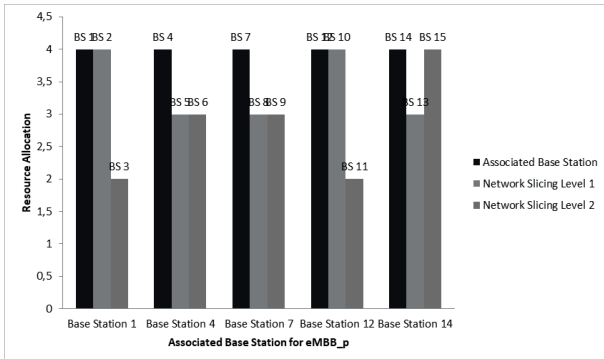


Figure 8: Network slicing for eMBB_p in Scenario 2

4.3.3 Bandwidth utilization

The consumption of bandwidth in both scenarios is depicted in Figures 9 and 10. In Scenario 1, the utilization of bandwidth without network slicing is 76%, while it is 24% in scenario 2 to achieve application-specific QoS by the clients.

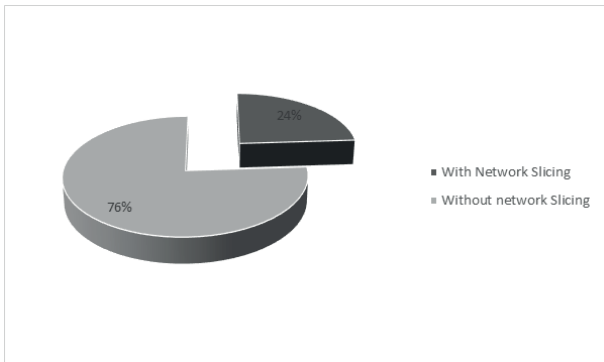


Figure 9: Bandwidth Utilization for Scenario 1

In Scenario 2, the utilization of bandwidth without network slicing is 62%. Through network slicing, 38% of the bandwidth has been utilized to serve the clients and achieve QoS.

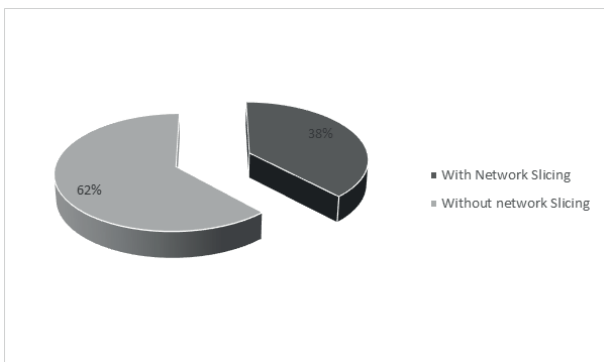


Figure 10: Bandwidth Utilization for Scenario 2

5 Conclusions

In this research, the concept of network slicing is investigated. SDN-based architecture-based network slicing in the 5G network is being developed. 5G clients of five different types of services, namely: eMBB, mMTC, URLLC, voice, and eMBB_p, are considered. The ratio of them is varied, and two different scenarios are constructed. Their performance with and without network slicing is analyzed. The developed SDN architecture is simulated using Python 3.7. From the simulation results, it is found that scenarios 1 and 2 achieve bandwidth utilization of 24% and 38%, respectively. Further, through network slicing, the clients of differential services are assured of the required bandwidth. The developed work is assumed to have static clients; hence, the BS associated with it and network slices will remain constant. However, to understand a more realistic scenario, the clients can be subjected to mobility, which is considered the future of work.

6 Acknowledgments

The authors are grateful to the Centre for Internet of Things (CIoT), Madras Institute of Technology Campus, Anna University, for providing the resources needed to complete the research.

7 Conflict of interest

The authors declare that there is no conflict of interest.

8 References

1. Maman, M., Calvanese-Strinati, E., Dinh, L.N. et al. Beyond private 5G networks: applications, architectures, operator models and technological enablers. *J Wireless Com Network* 2021, 195 (2021). <https://doi.org/10.1186/s13638-021-02067-2>
2. P. Ramesh and P. T. V. Bhuvaneswari, "Non Orthogonal Multiple Access Requirements for 5G and Its Myths," 2022 IEEE Delhi Section Conference (DELCON), 2022, pp. 1-6, <https://doi.org/10.1109/DELCON54057.2022.9752790>.
3. H. Zhang, N. Liu, X. Chu, K. Long, A. -H. Aghvami and V. C. M. Leung, "Network Slicing Based 5G and Future Mobile Networks: Mobility, Resource Management, and Challenges," in *IEEE Communications Magazine*, vol. 55, no. 8, pp. 138-145, Aug. 2017.

4. M. Kokilavani, R. Siddharth, S. Mohamed Riyaz, P. Ramesh, S. Ezhilarasi and P. T. V. Bhuvanewari, "Downlink Performance Analysis of 5G PD-NOMA System," 2022 IEEE Global Conference on Computing, Power and Communication Technologies (GlobConPT), 2022, pp. 1-6, <https://doi.org/10.1109/GlobConPT57482.2022.9938331>.
5. M. Richart, J. Baliosian, J. Serrat and J. Gorricho, "Resource Slicing in Virtual Wireless Networks: A Survey," IEEE Transactions on Network and Service Management, Vol. 13, No. 3, pp. 462-476, Sep. 2016.
6. Alcardo Alex Barakabitze, Arslan Ahmad, Rashid Mijumbi, Andrew Hines, "5G network slicing using SDN and NFV: A survey of taxonomy, architectures and future challenges," Computer Networks, Elsevier, Vol. 167, 2020.
7. Gupta and R. K. Jha, "A Survey of 5G Network: Architecture and Emerging Technologies," in IEEE Access, vol. 3, pp. 1206-1232, 2015, <https://doi.org/10.1109/ACCESS.2015.2461602>.
8. T.Mlinar, B.Batagelj, "Open RAN-What does an open architecture of the radio access network enable enable," Elektrotehniski Vestnik, Vol.90, pp. 265-271, 2023.
9. Samsung, "Network Slicing," technical white paper, April 2020.
10. A heavy reading white paper for Affirmed Networks,"4G – 5G ready network slicing white paper".
11. Khushneet Kour and Kausar Ali, "A Review Paper on 5G Wireless Networks," International Journal of Engineering Research & Technology (IJERT), ISSN: 2278-0181, 2016.
12. L. U. Khan, I. Yaqoob, N. H. Tran, Z. Han and C. S. Hong, "Network Slicing: Recent Advances, Taxonomy, Requirements, and Open Research Challenges," in IEEE Access, vol. 8, pp. 36009-36028, 2020, <https://doi.org/10.1109/ACCESS.2020.2975072>.
13. K. Katsalis, N. Nikaein, E. Schiller, A. Ksentini and T. Braun, "Network Slices toward 5G Communications: Slicing the LTE Network," in IEEE Communications Magazine, vol. 55, no. 8, pp. 146-154, Aug. 2017, <https://doi.org/10.1109/MCOM.2017.1600936>.
14. Subedi, P., Alsadoon, A., Prasad, P.W.C. et al. Network slicing: a next generation 5G perspective. J Wireless Com Network 2021, 102 (2021).
15. X. Foukas, G. Patounas, A. Elmokashfi and M. K. Marina, "Network Slicing in 5G: Survey and Challenges," in IEEE Communications Magazine, vol. 55, no. 5, pp. 94-100, May 2017, <https://doi.org/10.1109/MCOM.2017.1600951>.
16. S.Jayalakshmi, N.Sangeetha, S.Swetha, Dr. T. Ananth Kumar, "Network Slicing and Performance Analysis Of 5g Networks Based On Priority", International Journal of Scientific & Technology research, vol. 8, issue 11, November 2019.
17. GSMA, "An Introduction to network slicing", 2017.
18. P. Ramesh and P. T. V. Bhuvanewari, "Performance Analysis of NOMA under Power Control Mechanism," 2021 Innovations in Power and Advanced Computing Technologies (i-PACT), 2021, pp. 1-5, <https://doi.org/10.1109/i-PACT52855.2021.9696636>.



Copyright © 2024 by the Authors. This is an open access article distributed under the Creative Commons Attribution (CC BY) License (<https://creativecommons.org/licenses/by/4.0/>), which permits unrestricted use, distribution, and reproduction in any medium, provided the original work is properly cited.

Arrived: 05. 09. 2023

Accepted: 24. 04. 2024

A Novel Dual-Mode Dual Type Hysteresis Schmitt Trigger and its Applications using Single Differential Voltage Current Conveyor Transconductance Amplifier

Harika Pamu, Puli Kishore Kumar, Kiran Kumar Gurrala

Department of Electronics and Communication Engineering, National Institute of Technology Andhra Pradesh, Tadepalligudem, Andhra Pradesh, India

Abstract: This paper introduces a novel Schmitt trigger circuit that can operate in two modes: voltage and trans-impedance mode using a sole Differential Voltage Current Conveyor Transconductance Amplifier (DVCCTA) within the same topology with external grounded resistors. The suggested designs enable dual-type hysteresis (clockwise (CW) and counter-clockwise (CCW)) simultaneously within the same circuit topology. Additionally, the proposed design includes the unique ability to control threshold levels through the transconductance parameter (g_m) of DVCCTA via a grounded resistor. The proposed Schmitt trigger is extended for the application of a square/triangular waveform generator and pulse width modulator to illustrate the utility of the given Schmitt trigger circuit. All the proposed designs are appropriate for IC integration due to the available grounded passive attributes. Moreover, the design comes with a feature of independent control of oscillation frequency using a grounded capacitor eliminates the highest level of parasitics, and lessens the circuit's sensitivity to noise immunity. The maximum absolute deviation of output amplitude is observed to be less than 0.062 % (for CW mode) and 0.038 % (for CCW mode), while for threshold voltages, it is below 0.528 % (CW) and 0.321 % (CCW), respectively against for temperature variations of 0- 100 °C. Realization of DVCCTA uses 20 MOS transistors with 0.18 μm TSMC CMOS technology parameter, which is used to authenticate the workableness of the proposed design through PSPICE. Additionally, Monte Carlo simulations, temperature-dependent variations, non-ideal analysis, schematic layout with post-layout simulation, and also experimental results using ICAD844 are presented to validate the proposed design. The simulated responses correlate with the theoretical prediction.

Keywords: Schmitt trigger, DVCCTA, dual-type hysteresis, Square/triangular waveform generator, electronically tunable, pulse width modulation (PWM)

Nov dvonivojski histerezni Schmittov prožilec in njegova uporaba z uporabo enojnega diferencialnega napetostnega tokovnega transkonduktančnega ojačevalnika

Izveček: Članek predstavlja novo vezje Schmittovega prožilca, ki lahko deluje v dveh načinih: v napetostnem in transimpedančnem načinu z uporabo enega diferencialnega napetostno tokovnega transkonduktančnega ojačevalnika (DVCCTA) znotraj iste topologije z zunanjimi ozemljenimi upori. Predlagane zasnove omogočajo dvojno histerezo (v smeri urinega kazalca (CW) in v nasprotni smeri urinega kazalca (CCW)) znotraj iste topologije vezja. Poleg tega predlagana zasnova vključuje edinstveno zmožnost nadzora pragovnih ravni preko parametra transkonduktance (g_m) DVCCTA z ozemljenim uporom. Predlagani Schmittov prožilec je razširjen za uporabo generatorja pravokotnih/trikotnih valovnih oblik in modulatorja širine impulzov, da se ponazori uporabnost danega vezja Schmittovega prožilca. Vse predlagane zasnove so zaradi razpoložljivih ozemljenih pasivnih gradnikov primerne za integracijo v IC. Poleg tega je zasnova opremljena s funkcijo neodvisnega nadzora frekvence nihanja z uporabo ozemljenega kondenzatorja, ki odpravlja raven parazitnih signalov in zmanjšuje občutljivost vezja na šum. Največje absolutno odstopanje izhodne amplitude je

How to cite:

H. Pamu et al., "A Novel Dual-Mode Dual Type Hysteresis Schmitt Trigger and its Applications using Single Differential Voltage Current Conveyor Transconductance Amplifier", Inf. Midem-J. Microelectron. Electron. Compon. Mater., Vol. 54, No. 2(2024), pp. 131–147

manjše od 0,062 % (v načinu CW) in 0,038 % (v načinu CCW), medtem ko je za mejne napetosti pod 0,528 % (CW) oziroma 0,321 % (CCW) pri temperaturnih spremembah od 0 do 100 °C. Realizacija DVCCTA uporablja 20 tranzistorjev MOS s tehnologijo CMOS TSMC 0,18 μm , ki se uporablja za preverjanje uporabnosti predlagane zasnove s PSPICE. Poleg tega so za potrditev predlagane zasnove predstavljene simulacije Monte Carlo, temperaturno odvisne variacije, neidealna analiza, shematska postavitev s simulacijo po postavitvi in tudi eksperimentalni rezultati z uporabo ICAD844. Simulirani odzivi se ujemajo s teoretičnimi napovedmi.

Ključne besede: Schmittov prožilec, DVCCTA, dvojna histereza, generator pravokotnih/trikotnih valov, elektronska nastavljenost, pulzno-širinska modulacija (PWM)

* Corresponding Author's e-mail: harikapamu.sclr@nitandhra.ac.in

1 Introduction

The present world of the electronics environment is augmented with filters, rectifiers, amplifiers, A/D converters, comparators, oscillators, and many more signal-processing circuits. Among these, a comparator circuit accompanied by positive feedback is named as Schmitt trigger [1] which plays a vital role in the province of both analog and digital. Schmitt trigger circuit transforms any irregularly formed input signal into a square waveform and is commonly used to improve the circuit's immunity to noise. In addition, it is an essential block used in distinct applications like a square waveform generator [2], versatile modulator [3], relaxation oscillators [4], function generators [5], monostable multivibrator [6], pulse width modulator [7], switching power supplies [8], etc.

Initially, a Schmitt trigger has been presented with a traditional Op-Amp and passive components [1] but suffers from a finite gain-bandwidth product, high power dissipation, low slew rate, lesser dynamic range, etc. [9]. As an attractive strategy to waver the constraints of conventional Op-Amp [10], Various current mode analog active blocks (AAB) have been reported in the literature namely (second generation current conveyor) CCII [11], (third generation current conveyor) CCIII [12], (operational transconductance amplifier) OTA [13], (operational trans resistance amplifier) OTRA [14], (differential voltage current conveyor) DVCC [15], (dual X current conveyors) DXCCII [16], (dual X current conveyor transconductance amplifier) DXCCTA [17] and many more. An active block namely DVCCTA is chosen from the above-cited current mode active blocks due to its prominent feature of electronically adjustable transconductance in comparison to Op-Amp. The usage of DVCCTA can be extended to the field of signal processing for designing various circuits namely analog filters [18] - [19], oscillators [20] - [21], simulator [22] and so many.

Numerous Schmitt trigger circuit implementations using distinct current mode AAB are reported in the literature [23-43]. Some circuits based on CCII are discussed

in [23]–[27], but these implementations require either a higher number of active or passive elements and are incapable of providing a dual-type hysteresis mode of operation. In [27], a non-inverting Schmitt trigger is demonstrated, employing only a CCII and three passive components. This circuit functions as a zero-voltage comparator and is capable of adjusting the threshold voltage levels. However, a Schmitt trigger with independent current control of amplitude and frequency using two OTA's along with two grounded resistors is cited in [28]. In [29], current input dual hysteresis mode OTRA Schmitt trigger has been delivered with the possibility of changing its type of hysteresis with the help of a switch. Although, it uses a floating resistor which is not an advisable feature for IC Implementation. The improvement in circuit design using DXCCTA is also given in [30] without any passive elements. This configuration reduces the influence of temperature variation on output amplitude levels. However, it doesn't offer the capability to demonstrate both CW and CCW hysteresis. Another prominent configuration with DVCC and two grounded resistors [31] has the capability to adjust the hysteresis by varying the values of a resistor. Two more designs with (differential difference current conveyor) DDCC and (current differencing transconductance amplifier) CDTA with two resistors are demonstrated in [32] and [33] but unable to exhibit dual type hysteresis. Aside from the above mentioned circuits, dual-type hysteresis, independent and electronic control of threshold and amplitude levels are viable through (current follower differential input transconductance amplifier) CFDITA [34], (current differencing buffered amplifier) CDBA [35], (current controlled current differencing transconductance amplifier) CCCDTA [36] based designs but circuit in [34] is unable to give both type of hysteresis simultaneously. The Schmitt trigger circuit mentioned in [37] that uses a single (voltage differencing transconductance amplifier) VDTA and one resistor is unable to exhibit dual type hysteresis, but it does have the ability to independently control the output amplitude levels. Circuit cited in [38] uses single (second generation current controlled current conveyor) CCCII, a capacitor and two resistors for generating

a square waveform with the maximum power consumption of 600 μ W but unable to exhibit dual-type hysteresis. Square wave generators based on (second generation differential current conveyor) DCII, two resistors and a sole capacitor in [39] and [40] have the advantage of reducing noise caused by parasitics through the use of a grounded capacitor. A recent proposal introduces a Waveform generator utilizing commercially available ICs along with (extra X second generation current conveyor) EXCCII prototype [42] and five passive components. The circuit benefits from the capability of independently controlling oscillation frequency via passive elements. Also, an attempt was made to design a Schmitt trigger with (second generation voltage conveyor) VCII [43] comprising of two active blocks and five resistors exhibiting an average power consumption of 328 μ W and 365 μ W for transitions at non-inverting and inverting mode outputs, respective-

ly. Table. 1 demonstrates a comparative study with the earlier described Schmitt trigger circuits, which is summarized in the comparison section in great detail.

Henceforth, this paper presents a Schmitt trigger with dual-type hysteresis within the same topology available in two modes specifically voltage and trans-impedance mode with less number of grounded passive components and its application as a square/triangular wave generator and pulse width modulator. The design works with an AAB named DVCCTA for the Schmitt trigger operation. Additionally, the proposed design comes with an attractive feature of availability of both modes (voltage and transimpedance) within the same circuit topology. Notably, the topologies provide the benefit of independent control of threshold levels and oscillation frequency. The simulation results using PSPICE along with CMOS based DVCCTA and the ex-

Table. 1: Comparison of the proposed Schmitt trigger topology with the existing literature

Ref	Type and no. of AAB used	No. of passive component used	All grounded passive elements	Dual Type Hysteresis	Transistor type or IC	Dual type Hysteresis within the same topology	Operational frequency (HZ)	Independent control of threshold levels	Independent control of oscillation frequency	Insensitive to Temperature	Experimental Results Shown
[23]	CCII – 2	4 R	No	No	0.6 μ m CMOS, IC AD844	No	10K	No	No	No	Yes
[24]	CCII – 1	3R	No	No	0.35 μ m AMS CMOS	No	-	No	No	NA	No
[25]	CCII – 2	6R, 1C	No	No	0.35 μ m AMS CMOS	No	-	No	Yes	No	No
[27]	CCII – 1	3R	No	No	0.35 μ m AMS CMOS	No	-	No	Yes	NA	Yes
[28]	OTA – 2	2R	Yes	No	LM13600N	No	-	Yes	Yes	No	No
[29]	OTRA – 1	1R	No	Yes	IC AD844	Yes	100K	No	No	NA	No
[30]	DXCCTA-1	No	NA	No	TSMC 180 nm CMOS	No	5M	Yes	No	Yes	No
[31]	DVCC – 1	2R	Yes	No	0.25 μ m CMOS, OPA660	No	400K	Yes	Yes	NA	Yes
[32]	DDCC- 1	2R	No	No	0.5 μ m MIETTEC	No	NA	No	No	No	No
[33]	CDTA- 1	2R	No	No	0.18 μ m CMOS	No	410K	No	Yes	No	Yes
[34]	CFDITA – 1	1R	Yes	Yes	IC AD844, LM13700	Yes	5K	Yes	No	NA	Yes
[35]	CDBA- 1	3R	No	Yes	IC AD844	No	50	No	No	Yes	Yes
[36]	CCCDTA – 1	No	NA	Yes	IC AD844, ALA400 BJT and LM13600 N	Yes	100K	Yes	Yes	No	Yes
[37]	VDTA – 1	1R	Yes	No	BJT ALA400	No	1K	Yes	No	NA	No
[38]	CCCII – 1	2R,1C	Yes	No	45 nm BSIM CMOS, ICAD844	No	4M	No	No	No	Yes
[39]	DCII – 1	2R,1C	No	No	gpdk 180 nm	No	3.8M	No	Yes	No	Yes
[40]	DCII – 1	2R,1C	No	No	gpdk 180 nm	No	NA	No	Yes	No	Yes
[41]	VDTA-R – 1	2R	Yes	Yes	0.25 μ m TSMC	Yes	NA	Yes	Yes	No	No
[42]	EXCCII – 1	3R	No	No	IC AD844	No	19.2K	No	Yes	No	Yes
[43]	VCII – 2	5R	No	Yes	0.18 μ m CMOS	Yes	NA	Yes	No	NA	No
Proposed Design	DVCCTA – 1	1R	Yes	Yes	0.18 μ m TSMC and IC AD844	Yes	5M	Yes	Yes	Yes	Yes

perimental verification using IC AD844 are examined to authenticate the theory. Also, the feasibility of Schmitt trigger for different type of input voltages, temperature dependence, non-ideal analysis, and Monte Carlo analysis is illustrated.

The remaining sections of the paper are structured as follows. Section 2 discusses the circuit representation and analysis of the basic building block DVCCTA and the proposed dual mode (voltage mode and transimpedance mode) Schmitt trigger. Section 3 focuses on how the proposed circuits can be extended for the application as a square/triangular waveform generator and pulse width modulator. Section 4 gives the effect of non-ideal current and voltage transfer gains on the performance of the proposed Schmitt trigger. Section 5 presents the functional verification of the proposed circuits through simulation results. Moving on to Section 6 gives further validation of the proposed designs through experimental analysis, followed by a comparative analysis with existing models in Section 7. Finally, Section 8 addresses the conclusion.

2 Circuit representation and analysis

2.1 DVCCTA

The DVCCTA, a simple active block was first given in [44], which is combination of DVCC [15] resides at input phase and OTA [13] remains at output phase, which is a combination of DVCC [15] resides at input phase and OTA [13] remains at the output phase. Fig. 1 depicts the hierarchical block, while Fig. 2 presents the commercially available IC AD844 implementation and CMOS implementation [49] of DVCCTA, respectively.

The following characteristic equations define the analog block as:

$$I_{Y1} = I_{Y2} = 0; V_X = V_{Y1} - V_{Y2}; I_{Z+} = I_X; I_{O-} = -g_m V_{Z+} \quad (1)$$

where g_m can be defined as the transconductance of DVCCTA. This parameter is electronically tunable via an external biasing current (I_B) which is described by the following equation (2).

$$g_m = \sqrt{\mu_n c_{ox} \left(\frac{W}{L}\right)_{11,12}} I_B \quad (2)$$

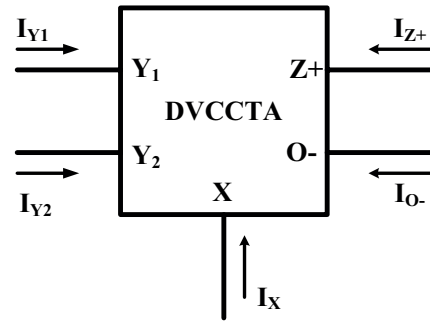


Figure 1: Hierarchical block of DVCCTA

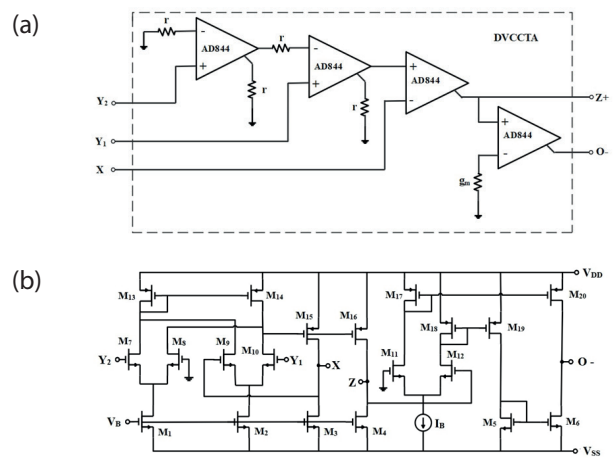


Figure 2: DVCCTA (a) IC AD844 implementation (b) CMOS implementation

2.2 DVCCTA based voltage mode Schmitt trigger

The proposed voltage mode Schmitt trigger uses a single DVCCTA and only one grounded external resistor with inputs V_{in1} , V_{in2} and output V_{out} is shown in Fig. 3. With the selection of input, we can avail dual type hysteresis operation likely CW and CCW which are clearly disclosed below.

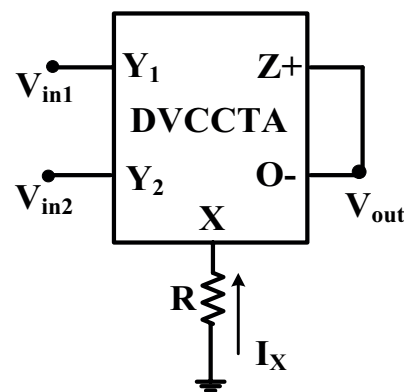


Figure 3: Proposed voltage mode Schmitt trigger circuit

2.2.1. CCW Schmitt trigger

Here, to enable the CCW mode of operation, the input V_{in1} is driven through the Y_1 terminal of DVCCTA by keeping Y_2 terminal grounded. The output V_{out} is taken across the O- terminal of DVCCTA. Depending upon the input signal level, square wave output either saturates at (positive saturation level) $+V_{sat}$ or at the (negative saturation level) $-V_{sat}$.

From the routine analysis of the design,

$$I_X = \frac{V_X}{R} \tag{3}$$

Adopting the port relation of DVCCTA ($V_X = V_{Y1} - V_{Y2}$), and $V_{Y2} = 0; V_X = V_{Y1} = V_{in1}$. Equation (2) can be written as

$$I_X = \frac{V_{in1}}{R} \tag{4}$$

Here the currents passing through the terminals Z+ and O- are equal ($I_{Z+} = I_{O-}$) because of the short circuit connection. From the port relations ($I_{Z+} = I_X; I_{O-} = -g_m V_{Z+}$) given in equation (1), we can write as follows

$$I_X = -g_m V_{Z+} \tag{5}$$

Using equations (4 and 5) and from circuit $V_{Z+} = V_{out}$, the input voltage (V_{in1}) is expressed as:

$$V_{in1} = (-g_m V_{Z+}) R = -V_{out} \left(\frac{R}{R_m} \right) \tag{6}$$

where g_m is taken as $1/R_m$.

The upper threshold voltage (V_{TH}) is calculated with the assumption that the initial value of output is at $-V_{sat}$.

$$V_{TH} = +V_{sat} \left(\frac{R}{R_m} \right) \tag{7}$$

As V_{in1} increases from zero, V_{out} remains at $-V_{sat}$ until V_{in1} reaches V_{TH} . When it satisfies the condition ($V_{in1} > V_{TH}$), output level changes from $-V_{sat}$ to $+V_{sat}$. Subsequently, the low threshold voltage (V_{TL}) is given as

$$V_{TL} = -V_{sat} \left(\frac{R}{R_m} \right) \tag{8}$$

The output level ($+V_{sat}$) is maintained for the input $V_{in1} > V_{TL}$.

The corresponding value for the hysteresis is calculated as

$$V_{HYS} = V_{TH} - V_{TL} \tag{9}$$

2.2.2 CW Schmitt trigger

This mode of operation is supervised by V_{in2} through the inverting Y_2 terminal of DVCCTA since V_{in1} is grounded. The O terminal comprises for output V_{out} , as shown in Fig. 3. The circuit analysis is as same as CCW mode and the voltage V_{in2} can be expressed as

$$V_{in2} = V_{out} \left(\frac{R}{R_m} \right) \tag{10}$$

The hysteresis operation is observed to be adverse of CCW operation with the assumption that the initial value of output is at $+V_{sat}$. Therefore, V_{TH} and V_{TL} are observed to be same as in equations (7) and (8) respectively.

2.3 Transimpedance mode Schmitt trigger

The transimpedance mode Schmitt trigger circuit is realized using the same topology as in Fig. 3 by adding an external grounded resistors at Y terminals with a current input (I_{in}). Dual-type hysteresis is available within same topology with the selection of input as either I_{in1} or I_{in2} within the same design and is clearly disclosed in this section.

CCW transimpedance mode Schmitt trigger is enabled through the input I_{in1} at Y_1 terminal of DVCCTA when Y_2 terminal is grounded and the output V_{out} is observed at O terminal of DVCCTA which is shown in Fig. 4. The principle operation is same as the voltage mode Schmitt trigger by considering the initial value of output is at $-V_{sat}$. By considering the ideal characteristics from equation (1), the simple calculations can be obtained below:

The input current (I_{in1}) is expressed as

$$I_{in1} = -V_{out} \left(\frac{R}{R_1} \right) g_m \tag{11}$$

Where g_m is taken as $1/R_m$.

The upper and lower threshold currents (I_{TH}, I_{TL}) can be expressed to be

$$I_{TH} = +V_{sat} \left(\frac{R}{R_1 R_m} \right) \tag{12}$$

$$I_{TL} = -V_{sat} \left(\frac{R}{R_1 R_m} \right) \quad (13)$$

CW transimpedance mode Schmitt trigger is enabled through the input I_{in2} at Y_2 terminal of DVCCTA while the other input terminal Y_1 is grounded. The O terminal incorporates the output V_{out} where the operation of hysteresis is observed to be adverse of CCW type. Likewise, the input current (I_{in2}) is given in equation (14) and I_{TH} , I_{TL} are the same as of CW type since the initial assumption of output is settled at $+V_{sat}$.

$$I_{in2} = V_{out} \left(\frac{R}{R_2} \right) g_m \quad (14)$$

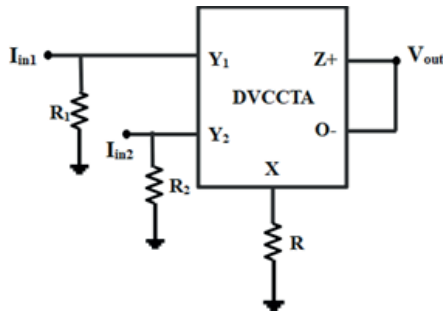


Figure 4: Transimpedance mode Schmitt trigger circuit

3 Applications

3.1 Waveform generator

To illustrate the usefulness and practical application of the introduced work, Schmitt trigger-based square/triangular waveform generator is depicted in Fig. 5. The waveform generator incorporates the proposed voltage mode Schmitt trigger design along with an integrator using CFOA, a resistor, and a capacitor. The proposed scheme adopts only grounded passive components. Mostly, the grounded capacitor reduces the level of parasitics during fabrication. It is expanded to the waveform generator as a square wave at V_{out1} and triangular wave at V_{out2} output terminals, that can be mathematically characterized as:

$$V_{out1} = V_{square} = -\frac{R_m}{R} V_{in} \quad (15)$$

$$V_{out2} = V_{triangular} = -\frac{V_{square}}{R_0 S C_0} \quad (16)$$

The Schmitt trigger either saturates at $+V_{sat}$ or $-V_{sat}$. Initially, by assuming that the output V_{square} is at $+V_{sat}$, this voltage makes the capacitor C_0 to charge with current I_Z initiating V_{out2} to linearly increase with a positive slope until V_{TH} . Subsequently, the square waveform output changes to $-V_{sat}$ which makes the capacitor C_0 to discharge V_{out2} decreases linearly with a negative slope until it reaches V_{TL} of V_{out1} . The succeeding relationships provide charging and discharging intervals of the capacitor.

$$\frac{V_{TH} - V_{TL}}{T_1} = \frac{I_Z}{C_0} \quad (17)$$

$$\frac{V_{TL} - V_{TH}}{T_2 - T_1} = -\frac{I_Z}{C_0} \quad (18)$$

Whereas V_{TH} and V_{TL} are originated from Equations (7) and (8), the time period ($T = T_1 + T_2$) of the waveform and subsequently the frequency can be computed as

$$T = 6RC_0 \quad (19)$$

$$f = \frac{1}{6RC_0} \quad (20)$$

3.2 Pulse Width Modulator (PWM)

PWM scheme is extensively used in voltage regulation, communication systems, power conversion control circuits, ADC, Instrumentation systems, and digital audio [45]–[48]. In this technique, the pulse width of the modulated output is altered according to the voltage level of input modulating signal. PWM output signal can be more oftenly produced by comparing a modulating signal and a carrier waveform like triangular or sawtooth waveform. The proposed design is adequately suited for designing the Pulse Width Modulator (PWM) displayed in Fig. 6 consists of single DVCCTA which acts as a comparator and a resistor. The modulating signal V_{in} is given through input terminal Y_2 , the voltage across Y_1 terminal Y_c operate as a carrier signal and the required PWM output V_{out} is taken over the Z terminal of DVCCTA. The feasible saturation levels of V_{out} are $+V_{sat}$ and $-V_{sat}$. As the V_c increases from zero and moves towards the input modulating signal V_{in} , the PWM output voltage abides at $-V_{sat}$ and once V_c reaches V_{in} and satisfies the condition ($V_c > V_{in}$), V_{out} changes its state from $-V_{sat}$ to $+V_{sat}$. It is maintained until the carrier voltage decreases and satisfies the condition of ($V_c < V_{in}$), then the PWM output state changes to $-V_{sat}$.

Employing the terminal characteristics given in equation (1), the mathematical analysis is given below

$$V_X = V_C - V_{in} \quad (21)$$

The current through X terminal can be written as

$$I_X = \frac{V_C - V_{in}}{R} \quad (22)$$

As we know that, from equation (1), $I_{Z+} = I_X$ and $I_{O-} = -g_m V_{Z+}$. Therefore, by equating I_{Z+} and I_{O-} because of the short circuit connection.

$$I_X = -g_m V_{out} = \frac{-V_{out}}{R_m} \quad (23)$$

Where g_m is considered as $1/R_m$.

By making use of equations (22, 23), the output voltage V_{out} of PWM is determined as

$$V_{out} = \frac{R_m}{R} (V_{in} - V_C) \quad (24)$$

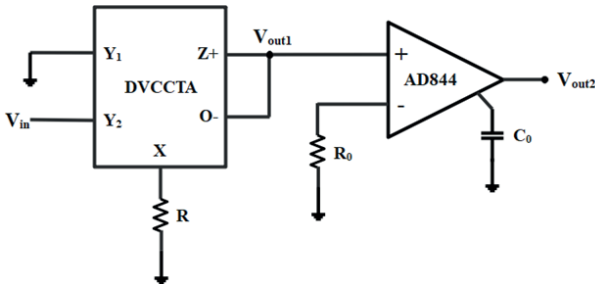


Figure 5: Square/triangular wave generator

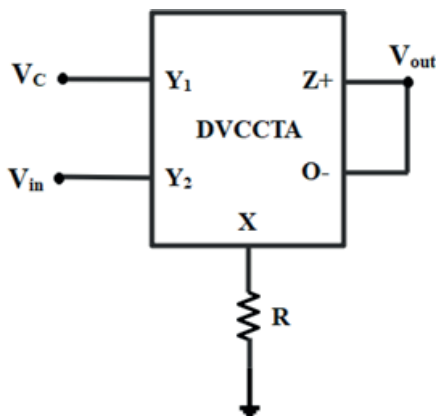


Figure 6: Proposed Pulse Width Modulator (PWM)

4 Non ideal analysis

To determine the non-ideal response of the proposed Schmitt Trigger, including various non-idealities of DVCCTA. The tracking errors in the matrix below show the deviation from the ideal DVCCTA's properties.

$$\begin{bmatrix} I_{Y1} \\ I_{Y2} \\ V_X \\ I_Z \\ I_{O\pm} \end{bmatrix} = \begin{bmatrix} 0 & 0 & 0 & 0 \\ 0 & 0 & 0 & 0 \\ 0 & \beta_1 & -\beta_2 & 0 \\ \alpha & 0 & 0 & 0 \\ 0 & 0 & 0 & \pm\gamma g_m \end{bmatrix} \begin{bmatrix} I_X \\ V_{Y1} \\ V_{Y2} \\ V_Z \end{bmatrix} \quad (25)$$

Here, α represents the current transfer gain, while β_1 and β_2 denote the voltage transfer gains, and γ represents the transconductance gain. The numerical relation between α and the current tracking error (ξ_i), as well as β and the voltage tracking error (ξ_v), can be expressed as:

$$\alpha = 1 - \xi_i, \beta_1 = 1 - \xi_{v1} \text{ and } \beta_2 = 1 - \xi_{v2} \quad (26)$$

Further analysis of the proposed circuits using equation (25) is as follows:

For CCW operation, By taking, $V_X = \beta_1 V_{in1}$ and $V_{Y2} = 0$, equation (3) can be written as

$$I_X = \frac{\beta_1 V_{in1}}{R} \quad (27)$$

Also considering, ($I_{Z+} = \alpha I_X$; $I_{O-} = -\gamma g_m V_{Z+}$), equation (5) can be written as

$$\alpha I_X = -\gamma g_m V_{Z+} \quad (28)$$

From equations (27 & 28), the input voltage V_{in1} is expressed as

$$V_{in1} = \frac{\gamma}{\alpha \beta_1} (-g_m V_{out}) R \quad (29)$$

However, for CW mode, the circuit analysis is similar to CCW mode, and voltage V_{in2} can be expressed according to equation (10).

5 Simulation Results

The proposed voltage mode Schmitt trigger design illustrated in Fig. 3 is examined with both CMOS and IC AD844 based DVCCTA using PSPICE with $0.18 \mu\text{m}$ CMOS technology parameter from TSMC. The passive attributes are selected as $R=500 \Omega$ and $R_m=1 \text{ k}\Omega$ with 50 Hz sinusoidal input voltage of amplitude $\pm 8 \text{ V}$. Fig. 7 depicts the simulation responses of input and output characteristics for the (current feedback operational amplifier) CFOA based implementation of the proposed design. In addition, the transient response of a proposed Schmitt trigger circuit utilizing CMOS imple-

mentation is illustrated in Fig. 8. The CMOS-based DVCCTA is biased with a supply voltage of $V_{DD} = -V_{SS} = 1.4V$, $V_B = -0.4V$ and $I_b = 60 \mu A$ ($g_m = 0.9961 \text{ mS}$), with $R = 500 \Omega$. Here, g_m is calculated to according to equation (2). The aspect ratios of MOS transistor are provided in Table. 2. Besides, the input and output characteristics for the proposed transimpedance mode schmitt trigger with a 50 Hz sinusoidal current input (I_{in}) of $\pm 2 \text{ mA}$ amplitude and $R = R_1 = R_2 = 1 \text{ k}\Omega$, $R_m = 10 \text{ k}\Omega$ is shown in Fig. 9 and Fig. 10. Furthermore, to check the proposed design's workability at higher frequencies, a 5 MHz sinusoidal voltage waveform with amplitude $\pm 8 \text{ V}$ is applied to voltage mode Schmitt trigger design. Fig. 11 depicts that the amplitude levels are not distorted at higher frequencies which further confirms the capability of Schmitt trigger circuits over a wide range of frequency. The CCW Schmitt trigger exhibits a -3 dB band-

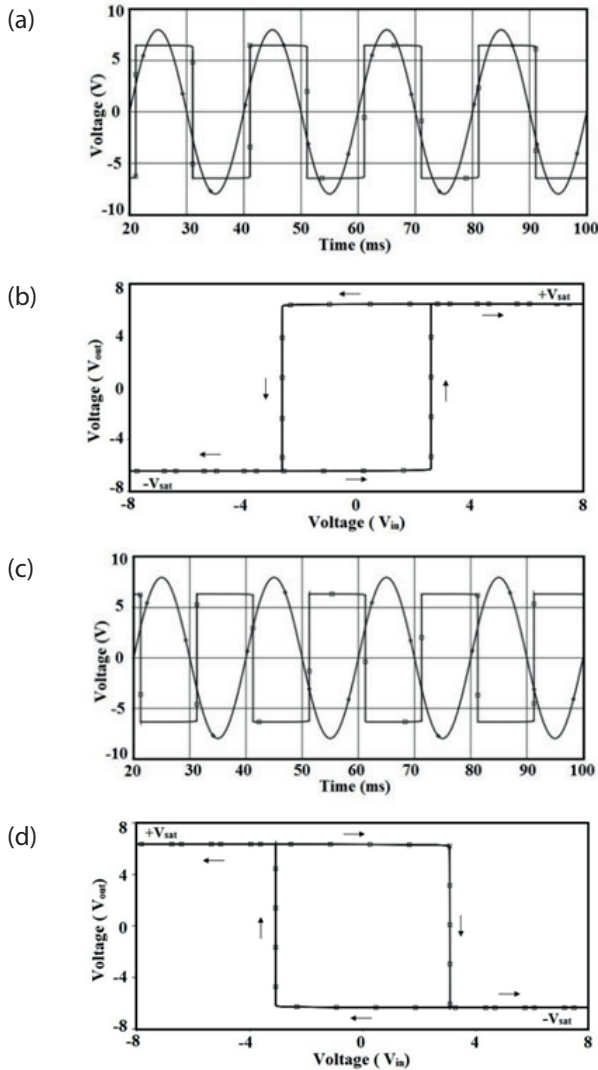


Figure 7: Simulated AD844 based DVCCTA Schmitt trigger responses (a) CCW V_{in1} and V_{out} waveform (b) CCW Hysteresis curve (c) CW V_{in1} and V_{out} waveform (d) CW Hysteresis curve

width at approximately 12.86 MHz, while the CW mode shows at around 10.82 MHz.

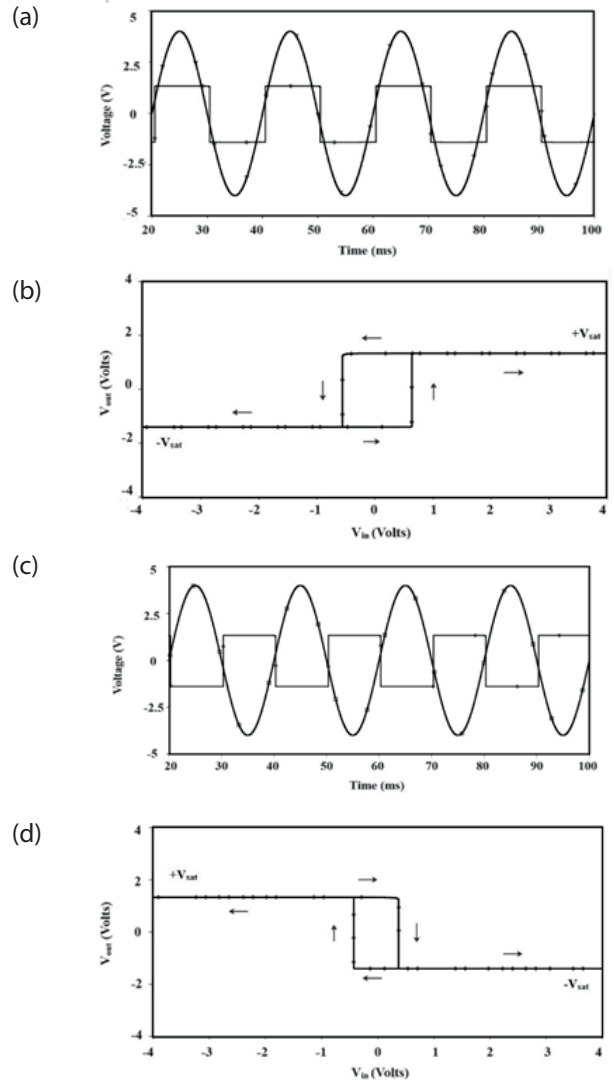


Figure 8: Simulated CMOS based DVCCTA Schmitt trigger responses (a) CCW V_{in1} and V_{out} waveform (b) CCW Hysteresis curve (c) CW V_{in1} and V_{out} waveform (d) CW Hysteresis curve

Table 2: CMOS based DVCCTA transistors dimensions

Transistors	W (in μm)	L (in μm)
$M_1 - M_6$	4.32	0.36
$M_7 - M_{10}$	1.44	0.36
$M_{11} - M_{16}$	21.6	0.36
$M_{17} - M_{20}$	7.2	0.36

In order to evaluate the temperature stability of the proposed Schmitt triggers, the output (V_{out}) is observed at different temperature values specifically (27 °C, 50 °C, 75 °C and 100 °C). As a result, as shown in Fig.12, it is observed that the amplitude and the threshold levels of a square wave are not adversely affected due

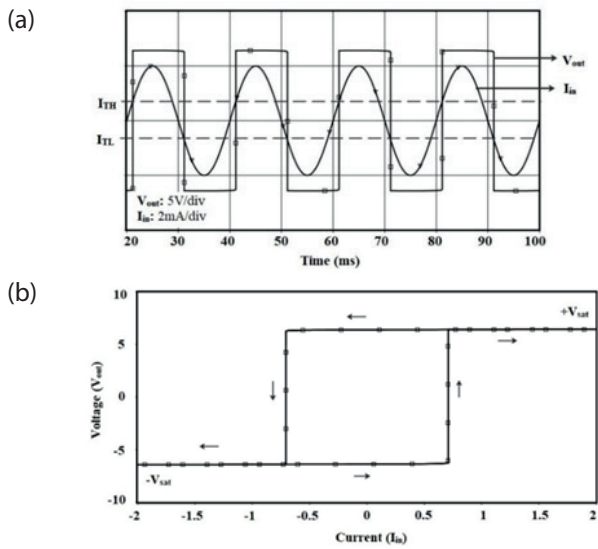


Figure 9: Simulated AD844 based Transimpedance mode CCW operation (a) I_{in1} and V_{out} waveform (b) Hysteresis curve

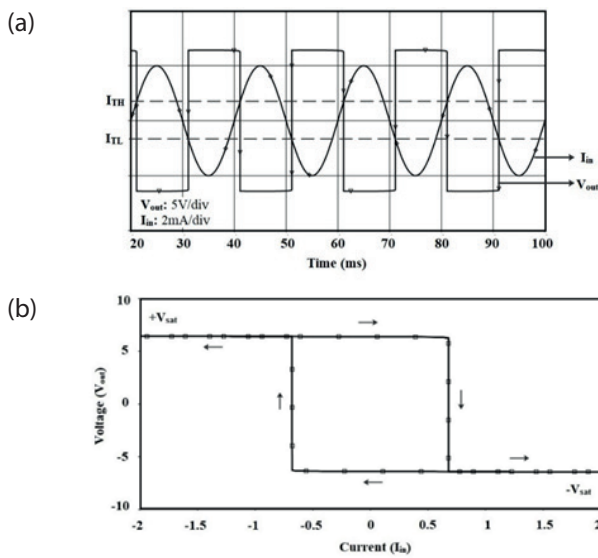


Figure 10: Simulated AD844 based Transimpedance mode CW operation (a) I_{in2} and V_{out} waveform (b) Hysteresis curve

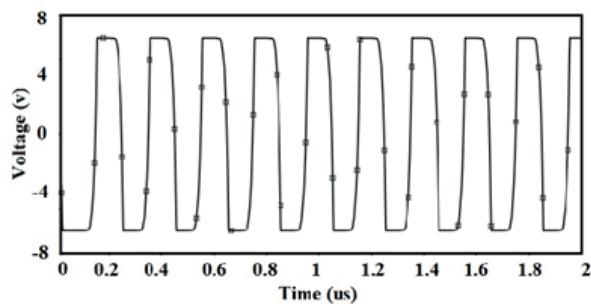


Figure 11: V_{out} at 5 MHz

to temperature variations. To further quantify the extent of deviation in amplitude and threshold levels, it is checked for temperature variations of 0- 100 °C. Notably, the findings from Figs. 13 and 14 reveals that the maximum absolute deviation in output amplitude remains below 0.0625 % (for CW Schmitt trigger) and 0.0381 % (for CCW Schmitt trigger), while for threshold voltages magnitude is less than 0.5 % (for both CW and CCW modes). Moreover, the stability of output amplitude levels through Monte Carlo analysis at temperatures 27, 50, 75 and 100 °C, considering over 200 random points with a 5 % tolerance in resistor values is depicted in Fig. 15 and 16. The measured mean and standard deviation values for output amplitude are as follows: (1.3119, 0.00058), (1.3128, 0.00059), (1.3142, 0.00061), (1.3159, 0.00063) for CCW mode, while for CW mode are taken as (1.2798, 0.0022), (1.2508, 0.0029), (1.2508, 0.003), (1.2515, 0.003), respectively which further demonstrates the circuit’s resilience to temperature variations.

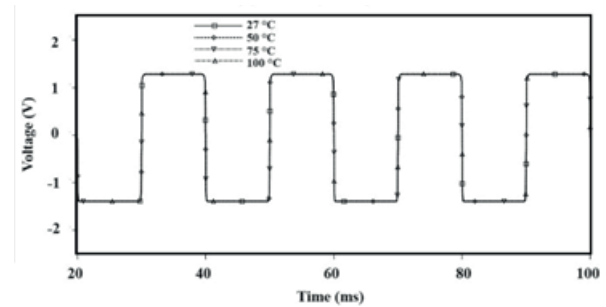


Figure 12: Variation in V_{out} for different temperature values (27 °C, 50 °C, 75 °C, 100 °C)

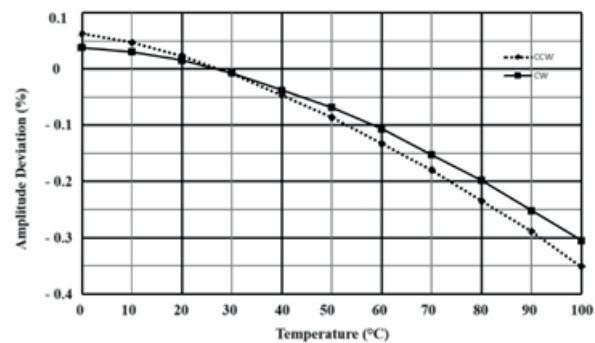


Figure 13: Deviation in output amplitude levels of the proposed voltage mode Schmitt trigger against temperature variations

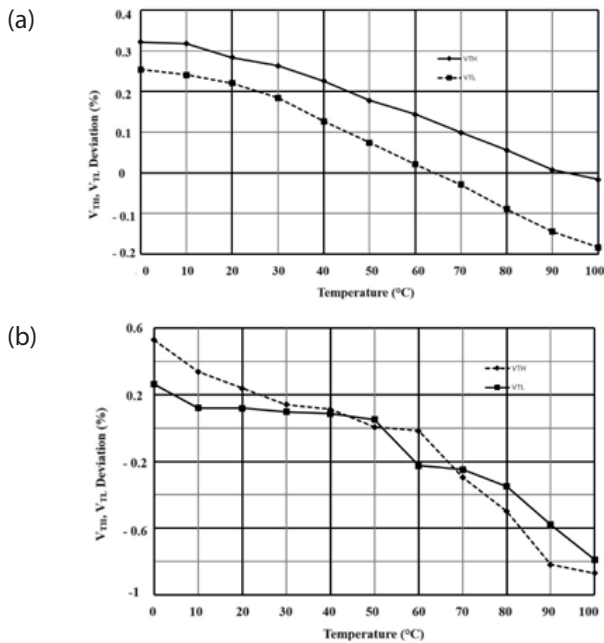


Figure 14: Deviation in Threshold voltage levels against temperature variations (a) CCW Schmitt trigger (b) CW Schmitt trigger

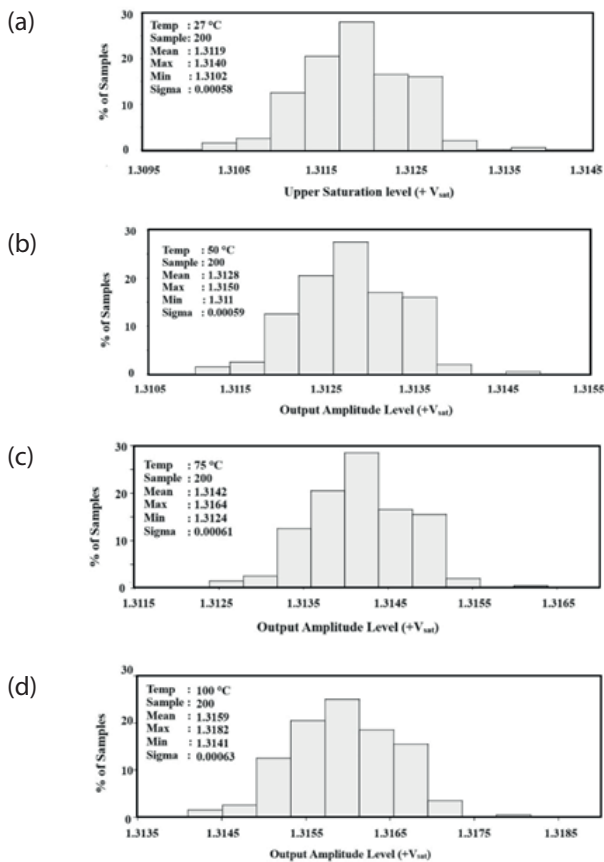


Figure 15: Monte Carlo simulations of output amplitude for CCW mode Schmitt Trigger (a) 27 °C (b) 50 °C (c) 75 °C (d) 100 °C.

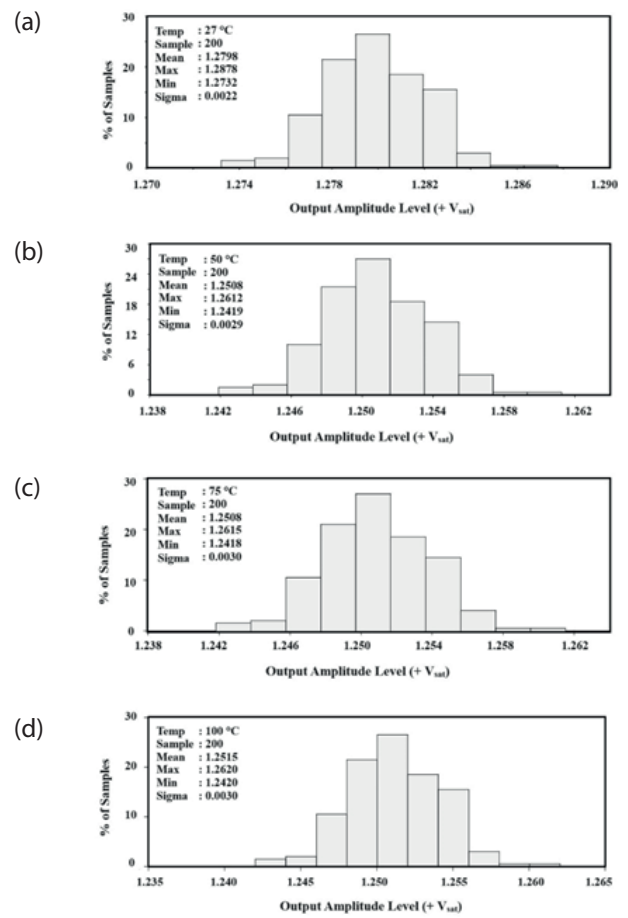


Figure 16: Monte Carlo simulations of output amplitude for CW mode Schmitt Trigger (a) 27 °C (b) 50 °C (c) 75 °C (d) 100 °C.

Fig. 17 depicts the simulated responses of both the CW and CCW structures of the proposed voltage mode circuit for a triangular wave input with a frequency of 50

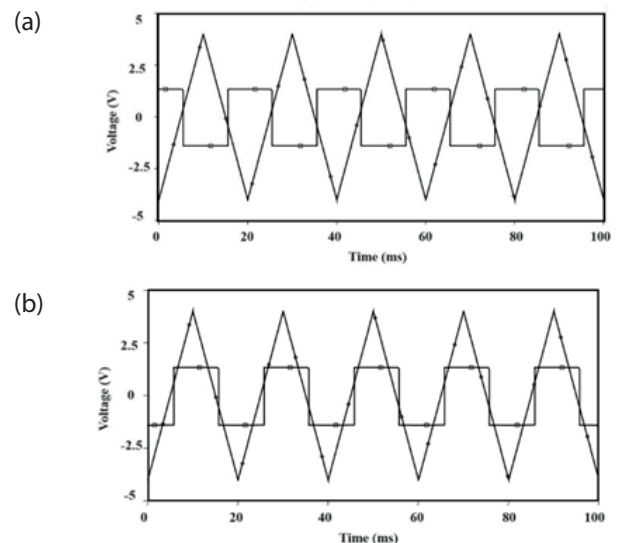


Figure 17: Triangular wave V_{in} and V_{out} waveform (a) CW (b) CCW

Hz and an amplitude of ± 4 V. Subsequently, the output is observed to be a square wave, regardless of the input waveform type. This key characteristic demonstrates the versatility and feasibility of the circuit, as it can effectively process and convert different types of input signals.

From Figs. 18 and 19, it is observed that the threshold levels of the proposed ICAD844 based voltage and transimpedance mode Schmitt trigger circuits can be electronically controlled by adjusting the transconductance parameter (g_m) through the relationship $g_m = \frac{1}{R_m}$, without disturbing the output's amplitude. Figs. 20 and 21 interprets the illustration for theoretical and simulated threshold voltages against R_m variation of dual type voltage mode Schmitt trigger, respectively. It is observed that the simulated threshold values concur well with the theoretical anticipation. Overall, the analysis highlights the controllability of threshold levels through R_m .

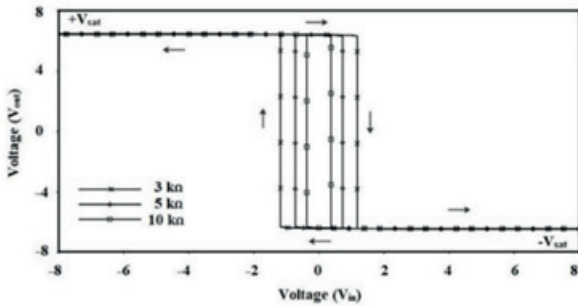


Figure 18: DC transfer characteristic of voltage mode Schmitt trigger for different R_m

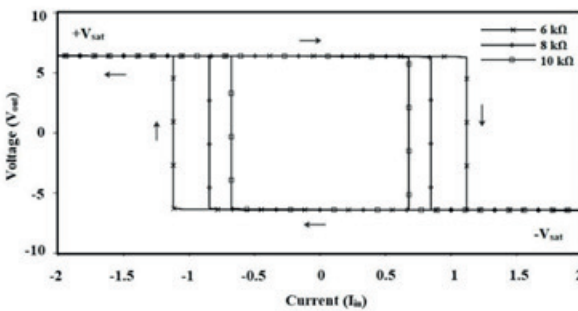


Figure 19: DC transfer characteristic of transimpedance mode Schmitt trigger for different R_m

Fig. 22 exhibits the theoretical simulation results for variation in operating frequency against C_0 . The results reveal that the operating frequency can be independently adjusted by C_0 , wherein, Equation (20) helps for the theoretical analysis. By maintaining the values of other external components R at 865Ω and $R_m = R_0 = 1 \text{ k}\Omega$, the capacitance can be varied from $3.8535 \mu\text{F}$ to 0.1376 nF . This variation in the capacitor enables a frequency range of 50 Hz to 1.4 MHz , further demonstrat-

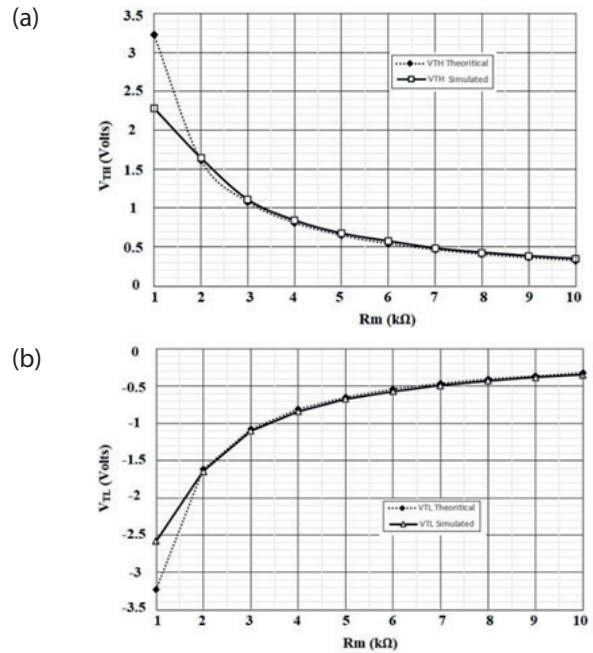


Figure 20: CW Schmitt Trigger threshold voltage levels against R_m (a) V_{TH} (b) V_{TL}

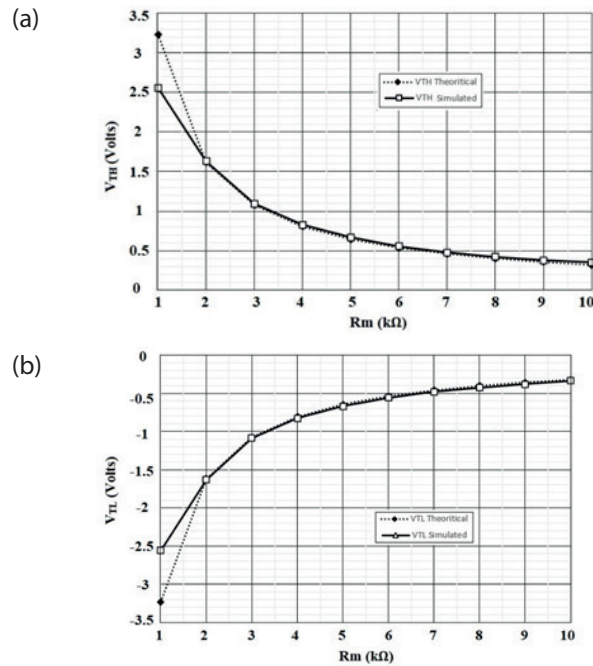


Figure 21: CCW Schmitt Trigger threshold voltage levels against R_m (a) V_{TH} (b) V_{TL}

ing the linearity of the proposed circuit over a broad frequency range. The output transient response of application part of Schmitt trigger as the square/triangular waveform generator at different input frequencies is pictured in Fig. 23 using CMOS based implementation of DVCCTA. The component values are elected as $C_0 = 3.8535 \mu\text{F}$, $R = 865 \Omega$ and $R_m = R_0 = 1 \text{ k}\Omega$. The summarized key properties of proposed designs is given in Table. 3.

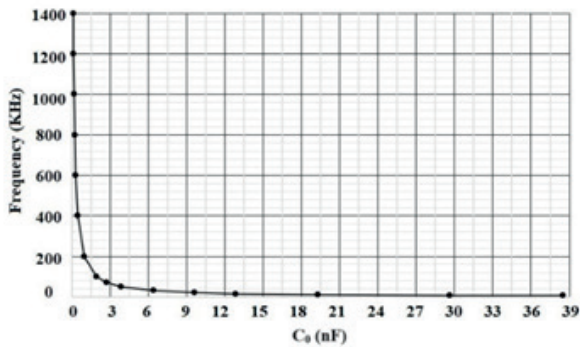


Figure 22: The operating frequency variations with changes in C_o

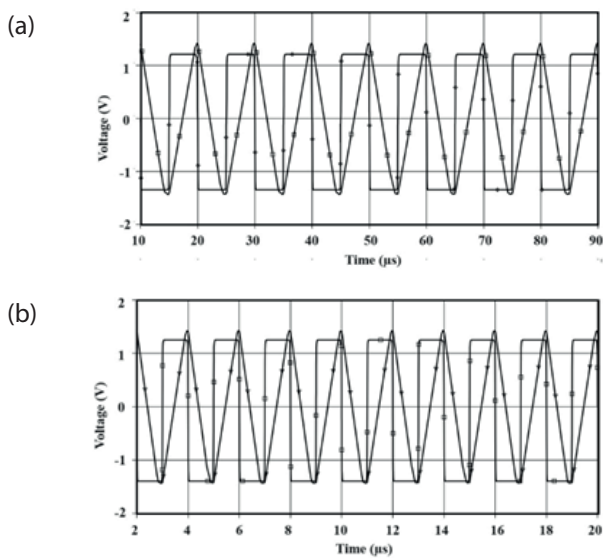


Figure 23: Transient response of Square/triangular waveform generator for input frequency (a) 100 KHz (b) 500 KHz

Finally, the circuit in Fig. 6 is used for the generation of PWM, and its output is depicted in Fig. 24 with the selection of $R = 1 \text{ k}\Omega$ and $R_m = 10 \text{ k}\Omega$ and input voltage V_{in} of 50 Hz sinusoidal with an amplitude of $8V_{pp}$. The carrier waveform V_c of about 500 Hz is set to be a triangular wave. It is obvious that the pulse width of V_{out} is modulated according to the input-modulating sinusoidal signal.

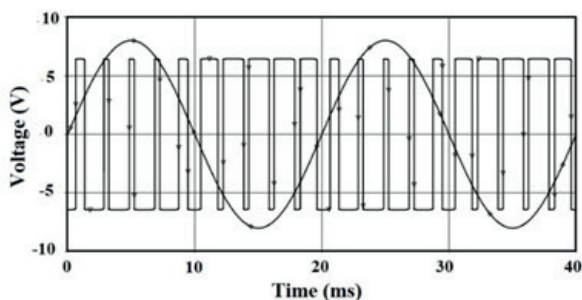


Figure 24: Simulated PWM output

6 Experimental results

The experimental demonstration of the considered design is done by means of IC AD844 implementation of DVCCTA. The supply voltages V_{DD} and V_{SS} for IC AD844 are given as $\pm 15V$ along with $r = 20 \text{ k}\Omega$. The proposed voltage mode CW Schmitt trigger at different frequencies gives the transient response as displayed in Fig. 25. Correspondingly, component values for practical verification are selected as $R = 1 \text{ k}\Omega$ and $R_m = 10$

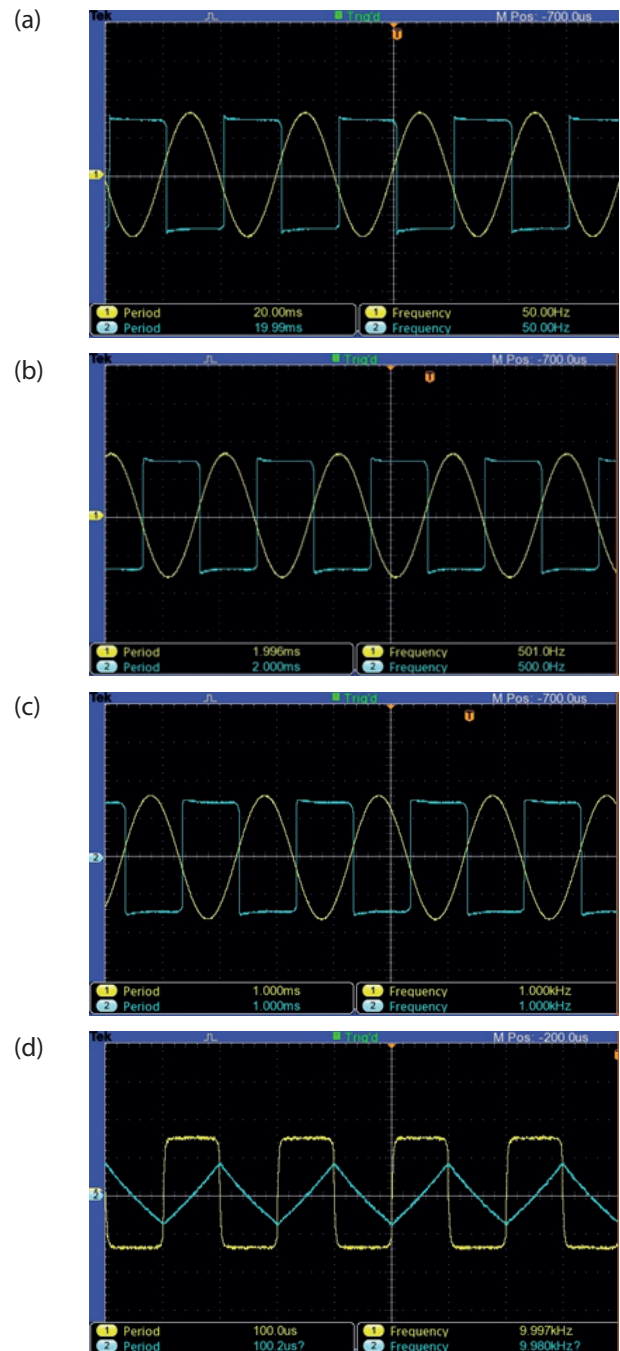


Figure 25: Experimentally observed V_{in} and V_{out} at frequencies (a) 50 Hz (b) 500 Hz (c) 1 kHz (d) 10 kHz

Table 3: Summary of key attributes of proposed Schmitt trigger circuits.

Parameters	CW Schmitt Trigger		CCW Schmitt Trigger	
No. of AAB (DVCCTA) used	1			
No. of passive elements used	1 (grounded)			
Maximum operational frequency	10.82 MHz		12.86 MHz	
Output amplitude levels deviation for temperature variations (0-100 °C)	Less than 0.0381 %		Less than 0.0625 %	
Threshold levels deviation for temperature variations (0-100 °C)	Less than 0.5282 %		Less than 0.3216 %	
Temperatures	Mean	Standard deviation	Mean	Standard deviation
27 °C	1.2798	0.0022	1.3119	0.00058
50 °C	1.2508	0.0029	1.3128	0.00059
75 °C	1.2508	0.003	1.3142	0.00061
100 °C	1.2515	0.003	1.3159	0.00063
Power supply	1.4 V			
Power Consumption	3.51 mW			
Application (Square/triangular wave generator) – Frequency range for capacitance variation (3.8535 μ F to 0.1376 nF)	50 Hz – 1.4 MHz			

k Ω with a sinusoidal input voltage of amplitude $V_{in} = \pm 8$ V. Accordingly, Fig. 26 delivers the output waveform for square/triangular wave generator with the selection of $R_m = R_o = R = 1$ k Ω and the variation of C_o as 3.33 μ F, 0.33 μ F, 0.11 μ F, 0.01 μ F for different frequencies of 50 Hz, 500 Hz, 1 kHz, 10 kHz respectively.

Moreover, Fig. 27 demonstrates the experimental output for PWM signal in transient domain with an input

voltage V_{in} of 50 Hz, 8V_{pp} sinusoidal and V_c works as the carrier signal which is preferred to be a triangular waveform. The component values are selected as $R = 1$ K Ω and $R_m = 10$ K Ω . It is observed that the width of the modulated output signal is controlled by controlling input voltage V_{in} with respect to carrier signal voltage.

Additionally, the MOS based schematic layout of the proposed Schmitt trigger for Fig. 2 (b) has been de-

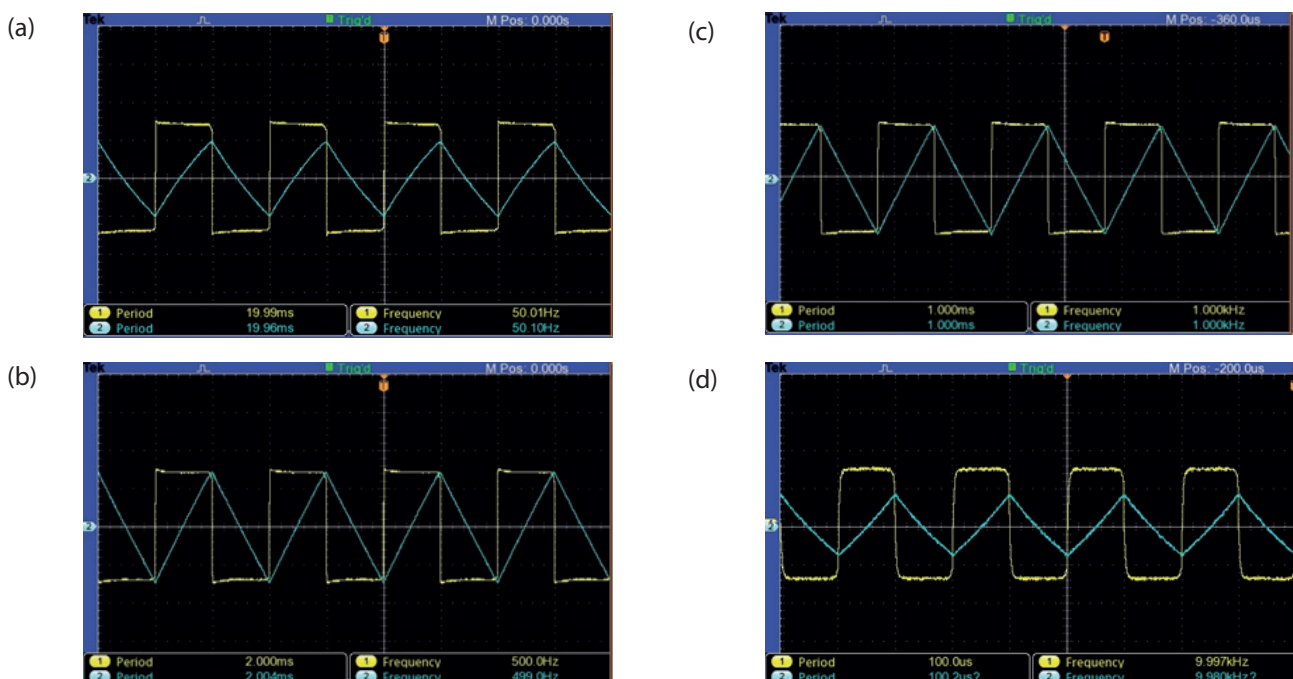


Figure 26: Experimentally observed V_{out1} and V_{out2} at frequencies (a) 50 Hz (b) 500 Hz (c) 1 kHz (d) 10 kHz

signed in virtuoso Analog Design Environment of the cadence software using 180 nm gpdk CMOS process parameters, is depicted in Fig. 28, showcasing its physical design. Furthermore, the accuracy of the layout has been assessed by conducting error checking and comparing nets between schematic and layout using specific tools, namely Design Rule Checking (DRC) and Layout Versus Schematic (LVS) verification. The pre-layout and post-layout simulations of the proposed Schmitt trigger are carried out which are given in Fig. 29.

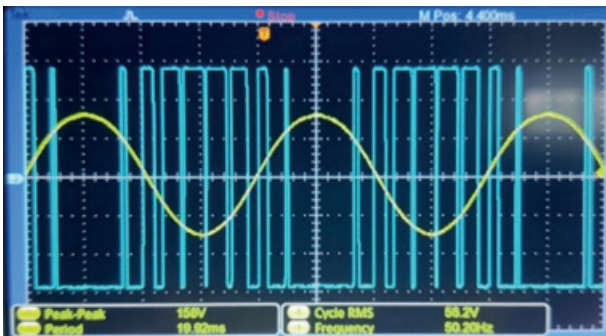


Figure 27: Modulating input V_{in} and PWM output waveform

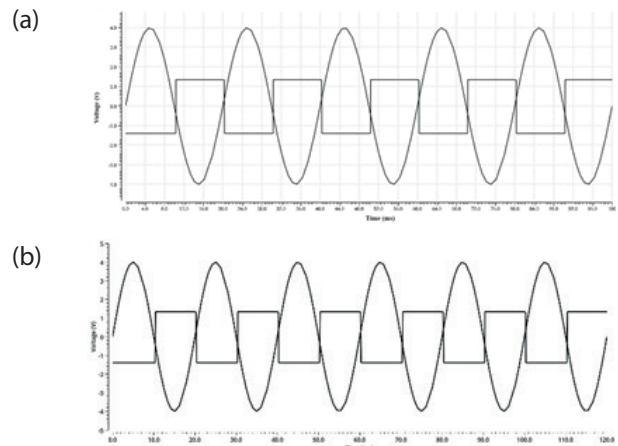


Figure 29: Input and output waveforms of proposed Schmitt trigger (a) Pre-layout simulation (b) Post-layout simulation

7 Comparison

Table. 1 provides a comprehensive comparison between the proposed topologies and the existing models found in the literature. The significance of

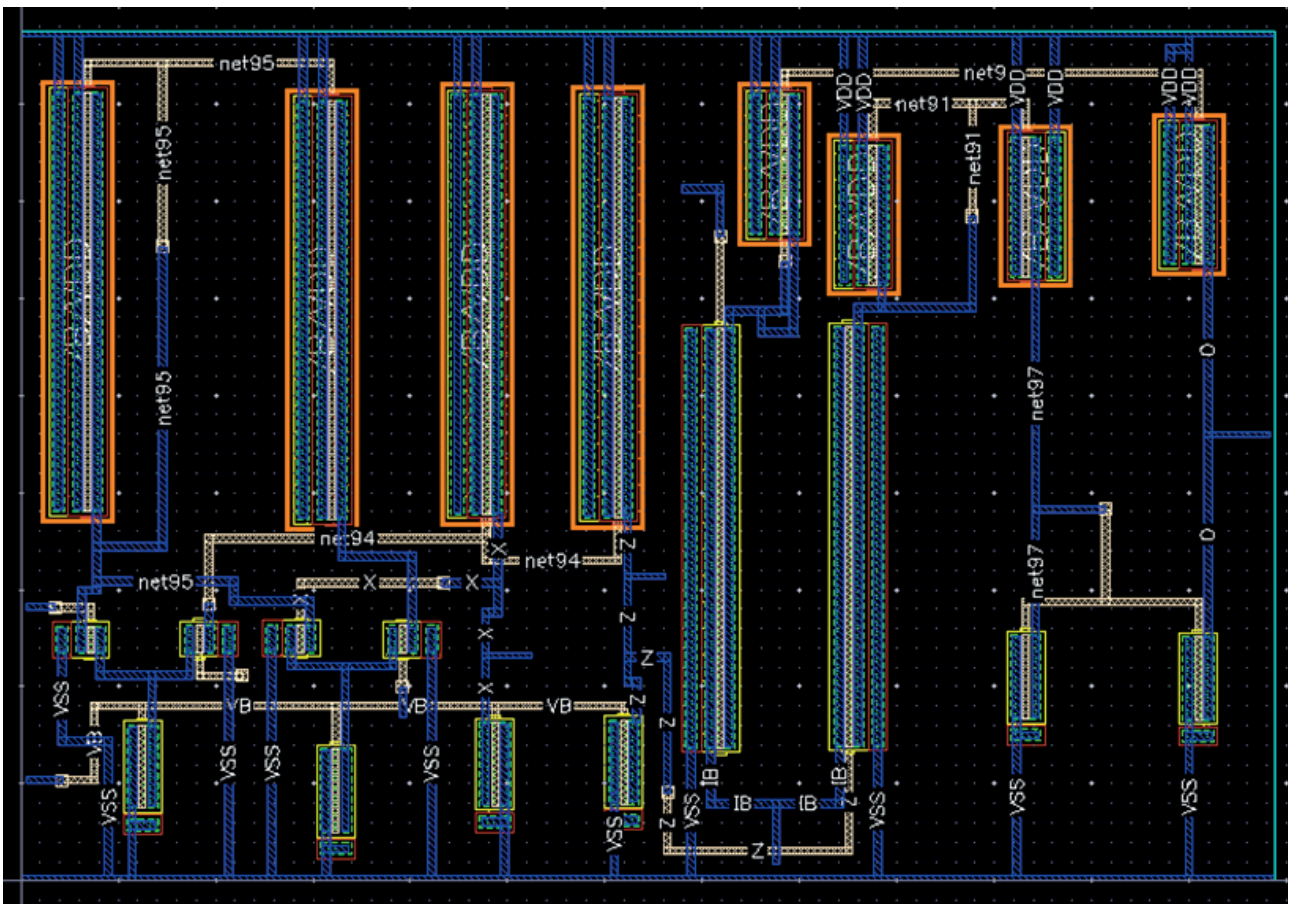


Figure 28: Schematic Layout of DVCCCTA for proposed design

the proposed designs is more precisely well summarized as:

- Use of a greater number of active elements [23, 25, 28, 43].
- Use of many passive attributes [23-25, 27-28, 31-33, 35, 38-43].
- Absence of dual-type hysteresis mode of operation [23-25, 27, 28, 30-33, 37-40, 42].
- Absence of dual type hysteresis mode of operation within the same topology [23-25, 27, 28, 30-33, 35, 37-40, 42].
- Absence of Independent control of threshold levels [23-25, 27, 29, 32-33, 35, 38-40, 42]
- Absence of Independent control of oscillation frequency [23-24, 29- 30, 32, 34-35, 37-38,43]
- Use of floating passive elements, which is difficult for IC fabrication [23-25, 27, 29, 32, 33, 35, 39-40, 42-43].

Based on the aforementioned observations, it is evident that the proposed Schmitt trigger circuits offer several notable advantages.

- Use of single AAB for realization of proposed circuits.
- Use of less number of grounded passive elements which makes it suitable for IC integration.
- Provides dual-mode Schmitt trigger circuits with single DVCCTA and grounded resistors.
- Provides both modes (CW and CCW) within the same topology.
- Extended for the application of square/triangular waveform generator and pulse width modulator.
- Provides good operational frequency.
- Independent control of Hysteresis.
- Independent control of the frequency of oscillation through a grounded capacitor.
- Insensitive to temperature.

8 Conclusion

Novel dual-mode Schmitt trigger employing a single DVCCTA and its application to square/triangular wave generator constructed using an additional CFOA, a grounded capacitor, and a grounded resistor which comprises an integrator and pulse width modulator (PWM) within the same topology is presented. The proposed design avails of two modes specifically voltage and transimpedance modes where the CW and CCW type of operation is acquired within the same topology on the basis of the selection of input. It uses only grounded passive elements and also a single CMOS-based DVCCTA, which is suitable for IC integration. Additionally, independent control of threshold levels is available. Tunability of grounded components is the prominent feature of the design where the operating

frequency can be made adjustable using a grounded capacitor and reduces the level of parasitics which sets the proposed design insensitive to noise. The highest absolute deviation of output amplitude and threshold voltage is less than 0.062 % and 0.528 %, respectively, over temperature variations ranging from 0- 100° C. The design brings dual-mode dual-type hysteresis operation, an excellent operational frequency range, and also insensitivity to temperature variations. Monte Carlo simulations, non-ideal analysis, and experimental results as well as the schematic layout with post-layout simulation results are depicted to justify the considered structure. The unique characteristics of the proposed designs make them applicable for bio-medical and other signal processing applications and can be extended for designing relaxation oscillators, versatile modulators, monostable multivibrators, etc.

9 Acknowledgments

This research is supported by Chips2startup (C2S) project sponsored by MEITY, Govt. of India and sanctioned to NIT Andhra Pradesh cluster.

10 Conflict of Interest

The authors declare that they have no conflict of interest.

Data Availability Statement: Data sharing not applicable to this article as no datasets were generated or analysed during the current study.

11 References

1. A. Sedra, K. C. Smith, "Microelectronic Circuits : 4th edition," oxford: Oxford University Press.ISBN 9780195116632.
2. S. K. Kar and S. Sen, "Tunable square-wave generator for integrated sensor applications," *IEEE Trans. Instrum. Meas.*, vol. 60, no. 10, pp. 3369–3375, 2011, <https://doi.org/10.1109/TIM.2011.2128490>.
3. P. Tuwanut, J. Koseeyaporn, and P. Wardkein, "A novel versatile modulator circuit," *AEU - Int. J. Electron. Commun.*, vol. 63, no. 5, pp. 387–397, 2009, <https://doi.org/10.1016/j.aeue.2008.02.010>.
4. T. Onomi, "Experimental Demonstration and Performance Estimation of a new Relaxation Oscillator Using a Superconducting Schmitt Trigger Inverter," *Phys. Procedia*, vol. 81, pp. 141–144, 2016, <https://doi.org/10.1016/j.phpro.2016.04.030>.

5. D. Kumar and R. Khatri, "Function Generator using Current Conveyor (CCII)," *Int. J. Comput. Appl.*, vol. 147, no. 7, pp. 1–4, 2016, <https://doi.org/10.5120/ijca2016911163>.
6. H. C. Chien and Y. K. Lo, "Design and implementation of monostable multivibrators employing differential voltage current conveyors," *Microelectronics J.*, vol. 42, no. 10, pp. 1107–1115, 2011, <https://doi.org/10.1016/j.mejo.2011.07.005>.
7. R. K. Ranjan, K. Mazumdar, R. Pal, and S. Chandra, "Generation of square and triangular wave with independently controllable frequency and amplitude using OTAs only and its application in PWM," *Analog Integr. Circuits Signal Process.*, vol. 92, no. 1, pp. 15–27, 2017, <https://doi.org/10.1007/s10470-017-0971-x>.
8. R. L. Newsom, W. C. Dillard, and R. M. Nelms, "Digital power-factor correction for a capacitor-charging power supply," *IEEE Trans. Ind. Electron.*, vol. 49, no. 5, pp. 1146–1153, 2002, <https://doi.org/10.1109/TIE.2002.803240>.
9. C. Toumazou, F. J. Lidgley, D. G. Haigh, "Analogue IC Design: the Current-Mode Approach," London: Peter Peregrinus Ltd. ISBN 0863412971.
10. D. Birolek, R. Senani, V. Biolkova, and Z. Kolka, "Active elements for analog signal processing: Classification, review, and new proposals," *Radioengineering*, vol. 17, no. 4, pp. 15–32, 2008.
11. A. Sedra, K. C. Smith, "A second generation current conveyor and its applications," *IEEE Trans. Circuit Theory*, vol. 17, no. 1, pp. 132–134, 1970.
12. A. Fabre, "Third generation current conveyor: A new helpful active element," *Electronic Letters*, vol. 31, no. 5, pp. 338–339, 1995.
13. R. V. Golhar, M. A. Gaikwad, and V. G. Nasre, "Design and Analysis of High Performance Operational Transconductance Amplifier," *International Journal of Scientific and Research Publications*, vol. 2, no. 8, pp. 1–5, 2012.
14. A. K. Singh, R. Senani, and A. Gupta, "OTRA, its implementations and applications: a state-of-the-art review," vol. 97, no. 2. Springer US, 2018.
15. H. O. Elwan, A. M. Soliman, "Novel CMOS differential voltage current conveyor and its applications," *IEEE Proceedings: Circuits, Devices and Systems*, vol. 144, no. 3, pp. 195–200, 1997.
16. A. Zeki and A. Toker, "The dual-X current conveyor (DX-CCII): A new active device for tunable continuous-time filters," *Int. J. Electron.*, vol. 89, no. 12, pp. 913–923, 2002, <https://doi.org/10.1080/0020721031000120461>.
17. A. Kumar and B. Chaturvedi, "Novel CMOS Dual-X Current Conveyor Transconductance Amplifier Realization with Current-Mode Multifunction Filter and Quadrature Oscillator," *Circuits, Syst. Signal Process.*, vol. 37, no. 6, pp. 2250–2277, 2018, <https://doi.org/10.1007/s00034-017-0680-9>.
18. N. Pandey and R. Pandey, "a First Order All Pass Filter and Its Application in a Quadrature Oscillator," vol. 12, pp. 772–777, 2012.
19. S. K. Paul and N. Pandey, "VM and CM universal filters based on single DVCCTA," *Act. Passiv. Electron. Components*, vol. 2011, 2011, <https://doi.org/10.1155/2011/929507>.
20. H. C. Chien and C. Y. Chen, "CMOS realization of single-resistance-controlled and variable frequency dual-mode sinusoidal oscillators employing a single DVCCTA with all-grounded passive components," *Microelectronics J.*, vol. 45, no. 2, pp. 226–238, 2014, <https://doi.org/10.1016/j.mejo.2013.11.007>.
21. N. Pandey and R. Pandey, "Approach for third order quadrature oscillator realisation," *IET Circuits, Devices Syst.*, vol. 9, no. 3, pp. 161–171, 2015, <https://doi.org/10.1049/iet-cds.2014.0170>.
22. W. Tangsrirat, "Floating simulator with a single DVCCTA," *Indian J. Eng. Mater. Sci.*, vol. 20, no. 2, pp. 79–86, 2013.
23. A. Srinivasulu, "A novel current conveyor based Schmitt trigger and its application as a relaxation Oscillator," *Int. J. Circuit Theory Appl.*, vol. 39, pp. 679–686, 2011.
24. S. Del Re, A. De Marcellis, G. Ferri, and V. Stornelli, "Low voltage integrated astable multivibrator based on a single CCII," *Proc. 2007 Ph.D Res. Microelectron. Electron. Conf. PRIME 2007*, no. 2, pp. 177–180, 2007, <https://doi.org/10.1109/RME.2007.4401841>.
25. A. De Marcellis, C. Di Carlo, G. Ferri, and V. Stornelli, "A CCII-based wide frequency range square waveform generator," *Int. J. Circuit Theory Appl.*, vol. 41, no. 1, 2011.
26. G. Diutaldo, G. Palumbo, and S. Pennisi, "A schmitt trigger by means of a ccii+," *Int. J. Circuit Theory Appl.*, vol. 23, no. 2, pp. 161–165, 1995, <https://doi.org/10.1002/cta.4490230207>.
27. A. De Marcellis, G. Ferri, P. Mantenuto, "A CCII-based non inverting Schmitt Trigger and its application as astable multivibrator for capacitive sensor interfacing," *Int. J. Circuit Theory Appl.*, vol. 45, pp. 1060–1076, 2016.
28. W. S. Chung, H. Kim, H. W. Cha, and H. J. Kim, "Triangular/square-wave generator with independently controllable frequency and amplitude," *IEEE Trans. Instrum. Meas.*, vol. 54, no. 1, pp. 105–109, 2005, <https://doi.org/10.1109/TIM.2004.840238>.
29. Y. K. Lo, H. C. Chein, H. J. Chiu, "Current input OTRA Schmitt trigger with dual hysteresis modes," *Int. J. Circuit Theory Appl.*, vl. 38, pp. 739–746, 2010.
30. A. Kumar and B. Chaturvedi, "Novel electronically controlled current-mode Schmitt trigger based on single active element," *AEU - Int. J. Electron.*

- Commun.*, vol. 82, pp. 160–166, 2017, <https://doi.org/10.1016/j.aeue.2017.08.007>.
31. S. Minaei and E. Yuce, "A simple Schmitt trigger circuit with grounded passive elements and its application to square/triangular wave generator," *Circuits, Syst. Signal Process.*, vol. 31, no. 3, pp. 877–888, 2012, <https://doi.org/10.1007/s00034-011-9373-y>.
 32. R. Das, K. Banerjee, A. Chakraborty, and L. Mondal, "Differential Difference Current Conveyor (DDCC) Based Schmitt Trigger Circuit & Its Application," *International Journal on Recent and Innovation Trends in computing and Communication*, Vol. 4, no. 8, pp. 69–72, 2016.
 33. K. Nagalakshmi, A. Srinivasulu, C. Ravariu, V. Vijay, and V. V. S. V. Krishna, "A Novel Simple Schmitt Trigger Circuit using CDTA and its application as a Square-Triangular Waveform Generator," *J. Mod. Technol. Eng.*, vol. 3, no. 3, pp. 205–216, 2018.
 34. A. Kumar and B. Chaturvedi, "Fully electronically controllable Schmitt trigger circuit with dual hysteresis," *Electron. Lett.*, vol. 53, no. 7, pp. 459–461, 2017, <https://doi.org/10.1049/el.2016.4770>.
 35. R. Pal, R. Pandey, N. Pandey, and R. C. Tiwari, "Single CDBA Based Voltage Mode Bistable Multivibrator and Its Applications," *Circuits Syst.*, vol. 06, no. 11, pp. 237–251, 2015, <https://doi.org/10.4236/cs.2015.611024>.
 36. P. Silapan and M. Siripruchyanun, "Fully and electronically controllable current-mode Schmitt triggers employing only single MO-CCDTA and their applications," *Analog Integr. Circuits Signal Process.*, vol. 68, no. 1, pp. 111–128, 2011, <https://doi.org/10.1007/s10470-010-9593-2>.
 37. M. Siripruchyanun, P. Saththaphol, and K. Payakkakul, "A Simple Fully Controllable Schmitt Trigger with Electronic Method Using VDTA," *Appl. Mech. Mater.*, vol. 781, no. 1, pp. 180–183, 2015, <https://doi.org/10.4028/www.scientific.net/amm.781.180>.
 38. U. Mohammad, M. Y. Yasin, R. Yousuf, and I. Anwar, "A novel square wave generator based on the translinear circuit scheme of second generation current controlled current conveyor-CCCII," *SN Appl. Sci.*, vol. 1, no. 6, 2019, <https://doi.org/10.1007/s42452-019-0608-z>.
 39. V. Vijay and A. Srinivasulu, "A novel squarewave generator using second-generation differential current conveyor," *Arab. J. Sci. Eng.*, vol. 42, no. 12, pp. 4983–4990, 2017, <https://doi.org/10.1007/s13369-017-2539-6>.
 40. V. Vijay and A. Srinivasulu, "A low power waveform generator using DCCII with grounded capacitor," *Int. J. Public Sect. Perform. Manag.*, vol. 5, no. 2, pp. 134–145, 2019, <https://doi.org/10.1504/IJPSPM.2019.099084>.
 41. P. Moonmuang, S. Unhavanich and W. Tangsrirat, "Simple current-controlled VDTA-R Schmitt trigger circuit," *In 2019 5th International Conference on Engineering, Applied Sciences and Technology (ICEAST)*, pp. 1–4, 2019, <https://doi.org/10.1109/ICEAST.2019.8802589>.
 42. A. Kumar and B. Chaturvedi, "Experimental realization of square/triangular wave generator using commercially available ICs," *J. Circuits, Syst. Comput.*, vol. 29, no. 14, 2020, <https://doi.org/10.1142/S0218126620502242>.
 43. A. Anand and R. Pandey, "A Novel Dual Output Schmitt Trigger Using Second Generation Voltage Controlled Conveyor," *2022 2nd International Conference on Intelligent Technologies (CONIT)*, Hubli, India, pp. 1–5, 2022, <https://doi.org/10.1109/CONIT55038.2022.9848259>.
 44. A. Jantakun, N. Pisutthipong, and M. Siripruchyanun, "A synthesis of temperature insensitive/electronically controllable floating simulators based on DV-CCTAs," *2009 6th Int. Conf. Electr. Eng. Comput. Telecommun. Inf. Technol. ECTI-CON 2009*, vol. 1, no. May 2014, pp. 560–563, 2009, <https://doi.org/10.1109/ECTICON.2009.5137069>.
 45. M. S. Roden, "Analog and Digital Communication Systems: 4th edition," Prentice - Hall, Englewood Cliffs, NJ, USA, pp. 176–183, 1996.
 46. D. Maksimovic and S. Cuk, "A unified analysis of PWM converters in discontinuous modes," *IEEE Trans. Power Electron.*, vol. 6, no. 3, pp. 476–490, 1991, <https://doi.org/10.1109/63.85890>.
 47. A. Djemouai, M. Sawan, and M. Slamani, "New CMOS integrated pulse width modulator for voltage conversion applications," *Proc. IEEE Int. Conf. Electron. Circuits, Syst.*, vol. 1, no. 2, pp. 116–119, 2000, <https://doi.org/10.1109/ICECS.2000.911498>.
 48. W. Mathis, "Nonlinear systems and communications systems," *5th Int. Conf. Telecommun. Mod. Satell. Cable Broadcast. Serv. TELSIKS 2001 - Proc. Pap.*, vol. 1, no. September, pp. 293–296, 2001, <https://doi.org/10.1109/TELSKS.2001.954894>.
 49. S. V. Singh and C. Shankar, "A new Trans-Impedance Mode biquad filter employing single DVC-CTA," *Journal of Electrical Systems*, Vol. 15, pp. 249–263, 2019.



Copyright © 2024 by the Authors. This is an open access article distributed under the Creative Commons Attribution (CC BY) License (<https://creativecommons.org/licenses/by/4.0/>), which permits unrestricted use, distribution, and reproduction in any medium, provided the original work is properly cited.

Arrived: 07. 02. 2024

Accepted: 18. 05. 2024

Empirical Light-soaking and Relaxation Model of Perovskite Solar Cells in an Indoor Environment

Matija Pirc

Laboratory of Photovoltaics and Optoelectronics, University of Ljubljana, Faculty of Electrical Engineering, Ljubljana, Slovenia

Abstract: Perovskite Solar Cell (PSC) technology is approaching the level of maturity required for some niche applications, primarily in indoor environments. However, their metastability, expressed in the form of the light-soaking effect (LSE), makes it difficult to accurately estimate their expected real-life performance. This work demonstrates a new approach to LSE modelling, which can be used to determine the performance parameters of the PSC based on the history of its irradiance. The model was developed and tested on PSC performance data recorded during one month of operation in a realistic uncontrolled indoor environment, two days of which were used for the tuning of the model and the rest for its verification. The presented model was compared to two static one-diode models, which do not account for the LSE. The energy yield prediction error of the new model was only -0.72 %, the error of the static model based on low-light measurements was +6.96 %, and the error of the static model based on measurements under standard test conditions (STC) was +7.76 %. EY prediction of the low-light static model can however be arbitrarily improved by cherry picking the I-V curve on which to base the model, once the expected result is known. A more meaningful measure of model performance is the mean absolute error (MAE) of the predicted power at the maximum power point PMPP. The MAE of PMPP predicted by the new model was 16.7% lower than that of the low-light static model and 17.1 % lower than that of the STC static model.

Keywords: perovskite solar cells; light-soaking; indoor photovoltaics; I-V curve; energy yield

Empirični model svetlobnega prežemanja in relaksacije perovskitnih sončnih celic v notranjem okolju

Izveček: Tehnologija perovskitnih sončnih celic (PSC) se približuje stopnji zrelosti, ki je potrebna za vstop na trg nekaterih nišnih aplikacij, predvsem v notranjem okolju. Zaradi njihove metastabilnosti, ki se izraža v obliki učinka svetlobnega prežemanja (ang. Light-soaking Effect - LSE), težko natančno ocenimo njihovo pričakovano učinkovitost v realnem okolju. To delo prikazuje nov način modeliranja LSE, ki omogoča napovedovanje delovanja PSC na podlagi zgodovine obsevanosti. Model je bil razvit in preizkušen na enomesečnih meritvah delovanja PSC v realnih nenadzorovanih notranjih pogojih delovanja. Podatki dveh dni so bili uporabljeni za umerjanje modela, preostali podatki pa za preverjanje njegovega delovanja. Predstavljeni model smo primerjali z dvema statičnima enodiodnima modeloma, ki ne upoštevata LSE. Napaka napovedi energijskega izplena novega modela je bila le -0,72 %, medtem ko je napaka statičnega enodiodnega modela, osnovanega na meritvah pri nizki osvetljenosti, znašala +6,96 % in napaka statičnega enodiodnega modela, osnovanega na meritvah pod standardnimi testnimi pogoji (ang. Standard Test Conditions - STC), znašala +7,76 %. Napoved energijskega izplena statičnega modela osnovanega na meritvah pri nizki osvetljenosti, je mogoče pri znanem želenem rezultatu skoraj poljubno izboljšati z izbiro krivulje I-U, na kateri ta model temelji, zato napaka energijskega izplena ni najboljši merilo uspešnosti modela. Boljše merilo je srednja absolutna vrednost napake (ang. Mean Absolute Error - MAE) napovedane moči v točki največje moči PMPP. MAE napovedane PMPP novega modela je bila za 16,7 % manjša od MAE napovedi statičnega modela, osnovanega na meritvah pri nizki osvetljenosti in 17,1 % manjša od MAE napovedi statičnega modela, osnovanega na STC meritvah.

Ključne besede: perovskitne sončne celice, svetlobno prežemanje, notranja fotovoltaika, I-U karakteristika, energijski izplen

* Corresponding Author's e-mail: matija.pirc@fe.uni-lj.si

How to cite:

M. Pirc, "Empirical Light-soaking and Relaxation Model of Perovskite Solar Cells in an Indoor Environment", Inf. Midem-J. Microelectron. Electron. Compon. Mater., Vol. 54, No. 2(2024), pp. 149–161

1 Introduction

In the field of photovoltaics (PV) perovskite solar cells (PSC) have received a lot of attention during the last decade due to their high power conversion efficiency (PCE) potential [1], [2] and simple and low cost production process [3]–[5]. Despite their great advantages, they also have a few weaknesses hindering their widespread adoption, namely the use of toxic materials like lead [6]–[8] and their less than desirable long-term stability [9], [10]. However, intense research efforts are also improving these areas to the point that commercial applications are becoming feasible [11]. One of the niches the first commercial PSCs will most likely flourish in is indoor PV [12], [13], due to the mild operating environment, and their high and tunable bandgap energy [14]–[16], which makes them particularly suitable for use with artificial light sources that emit light in the human visible light spectrum by design. At the same time, a vast opportunity for indoor PV is opening with the rapid expansion of the Internet of Things (IoT) market [17] and PSCs could be the perfect solution.

For any PV use case an estimation of power capacity and expected energy yield (EY) is required. The estimation process can be as simple as taking the average irradiation and nominal solar cell efficiency to get a rough estimation of expected EY or an in-depth analysis taking into account measured device characteristics, temperature dependence, angular irradiance distribution, spectra, etc. [18]–[22]. Such analysis is not only useful for adequate sizing of PV installations or PV devices, but also for optimizing the structure of PV devices [18], [21], real-time monitoring and early fault detection by comparing the predicted and real performance of an installation, as well as gaining deeper insights into the operation of solar cells.

Although methodologies for predicting solar cell performance and calculating EY have evolved significantly and are capable of remarkable accuracy in the case of established technologies like silicon solar cells, PSCs are still a challenge due to their short-term instability, widely known as the light-soaking effect (LSE). A simple approach to sidestepping the challenges of the LSE in outdoor environments is to use the performance characteristics of a fully light-soaked PSC throughout the whole day [22]. This method is quite accurate for outside environments on bright sunny days when the LSE rapidly reaches saturation. However, in indoor environments, or even outdoors on particularly cloudy or foggy days, the LSE is much slower due to lower irradiance and may not reach saturation at all, yet still significantly affects the performance [23], [24]. In these cases, a method for predicting the state of the LSE of a PSC based on the history of its irradiance could significantly

improve the accuracy of the PSC energy yield calculations.

Many mechanisms contribute to the LSE, e.g. light induced ion migration, trap defect passivation, charge carrier accumulation, lattice expansion, etc. [25]–[28]. The bulk of the research of the LSE focuses on understanding the mechanisms behind it and the models developed are quite involved and usually require in-depth knowledge of the specific PSC. For the purpose of long-term performance predictions, these models are often computationally too intensive and require device parameters which are challenging to acquire. Long-term performance modelling generally requires different, high-level models, which are comparatively easy to tune and use on large data sets of environmental parameters.

In this contribution, we present an empirical model of the LSE which was developed by analyzing recorded data of PSC performance in a realistic, uncontrolled indoor environment. The model can be tuned on a few days' worth of measured data and then used to predict the I - V curves of the PSC based on the history of its irradiance for any point in time. We also discuss the shortcomings of the model and explore the possibilities of further research and improvements.

2 Materials and methods

2.1 Measurement Setup

PSC performance and environmental parameters were monitored and logged by an in-house designed Indoor Monitoring System which is thoroughly described in [24], therefore only the relevant details will be repeated here. The system maintains four solar cells at the MPP, and logs the average values of their performance, irradiance, temperature and humidity every 5 minutes. Additionally, I - V scans of all the cells are performed every half an hour. I - V scans are performed in voltage steps of approximately 20 mV every 60 ms, starting at V_{oc} , sweeping down to 0 and then back up to V_{oc} . During each step, the irradiance is measured and stored with the I - V data to facilitate subsequent detection of unsuitable lighting conditions, e.g. sudden changes in the irradiance during an I - V scan.

The system was designed to mimic a realistic indoor PV powered device between I - V scans, which would shut down MPP tracking when the energy cost of MPP tracking would exceed energy gains. Therefore, when the current of the PSC falls below 30 μ A, MPP tracking and energy harvesting is suspended.

The monitoring system was located on a shelf approximately at the center of the Laboratory of Photovoltaics and Optoelectronic office 1 (LPVO-1) in Ljubljana, Slovenia, with windows facing north-north-west (336°). This means that direct sunlight is possible only for a few minutes in the evenings from about a month before to about a month after the summer solstice, which was not the case within the timespan of the measurements used here.

Irradiance was measured with a silicone photodiode SFH2440L with an IR-cut filter, to adjust the spectral response of the photodiode to be more similar to the spectral response of the PSC. Unfortunately, the difference between both spectral responses is still quite large and since the spectrum of light changes considerably when the ratio of natural and artificial lighting changes, the irradiance measurement accuracy leaves something to be desired. Although the accuracy is sufficient for the LSE modelling and performance prediction, PCE calculations based on these measurements are not recommended.

2.2 Perovskite solar cell

The structure of the PSC was glass | ITO | MeO-2PACz | perovskite | C₆₀ | SnO₂ | Cu in a p-i-n architecture, where the MeO-2PACz monolayer (2-(3,6-Dimethoxy-9H-carbazol-9-yl)ethyl)phosphonic acid) is a hole transport layer (HTL), and the C₆₀ and SnO₂ layers are electron transport layers (ETL). The perovskite absorber is a formamidinium-caesium (FACs) double cation perovskite absorber with the chemical formula FA_{0.83}Cs_{0.17}Pb(I_{0.83}Br_{0.17})₃. The back and front contacts are connected with 2 self-adhesive copper stripes. The device is sealed between 2 sheets of glass with two-component 5-minute epoxy. The area of the PSC is 1.06 cm² and under standard test conditions (STC) the short-circuit current density is 22.3 mA/cm², open-circuit voltage 1.13 V, fill factor 78.6 % and PCE 19.9 %. The *J-V*

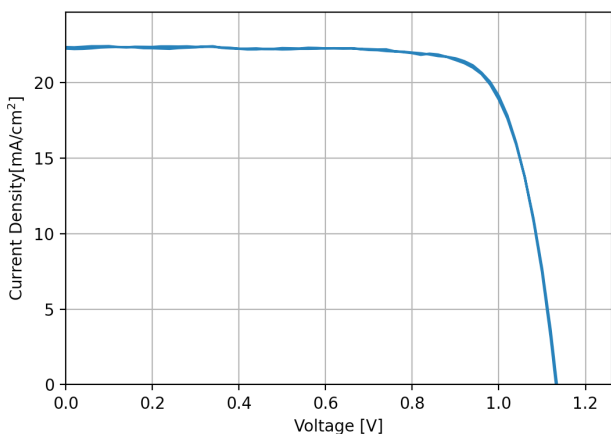


Figure 1: J-V of the PSC under STC

curve under STC and the external quantum efficiency (EQE) of the PSC, along with the EQE of the photodiode for measuring irradiance are shown in Figs. 1 and 2, respectively.

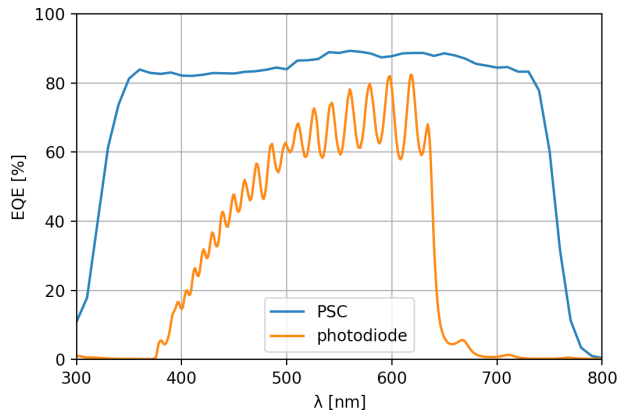


Figure 2: Spectral response of the PSC and photodiode with IR-cut filter for measuring irradiance.

2.3 Data preparation

Because the measurements were performed in an uncontrolled environment, not all the measurements were valid, e.g. when the irradiance was changing too much during the *I-V* scan. To filter out these scans, the standard deviation of the irradiance during each *I-V* scan was calculated and all *I-V* scans with a standard deviation of irradiance larger than 1 % of the average irradiance or larger than 0.005 W/m² were ignored. *I-V* scans with an average irradiance lower than 0.15 W/m² were also ignored, because the current measurement noise becomes too prevalent at such low irradiance. For easier comparisons with other studies all cell parameters and measurements were normalized to the area of 1 cm².

3 The Light-soaking Model

The effect of Light-soaking can be readily discerned by observing the *J-V* scans taken throughout a typical day. Fig. 3 shows the *J-V* scans recorded on August 1, 2022 progressing from light to dark color from the morning to the evening. The LSE is most apparent when comparing the *J-V* scans taken very early in the morning and very late in the evening. When the two marked scans were acquired, the irradiance was very similar (0.80 and 0.76 W/m², respectively), yet the *V_{oc}* was 90 mV higher in the evening (15 %), even though the irradiance was slightly lower.

Even though the LSE is most evident in increased *V_{oc}*, the *V_{oc}* has a very strong dependence on the irradiance

G , which makes it impossible to determine the size of the LSE from the V_{oc} alone.

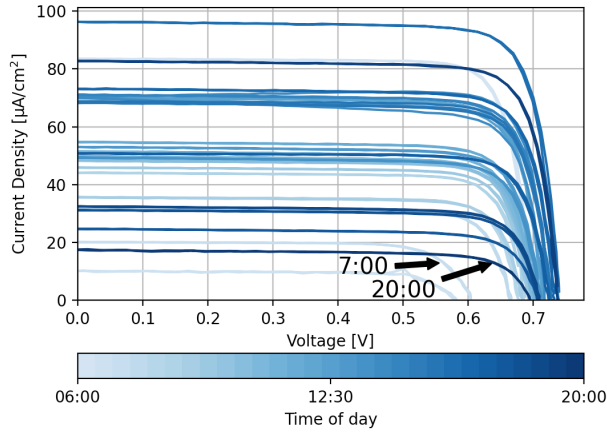


Figure 3: J - V scans of the PSC recorded on August 1, 2022. Line color hue indicates the time of the scan – from bright in the morning to dark in the evening. The two marked lines show the LSE most prominently.

3.1 One-diode Model Parameters

Power and EY calculations are possible as soon as the J - V curves for each point in time are determined. Solar cell J - V curves are often modelled by a one- or two-diode model. If the parameters of the model can be determined, all other calculations can be performed as well. To see if the parameters of such a model could be used to predict the influence of the LSE, a mass fit on all the J - V scans of the PSC acquired in August 2022 was performed using the 2/3 Diode Fit program [29]. With some experimentation we determined that a one-diode model is sufficient to achieve a very good fit for all the J - V scans and with the low irradiance in the indoor environment and therefore small currents, even the series resistance of the one-diode model can be safely disregarded. The one-diode model used in the study is shown in Fig. 4 and it is described by equation (1)

$$J = J_{PH} - J_S \left(\exp\left(\frac{V}{nkT/q}\right) - 1 \right) - \frac{V}{R_p} \quad (1)$$

where J_{PH} is photo-current density, J_S saturation current density of the diode, n ideality factor, k Boltzmann constant, T temperature, q electron charge, R_p shunt resistance and V voltage of the solar cell.

The photo-current density J_{PH} , which, in the case of zero series resistance, is equal to the short-circuit current density J_{SC} , is expected to be directly proportional to the irradiance G . This was confirmed by Fig. 5, which shows that measurements exhibit linear dependence

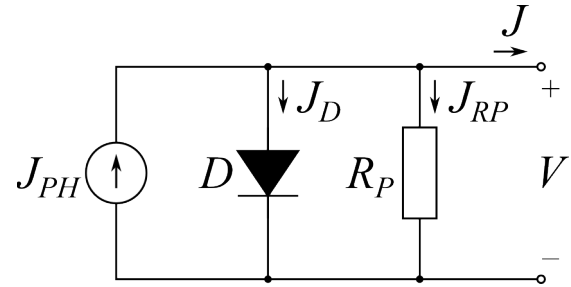


Figure 4: One-diode model used to model the PSC.

on irradiance with deviations of only a few percent, except for a few outliers most likely resulting from local shading.

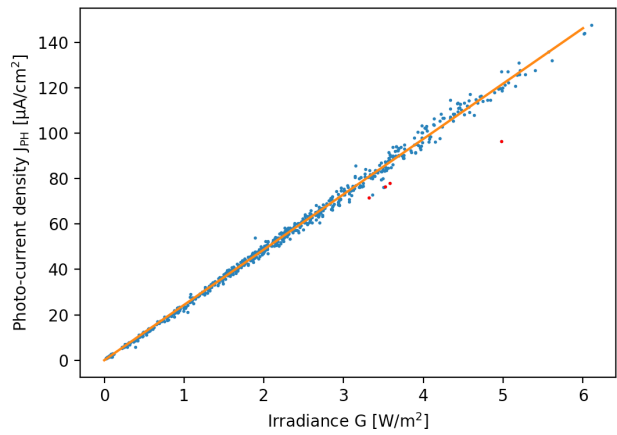


Figure 5: Short-circuit current density J_{SC} of all J - V scans vs. irradiance G (blue dots) and a linear fit to the data (orange line). The few red dots are considered to be outliers. The R^2 score of the fit without the outliers is 0.996.

Plotting the time evolution of the fitted parameters of the one-diode model unveils a weak correlation be-

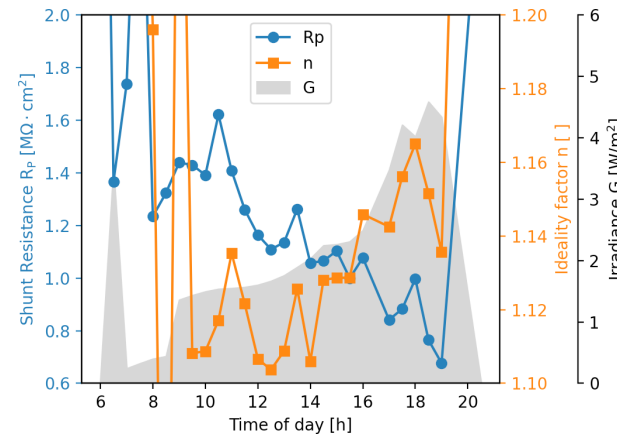


Figure 6: Time evolution of the ideality factor n (orange squares) and parallel resistance R_p , normalized to 1 cm^2 (blue circles) on August 5, 2022. The gray fill shows irradiance.

tween the ideality factor n and the irradiance G , as well as an inverse correlation between the parallel resistance R_p and the irradiance G throughout most of the day. Fig. 6 shows n , R_p and G on August 5, 2022. This date was selected because irradiance more or less steadily rises during the day, making it easier to perceive the observed correlations.

Saturation current density J_s on the other hand does not seem to have an obvious direct correlation to irradiance. Therefore Fig. 7 shows its time evolution for all days in August. On most days (but not all) the J_s starts quite high, drops by 2 or 3 orders of magnitude in the first 2 hours, and after that more or less steadily falls until the evening.

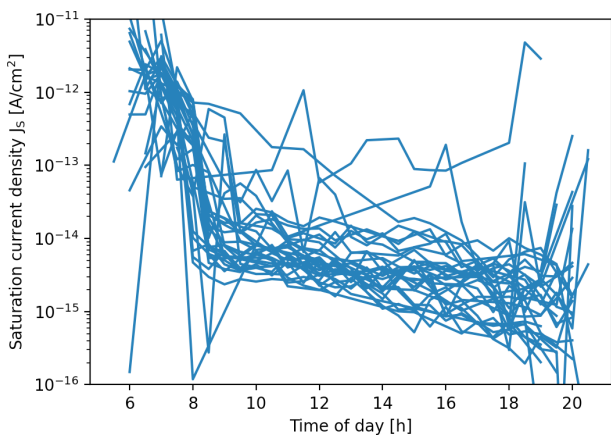


Figure 7: Time evolution of the saturation current density J_s throughout every day of August 2022.

The correlations of n and R_p to G are discernible between approximately 9:00 or 10:00 in the morning and 18:00 or 19:00 in the evening. Before and after that the correlations don't seem to hold or they are simply lost in the noise. When irradiance is low, the noise in the measurements makes for a very undefined fit, which can result in very large and unrealistic swings in parameter values.

To verify the observed correlations, we plotted the one-diode parameters of all J - V curves as a function of irradiance, shown in Figs. 8 through 10. The majority of values of the ideality factor n fall within a narrow range between 1.1 and 1.2 with some outliers, especially at lower irradiance values, falling outside this range. Values that do fall within this range seem to exhibit a slight linear dependence on irradiance, confirming the previous observation. It is likely that some of the outliers are not just the result of ambiguity when fitting the one-diode model to noisy data, but instead the ideality factor may also depend on the state of light-soaking. However, at this stage we are not yet sure if that is really the case, and for now we consider data points that

deviate enough from the main linear trend as outliers. The linear fit

$$n = n_0 + k_n G \tag{2}$$

depicted by the orange line in Fig. 8, where G is irradiance, the intercept n_0 is 1.094 and the linear coefficient k_n is $0.015 \text{ m}^2/\text{W}$, was performed using the RANSAC linear regression method (RANDOM SAMPLE CONSENSUS) from the python package Scikit-learn [30] with the residual threshold value of 0.05. The red dots in Fig. 8 are the ideality factor values which the RANSAC algorithm marked as outliers. Due to the intrinsic randomness of the RANSAC algorithm, the fit is slightly different for each run. The R^2 score of the fit without outliers varies between 0.5 to 0.7 from run to run.

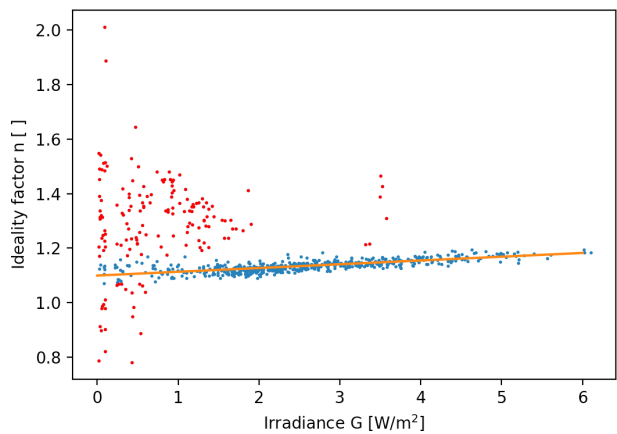


Figure 8: Ideality factors n of all the fits to J - V curves vs irradiance G (dots) and a linear fit to the data (orange line). The red dots are outliers as determined by the RANSAC fit method. The R^2 score of the fit without the outliers averages around 0.6.

Parallel resistance values (Fig. 9) mostly fall between 0.8 and $3 \text{ M}\Omega\text{-cm}^2$. Values larger than that have almost no influence on the J - V curve (smaller than the measurement accuracy), and are therefore just an artifact of the one-diode model fitting process. The datapoints give an impression of negative exponential relation to irradiance, which is similar to the inverse correlation observed in the time evolution of parallel resistance and irradiance shown in Fig. 6. We modelled the relation between parallel resistance R_P and irradiance G with the equation (3)

$$R_P = R_{P_{MIN}} + R_{PE} \exp\left(-\frac{G}{G_K}\right) \tag{3}$$

depicted by the orange line in Fig. 9, where G is irradiance, $R_{P_{MIN}}$ is $0.784 \text{ M}\Omega\text{-cm}^2$, R_{PE} is $1.390 \text{ M}\Omega\text{-cm}^2$ and G_K is 1.440 W/m^2 . The fit was acquired using a similar

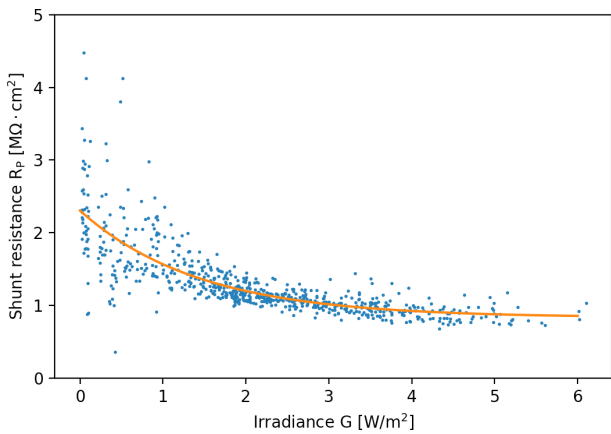


Figure 9: Parallel resistance R_p of all the fits to J - V curves vs irradiance G (blue dots) and an exponential fit to the data (orange line). The R^2 score of the fit without outliers is 0.637.

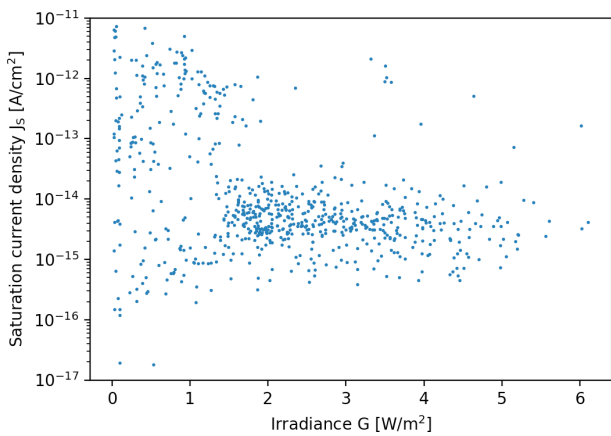


Figure 10: Saturation current J_s of all the fits to J - V curves vs irradiance G .

approach to the RANSAC linear regression method, but using our own code built on top of the python lmfit package, since the Scikit-learn package does not have a built-in function for RANSAC exponential regression. In the case of parallel resistance, the outliers are much more obvious (out of range of Fig. 9) than in the case of the ideality factor, therefore more or less the same datapoints are marked as outliers in each run and the results of the fit are much more consistent from run to run. The R^2 score of the fit without outliers is 0.637.

Saturation current densities resulting from the fittings of the data to the one-diode model, shown in Fig. 10, span a large range of values and do not show a direct correlation to irradiance as already expected based on Fig. 7. Therefore, we assume that the greater part of the LSE is encompassed within this parameter.

For additional context, the one-diode parameters of the same PSC have been extracted from the I - V curve

measured after the PSC was fully light-soaked under STC. In this case the saturation current density J_s is $1.1 \cdot 10^{-10}$ A/cm², the ideality factor n is 2.31, and parallel resistance R_p is infinite (any value above 10 kΩ gives good fit results). On the other hand, the model does require a series resistance of 1.15 Ω. The measured short-circuit current density is 22.3 mA/cm², which is 13.5 % lower than would be expected based on the photocurrent dependence on irradiance shown in Fig. 5. The ideality factor is considerably larger than in low light conditions, however, based on equation (2) it should be about 7 times larger still, showing that the linear fit is only valid within the range of low irradiances.

3.2 Linking one-diode model parameters to a single observable of the LSE

The challenge of predicting the size of the saturation current lies in its very large range of possible values as well as in its close connection to the ideality factor n . A small change in the ideality factor n , can be compensated with quite a large change in the saturation current density to achieve an almost identical J - V scan fit, as shown in Fig. 11. The two fits shown represent the measured data practically equally well, but the saturation current density of the second fit is approximately 5 times larger than that of the first fit while the difference in the ideality factor is less than 10 %. The parallel resistance is the same in both cases. This means that predicting the value of the saturation current independently from the ideality factor would not be the most reliable way of predicting the size of the LSE. Therefore, a more robust parameter, combining the saturation current density with other parameters, would be a better option for predicting the LSE.

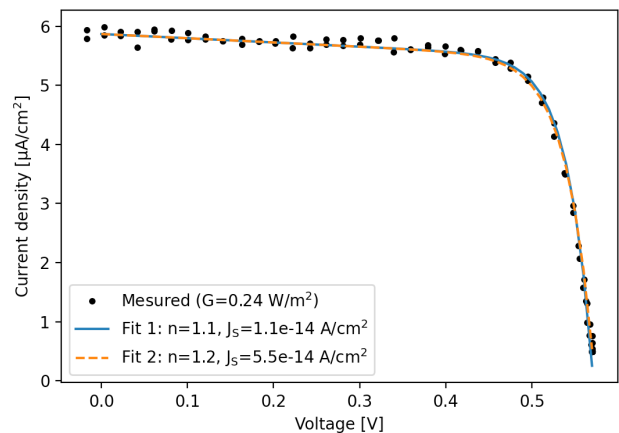


Figure 11: Demonstration of strong dependence of the J_s parameter on the n parameter of the one-diode model – under 10 % change in n requires 500 % change in J_s to get an almost identical fit within the measured range of data.

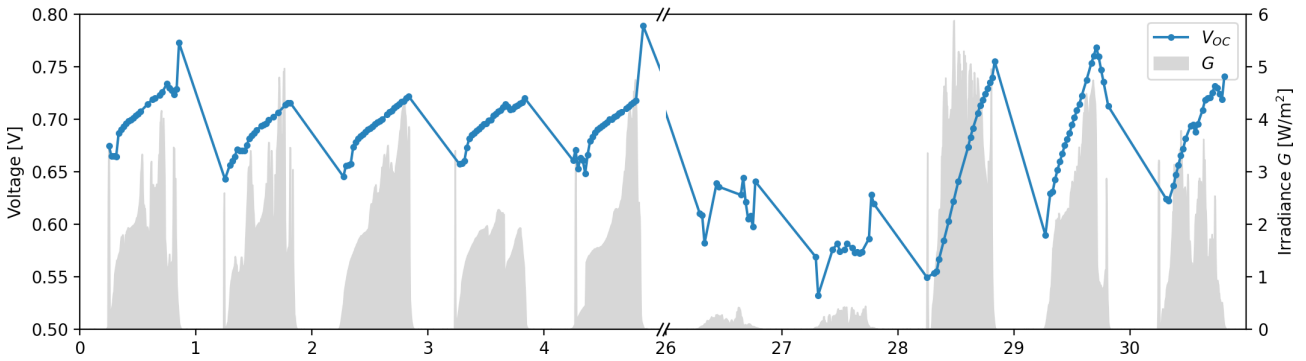


Figure 12: Time evolution of V_{oc} at a pre-selected photo-current density of $73.3 \mu\text{A}/\text{cm}^2$, equivalent to irradiance of $3 \text{ W}/\text{m}^2$, during the first 5 and last 5 days of August.

Open-circuit voltage is the most obvious parameter where the effects of light-soaking are evident. However, as already mentioned, it also strongly depends on the photocurrent, which in turn depends on the irradiance. The effect of light-soaking on the V_{oc} could be isolated from the direct effect of the irradiance if the I - V curves were always measured at the same irradiance. Although this was not possible within the experiment, such a measurement should only marginally affect the shape of the curve through minor changes to the ideality factor and the parallel resistance according to (2) and (3), provided the scan time at a different irradiance was short enough not to meaningfully change the amount of light-soaking. On the other hand, once a one-diode model fit is obtained, a V_{oc} at a pre-selected photo-current can be easily calculated with reasonable accuracy. Fig. 12 shows the time evolution of the calculated V_{oc} at a pre-selected photo-current density of $73.3 \mu\text{A}/\text{cm}^2$, which corresponds to $3 \text{ W}/\text{m}^2$ irradiance – approximately half of the maximum irradiance measured in August.

The time evolution of the V_{oc} at the pre-selected current indicates that the LSE more or less steadily increases throughout most days, with quite a weak dependence on the irradiance and only shows a decrease when the irradiance drops very drastically. Combining these observations with the observed speed with which the LSE increases under STC or in an outdoor environment compared to the indoor environment, leads us to believe that the speed of the LSE, or at least this parameter which indicates the state of the LSE, is proportional to the logarithm of the irradiance.

3.3 Discrete linear time-invariant system for LSE dependent VOC prediction

Previous studies [26], [27] have shown that at a constant irradiance, the V_{oc} of a PSC follows an increasing exponential decay form with an offset V_{ocMIN} (4), remi-

niscient of the voltage of a capacitor while charging to a fixed voltage through a resistor, if the offset is ignored.

$$V_{oc}(t) = V_{ocMIN} + V_{ocLS} \left(1 - \exp\left(-\frac{t}{\tau}\right) \right) \quad (4)$$

The time evolution of the V_{oc} in Fig. 12 looks like it could fit the same increasing exponential decay form, but with quite a long time constant. In light of this, we sought to model the LSE with a linear time-invariant (LTI) system, which takes a logarithm of the time resolved irradiance as an input and outputs the time resolved V_{oc} at a pre-selected current density. The predicted V_{oc} calculated for each point in time can then be used together with the ideality factor n and parallel resistance R_p calculated from the irradiance using (2) and (3) to determine the saturation current density J_s .

The step response of the system shown in (4) has an offset V_{ocMIN} which has to be treated separately since a system with an offset does not satisfy the homogeneity condition for linearity and is therefore not an LTI system. The step response of the linear part of the system is therefore

$$V_{oc}(t) = V_{ocLS} \left(1 - \exp\left(-\frac{t}{\tau}\right) \right) \quad (5)$$

where τ is the time constant of the LSE and V_{ocLS} is the size of the input step function determined by the irradiance and represents the final increase of the V_{oc} due to the LSE. The $V_{oc}(t)$ is assumed to be 0 for $t < 0$, but is not denoted within the equation by multiplication of the right-hand side with a unity step function for clarity's sake, as will be the case henceforth.

The LTI system could be modelled by a resistor-capacitor (RC) electrical circuit, and its response calculated by any electrical circuit simulator. However, since all the

measured data, including the irradiance, which will be the input to the system, is sampled at discrete points in time, it is more convenient to construct and run a discrete-time LTI system with an equivalent response. To do that, we first rewrite (5) as a unit step response $g(t)$ and derive the system's impulse response $h(t)$

$$g(t) = 1 - \exp\left(-\frac{t}{\tau}\right) \quad (6)$$

$$h(t) = \frac{dg(t)}{dt} = \frac{1}{\tau} \exp\left(-\frac{t}{\tau}\right) \quad (7)$$

Periodically sampling the impulse response with a sampling period of T_s , we get

$$h(nT_s) = \frac{1}{\tau} \exp\left(-\frac{nT_s}{\tau}\right) \quad (8)$$

which can be rewritten in its discrete-time form as

$$h[n] = K \cdot a^n \quad (9)$$

where K equals $1/\tau$ and a equals $\exp(-T_s/\tau)$.

The Z-transform of (9)

$$H(z) = K \cdot \frac{z}{z-a} \quad (10)$$

can be used to construct a difference equation of a discrete-time system

$$y[n] = K \cdot x[n] + a \cdot y[n-1] \quad (11)$$

where $x[n]$ are the consecutive input values of the system (logarithm of the irradiance) and $y[n]$ are the consecutive output values of the system (increase of the V_{oc} due to the LSE).

Before the logarithm function can be applied to the irradiance, the irradiance needs to be normalized to a reference value. We assume some minimal irradiance is required for the processes contributing to the LSE to start, although so far, we have not found any reports on the matter. Therefore, we define the logarithmic irradiance GL as

$$GL = \log_{10} \frac{G}{G_{MIN}} \quad (12)$$

The values of the irradiance G are also downward limited to G_{MIN} to avoid negative and complex values of GL , which can appear when negative values of irradiance are measured due to noise when the real irradiance is below the noise threshold of the instrument. The complete model for predicting the V_{oc} is described by Pseudo-code 1:

Pseudo-code 1: V_{oc} prediction model.

INPUT: vector G

OUTPUT: vector V_{oc}

```

 $V_{oc}^{[0]} = V_{oc}^{[0]}$ 
for  $n = 1$  to length( $G$ )-1
     $G_{LIM}^{[n]} = \max(G[n], G_{MIN})$ 
     $GL[n] = \log_{10}(G_{LIM}^{[n]}/G_{MIN})$ 
     $V_{oc}^{[n]} = K \cdot GL[n] + a \cdot V_{oc}^{[n-1]}$ 
 $V_{oc}^{[n]} = V_{oc}^{[n]} + V_{oc}^{[n]}$ 
end for

```

Before the model can be used for predicting the values of the V_{oc} at the pre-selected photo-current, the constants G_{MIN} , $V_{oc}^{[0]}$, K , a , and $V_{oc}^{[n]}$ have to be tuned to the specific solar cell. This can be achieved by treating the constants as parameters of a model, and fitting the model to the known values of the V_{oc} at the specific times when it was measured. We used the data of the first 2 days to tune the model and the rest of the data to assess the performance of the model. The values of the constants after the tuning process are collected in Table 1.

Table 1: Tuned model parameters.

Parameter	Value
G_{MIN}	0.0001 W/m ²
$V_{oc}^{[0]}$	0.303 V
$V_{oc}^{[n]}$	0.425 V
K	2.949·10 ⁻⁴
a	0.99689

4 Results

Fig. 13 shows the V_{oc} at the pre-selected photo-current density of 73.3 $\mu\text{A}/\text{cm}^2$, corresponding to an irradiance of 3 W/m², calculated from the one-diode model fits of the measured I-V scans (blue circles) and predicted by the new model (orange line). The gray filled area represents the logarithm of the normalized irradiance, which is used as an input to the LTI system predicting the V_{oc} . Fig. 14 shows the measured (blue circles) and the predicted (orange dots) P_{MPP} as well as the P_{MPP} predicted by two static models (green Xs and red plusses), which

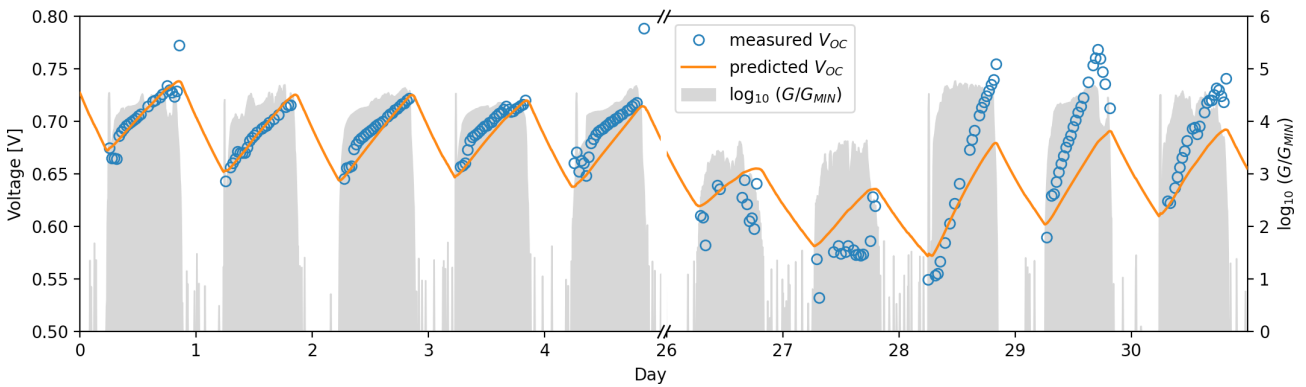


Figure 13: The measured (blue circles) and the predicted (orange line) V_{OC} at the pre-selected photo-current density of $73.3 \mu A/cm^2$, equivalent to an irradiance of $3 W/m^2$, for the first 5 and last 5 days of August. The gray fill shows the logarithm of the irradiance normalized to the minimum irradiance, which is used as the input to the prediction LTI system.

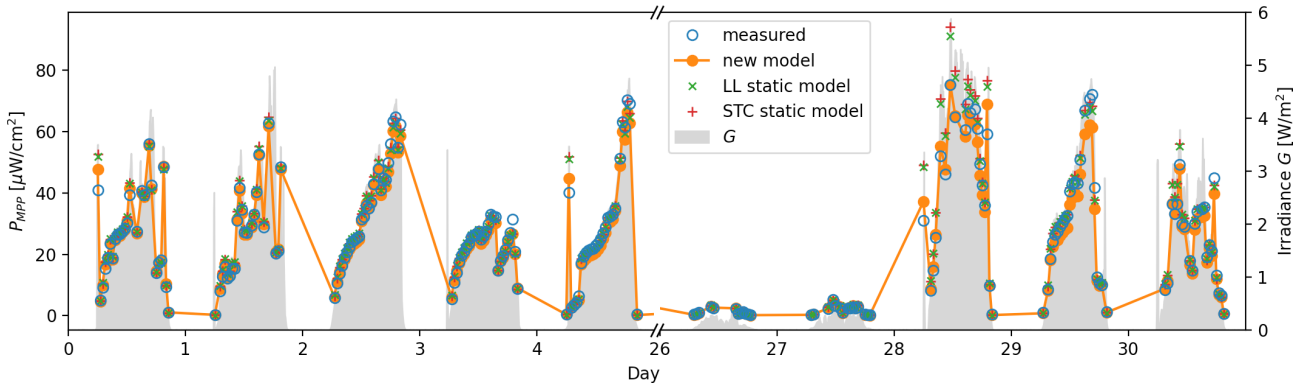


Figure 14: The measured P_{MPP} (blue circles), the P_{MPP} predicted by the new model (orange line with dots), the P_{MPP} predicted using the low-light static model (green Xs), and the P_{MPP} predicted using the STC static model (red plusses) for the first 5 and the last 5 days of August.

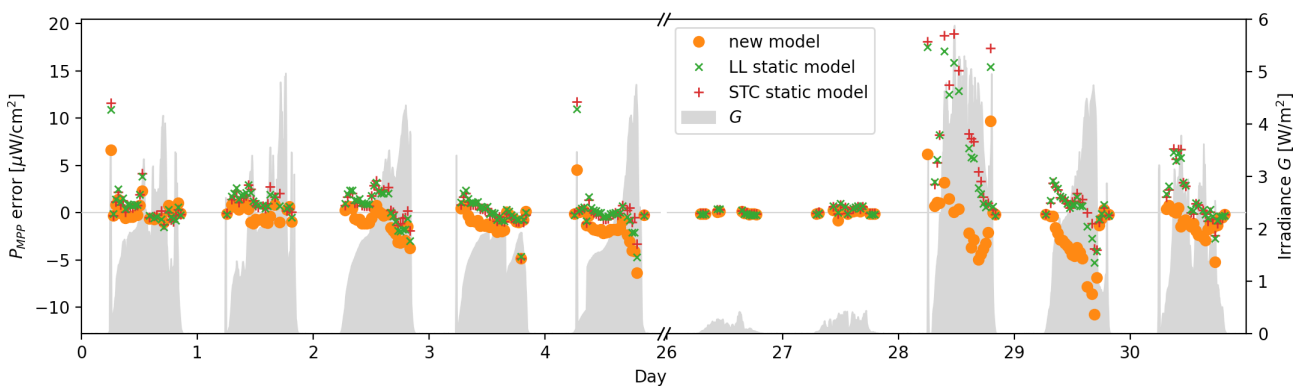


Figure 15: The P_{MPP} prediction errors of the new model (orange dots), the low-light static model (green Xs), and the STC static model (red plusses) for the first 5 and the last 5 days of August.

do not take the LSE into account, to provide a basis for comparison. Fig. 15 shows the errors of the new model (orange dots) and the two reference static models (green Xs and red plusses). The gray fill in Figs. 14 and 15 shows irradiance. All three figures show the data for the first 5 days and the last 5 days of August 2022.

The V_{OC} predicted by the new model follows the measured V_{OC} quite well at the beginning of the month, but not quite as well at the end of the month. The V_{OC} values measured on the 27th and 28th of August (Saturday and Sunday) seem to change quite unpredictably, which is the result of very low irradiance and therefore a low signal to noise ratio. The very low irradiance is consistent

with the blinds being lowered all the way down. Despite this, the predicted V_{OC} values are in the general vicinity of the measured values. On the last three days of August, the model underestimates the LSE and the predicted V_{OC} lags considerably behind the measured V_{OC} . Such discrepancies between the measurements and predictions begin to appear in the second half of the month. This behavior is reflected in the predicted P_{MPP} which also matches the measured P_{MPP} very well at the beginning of the month, and not nearly as well towards the end of the month.

The static models used as a basis for comparison consist of taking a single $I-V$ scan, obtaining a fit to the one-diode model and using the obtained parameters to calculate the P_{MPP} for every point in time based on the irradiance. Energy yield predictions or analysis in outdoor environments are often performed using measured stabilized $I-V$ characteristics of the PSC, which means the $I-V$ scan is taken only after the cell has been fully light-soaked. Since the fully light-soaked state can be reached quite quickly in a bright outdoor environment, the error introduced by this approach is acceptable in most cases. In the case of low-light environments, however, the LSE may not reach saturation even after an entire day, therefore an $I-V$ scan taken sometime in the middle of the day may be more representative. We decided to use both approaches and derive one static model based on an $I-V$ scan performed in low-light conditions on the first day of the measurements, when the brightness was the highest (green Xs in figures, hereafter referred to as the low-light or LL static model) and the other based on the $I-V$ scan of the fully light-soaked PSC under STC (red plusses in figures, hereafter referred to as the STC static model). The prediction error of the low-light static model is quite well balanced between positive and negative values at the beginning of the month, confirming a good choice of the $I-V$ scan to base the model on.

It has to be noted that selecting a different $I-V$ scan for the low-light static model can result in either better or worse predictions. EY calculations in particular can easily be manipulated by selecting just the right $I-V$ scan to get the desired result on a known dataset. Therefore, EY calculations and their errors are given for completeness and to give an idea of how large errors in the EY can potentially be expected, but are not a reliable measure of the quality of the method. Instead, the mean absolute error (MAE) and root mean square error (RMSE) of the P_{MPP} paint a much clearer picture, although they too depend on the selection of the $I-V$ scan in the case of the low-light static model and the selection of the model tuning period in the case of the new model. The STC static model on the other hand is much less tweakable.

A good selection of the tuning period is essential for the performance of the model. Tests showed that the minimum tuning period is 2 days, because this ensures that the relaxation of the LSE is well defined in the training data. Longer training periods are generally beneficial, but not necessarily by much. If the selected training period includes representative conditions, increasing the training period does not improve the model's performance greatly. However, longer tuning periods usually include a wider range of conditions and thus provide a more representative dataset and therefore result in a better performing model.

The P_{MPP} predictions of both static models are very similar and the low-light static model performs only marginally better than the STC static model. However, a closer examination of the predictions shows a considerably different picture. Fig. 16 shows the measured and predicted $J-V$ (solid lines) and $P-V$ (dotted lines) curves, with the MPP marked with Xs on the $I-V$ curves and plusses on the $P-V$ curves. The predicted curves of the new model and the low-light static model match the general shape of the measured data very well. The STC static model, on the other hand, predicts a much more gradual drop in current density when approaching V_{OC} and considerably higher V_{OC} , resulting in a lower predicted fill-factor (FF). Although the general shape of the predicted $J-V$ curve is a much worse match to the measured data than those of the other models, the combination of increased V_{OC} and decreased FF coincidentally results in almost the same P_{MPP} as in the case of the low-light static model.

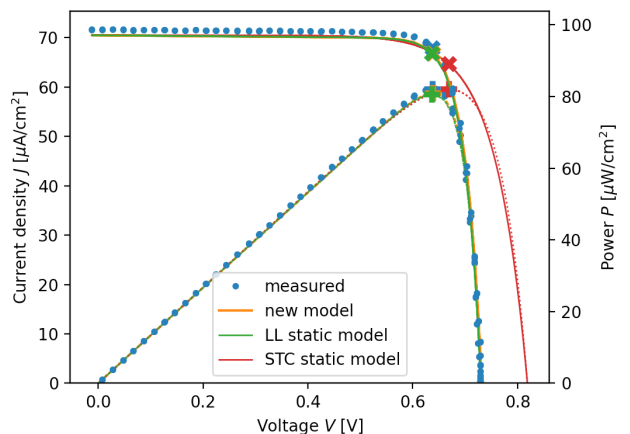


Figure 16: Measured (blue dots) and predicted $J-V$ curves (solid lines) and $P-V$ curves (dotted lines) of all three prediction models: the new model (orange), the low-light static model (green), and the STC static model (red). The MPP on the $J-V$ curve is marked with Xs, and on the $P-V$ curve with plusses.

The measured and predicted EY over the course of the month, as well as the MAE and RMSE of all the models

are summarized in Table 2. During the first half of the month the P_{MPP} predictions of the new model mostly outperform the predictions of both static models. However, at the end of the month, the errors of the static models are sometimes lower than those of the new model. Taking the entire prediction period into account, the MAE of the new model is 16.7 % lower than MAE of the low-light static model and 17.1 % lower than MAE of the STC static model. The RMSE indicates slightly lower improvement of 12.3 % and 15.6 % over the low-light and STC static models, respectively. The EY prediction errors of both static models are +6.96 % and +7.76 %, while the EY prediction error of the new model is only -0.72 %, which is extraordinary and probably due to a bit of luck as well.

Table 2: Performance comparison of the new model with the static model.

Parameter	Measurement	static model	STC static model	new model
EY [mWh/cm ²]	12.50	13.37	13.47	12.41
EY error [%]	-	+6.96	+7.76	-0.72
MAE(PMPP) [μW/cm ²]*	-	2.21	2.22	1.84
RMSE(PMPP) [μW/cm ²]*	-	3.26	3.39	2.86

* P_{MPP} varies between 0 and 94 μW/cm²

5 Discussion

The presented model of the LSE in the PSC predicts the state of the PSC based on the history of irradiance quite well in the first half of the month but starts to deviate in the second half. It has to be noted, that the model is never completely reset and errors in prediction accumulate with time. Yet, despite this, the error at the end of the month still remains strictly within $\pm 13 \mu\text{W}/\text{cm}^2$ and rarely exceeds $\pm 5 \mu\text{W}/\text{cm}^2$ (14 % and 5 % of the observed P_{MPP} range), exhibiting a degree of robustness of the model.

On the other hand, the model cannot predict the small variations the measured V_{OC} exhibits (Fig. 13), even at the beginning of the month. We believe the same basic approach could be used to model those variations as well, but with a more sophisticated LTI system. However, more research is need to isolate individual contributions of external parameters to light-soaking and to more carefully identify the system's response to external stimuli.

The experiment that provided the data for this work was designed to provide data on PSC performance in a realistic, uncontrolled indoor environment and statistical data on such an environment throughout the seasons of the year. As such, it was not optimized to gather data required for the LSE modelling. However, the recorded data was just accurate enough to facilitate the first steps in the LSE modelling in PSCs and inspire further research, which will hopefully provide higher quality data for a more accurate model as well as more reliable and extensive validation. The experiment had several shortcomings if viewed in light of the requirements for LSE research that will have to be improved upon in future research:

- Shading in realistic indoor environments can be very localized, therefore it is very important to place the irradiance sensor as close as possible to the device under test (DUT), or better yet, place several irradiance sensors on opposite sides of the DUT.
- Spectral matching of the irradiance sensor and the PSC remains a challenge for now, especially if the angular sensitivity of both devices needs to match as well. A workaround would be to avoid an uncontrolled environment and strictly control the spectrum of incident light.
- For the purpose of accurate one-diode model fitting, the current measurement accuracy needs to be increased.
- The irradiance within this experiment almost never exceeded 6 W/m², therefore the model is only verified within this low irradiance range.

In a more specialized experiment, the influence of temperature could also be characterized and perhaps included in the model. However, within this work, the measured temperature was accounted for only as a parameter of the one-diode model (1), even though it has been established before that it affects the LSE [25] as well. With the very limited changes in temperature in the indoor environment (26.4 °C to 34.0 °C) we assumed that all other sources of uncertainty overshadowed the influence of temperature.

Focusing on the prediction results for the second half of the month, we see several possible reasons for the reduced performance of the model. It is possible that changes in blinds positions (which were not recorded or otherwise logged) changed either the average spectrum of light enough to influence the LSE or changed the shading conditions, which could have led to a smaller indicated irradiance, which could in turn have caused the model to underestimate the LSE. PSCs are also known for their less than optimal long-term stability and it is possible that their performance changed enough during the first month to make a noticeable

difference in how the LSE manifests. However, it is impossible to conclusively determine the cause of the slightly worse performance at the end of the test period from the available data.

6 Conclusions

Within this work a new model for predicting the light-soaking effect (LSE) of perovskite solar cells (PSC) based on the history of their irradiance has been presented. The model uses the current irradiance to calculate the photo-current I_{PH} , the ideality factor n and the shunt resistance R_p of the one-diode model of the PSC. From the irradiance history it calculates the V_{OC} at a pre-selected current (to isolate the LSE from the influence of the photo-current on the V_{OC}), which is then used to calculate the saturation current of the one-diode model. The thus calculated one-diode model parameters account for the LSE and can be used in further analysis, like P_{MPP} or energy yield calculations.

The proposed model was compared to two static one-diode models over the course of one month and showed a 16.7 % improvement over the low-light static model and 17.1 % improvement over the STC static model in the mean absolute error (MAE) of the P_{MPP} prediction, achieving a MAE of 1.84 μ W compared to the 2.21 μ W and 2.22 μ W of the low-light and STC based static models, respectively, compared to the daily variations of P_{MPP} between 0 and approximately 94 μ W.

7 Acknowledgments

I would like to thank M. Topič, M. Jošt, Ž. Ajdič, Š. Tomšič, M. Jankovec and G. Matič for many fruitful discussions. The Research was funded by the Slovenian Research and Innovation Agency, program P2-0415.

8 Conflict of Interest

I have no conflict of interest to declare.

9 References

1. J.-Y. Shao *et al.*, "Recent progress in perovskite solar cells: material science," *Sci. China Chem.*, vol. 66, no. 1, pp. 10–64, Jan. 2023, <https://doi.org/10.1007/s11426-022-1445-2>.
2. "Best Research-Cell Efficiency Chart Provided by NREL." [Online]. Available: <https://www.nrel.gov/pv/assets/pdfs/best-research-cell-efficiencies.pdf>. [Accessed: 03-Aug-2023].
3. R. G. Charles, A. Doolin, R. García-Rodríguez, K. Valadez Villalobos, and M. L. Davies, "Circular economy for perovskite solar cells – drivers, progress and challenges," *Energy Environ. Sci.*, 2023, <https://doi.org/10.1039/D3EE00841J>.
4. A. S. R. Bati, Y. L. Zhong, P. L. Burn, M. K. Nazeeruddin, P. E. Shaw, and M. Batmunkh, "Next-generation applications for integrated perovskite solar cells," *Commun. Mater.*, vol. 4, no. 1, pp. 1–24, Jan. 2023, <https://doi.org/10.1038/s43246-022-00325-4>.
5. M. Mujahid, C. Chen, W. Hu, Z.-K. Wang, and Y. Duan, "Progress of High-Throughput and Low-Cost Flexible Perovskite Solar Cells," *Sol. RRL*, vol. 4, no. 8, p. 1900556, 2020, <https://doi.org/10.1002/solr.201900556>.
6. M. Wang *et al.*, "Lead-Free Perovskite Materials for Solar Cells," *Nano-Micro Lett.*, vol. 13, no. 1, p. 62, Jan. 2021, <https://doi.org/10.1007/s40820-020-00578-z>.
7. X. Liu *et al.*, "Lead-Free Perovskite Solar Cells with Over 10% Efficiency and Size 1 cm² Enabled by Solvent–Crystallization Regulation in a Two-Step Deposition Method," *ACS Energy Lett.*, vol. 7, no. 1, pp. 425–431, Jan. 2022, <https://doi.org/10.1021/acscenergylett.1c02651>.
8. A. E. Magdalin *et al.*, "Development of lead-free perovskite solar cells: Opportunities, challenges, and future technologies," *Results Eng.*, vol. 20, p. 101438, Dec. 2023, <https://doi.org/10.1016/j.rineng.2023.101438>.
9. T. Ahmed Chowdhury, M. A. B. Zafar, M. S.-U. Islam, M. Shahinuzzaman, M. Aminul Islam, and M. Uddin Khandaker, "Stability of perovskite solar cells: issues and prospects," *RSC Adv.*, vol. 13, no. 3, pp. 1787–1810, 2023, <https://doi.org/10.1039/D2RA05903G>.
10. X. Zhao *et al.*, "Accelerated aging of all-inorganic, interface-stabilized perovskite solar cells," *Science*, vol. 0, no. 0, p. eabn5679, Jun. 2022, <https://doi.org/10.1126/science.abn5679>.
11. M. Peplow, "A new kind of solar cell is coming: is it the future of green energy?," *Nature*, vol. 623, no. 7989, pp. 902–905, Nov. 2023, <https://doi.org/10.1038/d41586-023-03714-y>.
12. C.-H. Chen, Z.-K. Wang, and L.-S. Liao, "Perspective on perovskite indoor photovoltaics," *Appl. Phys. Lett.*, vol. 122, no. 13, p. 130501, Mar. 2023, <https://doi.org/10.1063/5.0147747>.
13. K.-L. Wang, Y.-H. Zhou, Y.-H. Lou, and Z.-K. Wang, "Perovskite indoor photovoltaics: opportunity and challenges," *Chem. Sci.*, vol. 12, no. 36, pp. 11936–11954, 2021, <https://doi.org/10.1039/D1SC03251H>.

14. T. C.-J. Yang, P. Fiala, Q. Jeangros, and C. Ballif, "High-Bandgap Perovskite Materials for Multi-junction Solar Cells," *Joule*, vol. 2, no. 8, pp. 1421–1436, Aug. 2018, <https://doi.org/10.1016/j.joule.2018.05.008>.
15. Q. Ou *et al.*, "Band structure engineering in metal halide perovskite nanostructures for optoelectronic applications," *Nano Mater. Sci.*, vol. 1, no. 4, pp. 268–287, Dec. 2019, <https://doi.org/10.1016/j.nanoms.2019.10.004>.
16. E. L. Unger, L. Kegelmann, K. Suchan, D. Sörell, L. Korte, and S. Albrecht, "Roadmap and roadblocks for the band gap tunability of metal halide perovskites," *J. Mater. Chem. A*, vol. 5, no. 23, pp. 11401–11409, Jun. 2017, <https://doi.org/10.1039/C7TA00404D>.
17. "State of IoT 2023: Number of connected IoT devices growing 16% to 16.7 billion globally," *IoT Analytics*, 24-May-2023. [Online]. Available: <https://iot-analytics.com/number-connected-iot-devices/>. [Accessed: 08-Nov-2023].
18. Š. Tomšič, M. Jošt, K. Brecl, M. Topič, and B. Lipovšek, "Energy Yield Modeling for Optimization and Analysis of Perovskite-Silicon Tandem Solar Cells Under Realistic Outdoor Conditions," *Adv. Theory Simul.*, vol. 6, no. 4, p. 2200931, 2023, <https://doi.org/10.1002/adts.202200931>.
19. B. Lipovšek, M. Jošt, Š. Tomšič, and M. Topič, "Energy yield of perovskite solar cells: Influence of location, orientation, and external light management," *Sol. Energy Mater. Sol. Cells*, vol. 234, p. 111421, Jan. 2022, <https://doi.org/10.1016/j.solmat.2021.111421>.
20. S. Hwang, H. Lee, and Y. Kang, "Energy yield comparison between monofacial photovoltaic modules with monofacial and bifacial cells in a carport," *Energy Rep.*, vol. 9, pp. 3148–3153, Dec. 2023, <https://doi.org/10.1016/j.egy.2023.02.011>.
21. I. Haedrich and M. Ernst, "Impact of angular irradiance distributions on coupling gains and energy yield of cell interconnection designs in silicon solar modules in tracking and fixed systems," *J. Phys. Appl. Phys.*, vol. 54, no. 22, p. 224003, Mar. 2021, <https://doi.org/10.1088/1361-6463/abe967>.
22. M. Jošt *et al.*, "Perovskite Solar Cells go Outdoors: Field Testing and Temperature Effects on Energy Yield," *Adv. Energy Mater.*, vol. 10, no. 25, p. 2000454, 2020, <https://doi.org/10.1002/aenm.202000454>.
23. M. Remec *et al.*, "From Sunrise to Sunset: Unraveling Metastability in Perovskite Solar Cells by Coupled Outdoor Testing and Energy Yield Modelling," *Adv. Energy Mater.*, vol. n/a, no. n/a, p. 2304452, <https://doi.org/10.1002/aenm.202304452>.
24. M. Pirc, Ž. Ajdič, D. Uršič, M. Jošt, and M. Topič, "Indoor Energy Harvesting With Perovskite Solar Cells for IoT Applications—A Full Year Monitoring Study," *ACS Appl. Energy Mater.*, vol. 7, no. 2, pp. 565–575, Jan. 2024, <https://doi.org/10.1021/acsaem.3c02498>.
25. L. Lin *et al.*, "Light Soaking Effects in Perovskite Solar Cells: Mechanism, Impacts, and Elimination," *ACS Appl. Energy Mater.*, Apr. 2023, <https://doi.org/10.1021/acsaem.2c04120>.
26. B. Li *et al.*, "Revealing the Correlation of Light Soaking Effect with Ion Migration in Perovskite Solar Cells," *Sol. RRL*, vol. 6, no. 7, p. 2200050, 2022, <https://doi.org/10.1002/solr.202200050>.
27. J. Herterich, M. Unmüssig, G. Loukeris, M. Kohlstädt, and U. Würfel, "Ion Movement Explains Huge VOC Increase despite Almost Unchanged Internal Quasi-Fermi-Level Splitting in Planar Perovskite Solar Cells," *Energy Technol.*, vol. 9, no. 5, p. 2001104, 2021, <https://doi.org/10.1002/ente.202001104>.
28. B. Cai *et al.*, "Unveiling the light soaking effects of the CsPbI3 perovskite solar cells," *J. Power Sources*, vol. 472, p. 228506, Oct. 2020, <https://doi.org/10.1016/j.jpowsour.2020.228506>.
29. S. Suckow, T. M. Pletzer, and H. Kurz, "Fast and reliable calculation of the two-diode model without simplifications," *Prog. Photovolt. Res. Appl.*, vol. 22, no. 4, pp. 494–501, 2014, <https://doi.org/10.1002/pip.2301>.
30. F. Pedregosa *et al.*, "Scikit-learn: Machine Learning in Python," *J. Mach. Learn. Res.*, vol. 12, no. 85, pp. 2825–2830, 2011.



Copyright © 2024 by the Authors. This is an open access article distributed under the Creative Commons Attribution (CC BY) License (<https://creativecommons.org/licenses/by/4.0/>), which permits unrestricted use, distribution, and reproduction in any medium, provided the original work is properly cited.

Arrived: 06. 02. 2024

Accepted: 03. 06. 2024

MIDEM 2024

59th INTERNATIONAL CONFERENCE ON MICROELECTRONICS, DEVICES AND MATERIALS WITH THE WORKSHOP ON ELECTROMAGNETIC COMPATIBILITY: FROM THEORY TO PRACTICE

October 2nd – October 4th, 2024
 Rimske Toplice, Slovenia

Announcement and Call for Papers

Chairs:

**Assoc. Prof. Dr. Benjamin
 Lipovšek**
Assoc. Prof. Dr. Marko Jankovec

IMPORTANT DATES

Abstract submission deadline:

May 17, 2024

Acceptance notification:

June 30, 2024

Full paper submission deadline:

August 31, 2024

Invited and accepted papers will be published in the Conference Proceedings.

Detailed and updated information about the MIDEM Conferences, as well as for paper preparation can be found on

<http://www.midem-drustvo.si//>

GENERAL INFORMATION

The 59th International Conference on Microelectronics, Devices and Materials with the Workshop on Electromagnetic Compatibility: From Theory to Practice continues the successful tradition of annual international conferences organised by the MIDEM Society, the Society for Microelectronics, Electronic Components and Materials. The conference will be held in Rimske Toplice, Slovenia, from **OCTOBER 2nd – 4th, 2024.**

Topics of interest include but are not limited to:

- Electromagnetic compatibility (workshop topic)
- Novel monolithic and hybrid circuit processing techniques,
- New device and circuit design,
- Process and device modelling,
- Semiconductor physics,
- Sensors and actuators,
- Electromechanical devices, microsystems and nanosystems,
- Nanoelectronics,
- Optoelectronics,
- Photovoltaics,
- Electronic materials science and technology,
- New electronic materials and applications,
- Materials characterization techniques,
- Reliability and failure analysis,
- Education in microelectronics, devices and materials.

ORGANIZER:

MIDEM Society - Society for Microelectronics, Electronic Components and Materials, Slovenia

PARTNERS:

UL FE, IJS, IMAPS - Slovenia Chapter, IEEE - Slovenia Section



Boards of MIDE M Society | *Organi društva MIDE M*

MIDE M Executive Board | Izvršilni odbor MIDE M

President of the MIDE M Society | Predsednik društva MIDE M

Prof. Dr. Barbara Malič, Jožef Stefan Institute, Ljubljana, Slovenia

Honorary president:

Prof. Dr. Marko Topič, UL, Faculty of Electrical Engineering, Slovenia

Vice-presidents | Podpredsednika

Prof. Dr. Janez Krč, UL, Faculty of Electrical Engineering, Ljubljana, Slovenia

Dr. Iztok Šorli, Mikroiks d.o.o., Ljubljana, Slovenia

Secretary | Tajnik

Olga Zakrajšek, UL, Faculty of Electrical Engineering, Ljubljana, Slovenia

MIDE M Executive Board Members | Člani izvršilnega odbora MIDE M

Prof. Dr. Slavko Bernik, Jožef Stefan Institute, Slovenia

Assoc. Prof. Dr. Miha Čekada, Jožef Stefan Institute, Ljubljana, Slovenia

Prof. DDr. Denis Đonlagić, UM, Faculty of Electrical Engineering and Computer Science, Maribor, Slovenia

Prof. Dr. Vera Gradišnik, Tehnički fakultet Sveučilišta u Rijeci, Rijeka, Croatia

Mag. Leopold Knez, Iskra TELA, d.d., Ljubljana, Slovenia

Mag. Mitja Koprivšek, ETI Elektroelementi, Izlake, Slovenia

Asst. Prof. Dr. Gregor Primc, Jožef Stefan Institute, Ljubljana, Slovenia

Prof. Dr. Janez Trontelj, UL, Faculty of Electrical Engineering, Ljubljana, Slovenia

Asst. Prof. Dr. Hana Uršič Nemevšek, Jožef Stefan Institute, Ljubljana, Slovenia

Dr. Danilo Vrtačnik, UL, Faculty of Electrical Engineering, Ljubljana, Slovenia

Supervisory Board | Nadzorni odbor

Dr. Drago Resnik, retired, Slovenia

Prof. Dr. Franc Smole, retired, Slovenia

Prof. Dr. Drago Strle, UL, Faculty of Electrical Engineering, Ljubljana, Slovenia

Court of honour | Častno razsodišče

Darko Belavič, retired, Slovenia

Prof. Dr. Danjela Kuščer Hrovatin, Jožef Stefan Institute, Ljubljana

Dr. Hana Uršič Nemevšek, Jožef Stefan Institute, Ljubljana, Slovenia

Informacije MIDE

Journal of Microelectronics, Electronic Components and Materials

ISSN 0352-9045

Publisher / Založnik:

MIDEM Society / Društvo MIDE

Society for Microelectronics, Electronic Components and Materials, Ljubljana, Slovenia

Strokovno društvo za mikroelektroniko, elektronske sestavne dele in materiale, Ljubljana, Slovenija

www.midem-drustvo.si